FEDERAL UNIVERSITY OF UBERLÂNDIA
School of Mechanical Engineering

FEMEC
FACULDADE DE ENGENHARIA MECÂNICA

LUCAS DE SOUZA MEIRA

Reduced-Order Acoustic Predictions of Non-Axisymmetric Nozzle Jets

Uberlândia
2025

LUCAS DE SOUZA MEIRA

Reduced-Order Acoustic Predictions of Non-Axisymmetric Nozzle Jets

Thesis submitted to the Graduate Program in Mechanical Engineering at the Federal University of Uberlândia, in partial fulfillment of the requirements to obtain the degree of **Doctor in Mechanical Engineering**.

Concentration area: Heat Transfer and Fluid Mechanics.

Advisor: Prof. Dr. Francisco José de Souza.

Uberlândia
2025

Ficha Catalográfica Online do Sistema de Bibliotecas da UFU
com dados informados pelo(a) próprio(a) autor(a).

M514
2025

Meira, Lucas de Souza, 1991-
Reduced-Order Acoustic Predictions of Non-Axisymmetric Nozzle Jets [recurso eletrônico] / Lucas de Souza Meira. - 2025.

Orientador: Francisco José de Souza.
Tese (Doutorado) - Universidade Federal de Uberlândia, Pós-graduação em Engenharia Mecânica.
Modo de acesso: Internet.
DOI http://doi.org/10.14393/ufu.te.2025.608
Inclui bibliografia.

1. Engenharia mecânica. I. Souza, Francisco José de,1973-, (Orient.). II. Universidade Federal de Uberlândia. Pós-graduação em Engenharia Mecânica. III. Título.

CDU: 621

Bibliotecários responsáveis pela estrutura de acordo com o AACR2:
Gizele Cristine Nunes do Couto - CRB6/2091
Nelson Marcos Ferreira - CRB6/3074

UNIVERSIDADE FEDERAL DE UBERLÂNDIA
Coordenação do Programa de Pós-Graduação em Engenharia Mecânica
Av. João Naves de Ávila, nº 2121, Bloco 1M, Sala 212 - Bairro Santa Mônica, Uberlândia-MG, CEP 38400-902
Telefone: (34) 3239-4282 - www.posmecanicaufu.com.br - secposmec@mecanica.ufu.br

ATA DE DEFESA - PÓS-GRADUAÇÃO

Programa de Pós-Graduação em:	Engenharia Mecânica				
Defesa de:	Tese de Doutorado, nº 412, PPGEM				
Data:	29/10/2025	Hora de início:	14:05	Hora de encerramento:	18:07
Matrícula:	12023EMC008				
Nome do Discente:	Lucas de Souza Meira				
Título do Trabalho:	Reduced-order acoustic predictions of non-axisymmetric nozzle jets				
Área de concentração:	Transferência de Calor e Mecânica dos Fluidos				
Linha de pesquisa:	Dinâmica dos Fluidos e Transferência de Calor				
Projeto de Pesquisa de vinculação:	Não se aplica				

Reuniu-se, presencialmente no auditório do MFLab e por videoconferência, a Banca Examinadora, designada pelo Colegiado do Programa de Pós-graduação em Engenharia Mecânica, assim composta: Prof. Dr. Aristeu da Silveira Neto - UFU; Prof. Dr. Elie Luis Martínez Padilla - UFU; Prof. Dr. César José Deschamps - UFSC; Prof. Dr. Filipe Dutra da Silva - UFSC e Prof. Dr. Francisco José de Souza - UFU; orientador do candidato.

Iniciando os trabalhos, o presidente da mesa, Prof. Dr. Francisco José de Souza, apresentou a Comissão Examinadora e o candidato, agradeceu a presença do público, e concedeu ao Discente a palavra para a exposição do seu trabalho. A duração da apresentação do Discente e o tempo de arguição e resposta foram conforme as normas do Programa.

A seguir, o senhor presidente concedeu a palavra, pela ordem sucessivamente, aos examinadores, que passaram a arguir o candidato. Ultimada a arguição, que se desenvolveu dentro dos termos regimentais, a Banca, em sessão secreta, atribuiu o resultado final, considerando o candidato:

Aprovado.

Esta defesa faz parte dos requisitos necessários à obtenção do título de Doutor.

O competente diploma será expedido após cumprimento dos demais requisitos, conforme as normas do Programa, a legislação pertinente e a regulamentação interna da UFU.

Documento assinado eletronicamente por **Francisco José de Souza**, **Professor(a) do Magistério Superior**, em 29/10/2025, às 18:14, conforme horário oficial de Brasília, com fundamento no art. 6º, § 1º, do Decreto nº 8.539, de 8 de outubro de 2015.

Documento assinado eletronicamente por **Aristeu da Silveira Neto**, **Professor(a) do Magistério Superior**, em 29/10/2025, às 18:15, conforme horário oficial de Brasília, com fundamento no art. 6º, § 1º, do Decreto nº 8.539, de 8 de outubro de 2015.

Documento assinado eletronicamente por **Filipe Dutra da Silva**, **Usuário Externo**, em 29/10/2025, às 18:20, conforme horário oficial de Brasília, com fundamento no art. 6º, § 1º, do Decreto nº 8.539, de 8 de outubro de 2015.

Documento assinado eletronicamente por **Elie Luis Martinez Padilla**, **Professor(a) do Magistério Superior**, em 29/10/2025, às 18:36, conforme horário oficial de Brasília, com fundamento no art. 6º, § 1º, do Decreto nº 8.539, de 8 de outubro de 2015.

Documento assinado eletronicamente por **César José Deschamps**, **Usuário Externo**, em 30/10/2025, às 18:11, conforme horário oficial de Brasília, com fundamento no art. 6º, § 1º, do Decreto nº 8.539, de 8 de outubro de 2015.

A autenticidade deste documento pode ser conferida no site https://www.sei.ufu.br/sei/controlador_externo.php?acao=documento_conferir&id_orgao_acesso_externo=0, informando o código verificador **6712205** e o código CRC **489C87E8**.

Referência: Processo nº 23117.067232/2025-01 SEI nº 6712205

To my family, friends, and colleagues.

Acknowledgments

I express my absolute gratitude to my advisor, Professor Dr. Francisco José de Souza, for his instruction and encouragement during my maturation as a scientist in the last years. He gave me the opportunity to learn about science with his great patience and cordiality to share his knowledge and friendship. And I also express special gratitude to my research group (Alessandra, Rafaela, José Guilherme, and Bruno) for dividing experience and expertise with me.

I would like to thank my parents, Sebastião e Maria Albertina, for all kindness and patience, and my brothers, Thiago and Maria Teresa, for the affection. A special thank to Ivani and her family, for kindness and partnership.

I would like to thank all my colleagues of the Fluid Mechanics Laboratory (MFLab), professors, researchers, technicians, and staff, for examples of perseverance and provision of the infrastructure to maintain our work on science. The moments spent during lunches and coffee breaks were full of joy, jokes, new ideas, and learning, and I am grateful for that. A sincere thanks for friendship and cultural sharing with south Americans and Africans brothers during spent times at UFU restaurant, it was a great experience of brotherhood – "may the *magesi* be with you".

And last but not least, I would like to express my total appreciation to God, for the gift of life, health, knowledge, and the opportunity to meet amazing people in my lifetime and make all this possible.

17. And I gave my heart to know wisdom, and to know madness and folly: I perceived that this also is vexation of spirit.
18. For in much wisdom is much grief: and he that increaseth knowledge increaseth sorrow.

Ecclesiastes 1:17-18. Holy Bible

We have to be versatile and pleasant.

Uncle Olavim

Abstract

MEIRA, L. S. **Reduced-Order Acoustic Predictions of Non-Axisymmetric Nozzle Jets**. 154p. Ph.D. Thesis. School of Mechanical Engineering, Federal University of Uberlândia, Uberlândia, 2025.

The jet engines continue to be the major contribution to the noise generation in aircraft, during take-off and approach phases. The jet noise results from the mixing region and the intense turbulence between the core and adjacent flow during the mixing process. In this region a turbulent flow presenting a high Mach and Reynolds number, eddies in several scales, and instabilities convert a mount of mechanical energy in pressure wave fluctuations, generating acoustic noise. Once a crescent growth of air transportation demand, it is mandatory to ensure the birth of quieter projects in aerospace engineering, following the best practices and regulation for noise reduction.

In the present work, the development of a feasible methodology is presented to study and predict noise pattern in subsonic jet ($0.7 \leq M_a \leq 0.8$). By means of the Computational Fluid Dynamics (CFD) and the Generalized Acoustic Analogy (GAA) implemented in an in-house code, named FastJetNoise. The results presented in this research were compared with experimental data provided by Southampton's Doak Laboratory. To conduct the analysis, a commercial Reynolds-Averaged Navier-Stokes (RANS) solver was used to simulate the turbulent flow characteristics. The flow properties were then discretized in a structured mesh, which was computed using the FastJetNoise code. Specific radial and azimuthal coordinates were measured, and their Power Spectral Density (PSD) was compared with experimental results. For this study, a baseline circular smooth nozzle was simulated and validated, with good agreement between the numerical and experimental data. In addition, a few non-axisymmetric nozzles were evaluated and their contribution in noise reduction were estimated.

In conclusion, the findings of this research highlight the potential of the GAA in association with RANS results as an effective tool for jetstream noise prediction. The low computational cost by means this analogy opens the possibilities of different evaluations, such as flow regimes, different geometries and passive noise reduction devices. The accuracy of noise predictions can contribute significantly to the development of quieter, more efficient jet propulsion systems, as well as to the implementation of better noise reduction strategies in the industry.

Keywords: Aeroacoustic, CFD, Generalized Acoustic Analogy, Mixing Jet, Noise.

Resumo

MEIRA, L. S. **Previsões Acústicas de Ordem Reduzida em Bocais de Jatos não-Axissimétricos**. 154p. Tese de Doutorado. Faculdade de Engenharia Mecânica, Universidade Federal de Uberlândia, Uberlândia, 2025.

Os motores a jato continuam sendo a maior contribuição de produção de ruído em aeronaves, especialmente nas fases de decolagem e aproximação. O ruído de jato resulta da intensa turbulência que ocorre na região de mixtura, que está definida entre o núcleo do jato e o escoamento atmosférico. Nesta região um escoamento turbulento a altos números de Reynolds e Mach, estruturas turbilhonares em diversas escalas interagem entre si, convertendo parte da energia cinética do escoamento em flutuações no campo de pressão, produzindo o ruído aeroacústico. Devido à crescente demanda por transporte aéreo, é fundamental garantir a introdução de projetos mais silenciosos e sustentáveis na engenharia aeroespacial, em acordo com as boas práticas e as normas de redução de ruído.

No corrente trabalho, o desenvolvimento de uma metodologia viável é apresentada para o estudo e predição de ruído em jatos subsônicos ($0.7 \leq M_a \leq 0.8$). Por meio da fluidodinâmica computacional (CFD) e Analogia Acústica Generalizada (GAA), implementada em um código interno, FastJetNoise, os resultados apresentados foram comparados com dados experimentais providos pelo Laboratório Doak, de Southamptom. No início da análise, um solucionador comercial baseado em médias de Reynolds (RANS) foi utilizado para simular as características do escoamento,que , posteriormente tiveram suas propriedades discretizadas em uma malha estruturada, calculada usando o código FastJetNoise. Coordenadas radiais e azimutais específicas foram medidas, e sua Densidade Espectral de Potência (PSD) foi comparada com resultados experimentais. Para este estudo, simulamos e validamos um bocal circular liso de referência, com boa concordância entre os dados numéricos e experimentais. Posteriormente, bocais não axissimétricos foram modelados e suas contribuições na redução de ruído foram contabilizadas.

Em suma, os resultados deste trabalho destacam o potencial da GAA em associação com os resultados de simulações RANS como uma ferramenta eficaz para a previsão de ruído em jatos. O baixo custo computacional proporcionado por essa metodologia abre possibilidades para futuras avaliações, como regimes de escoamento, diferentes geometrias e dispositivos de redução passiva de ruído. As previsões de ruído podem contribuir significativamente para o desenvolvimento de sistemas de propulsão a jato mais silenciosos e eficientes, bem como para a implementação de melhores estratégias de redução de ruído na indústria.

Palavras-chave: Aeroacústica, CFD, Analogia Acústica Generalizada, Jato de mistura, Ruído.

List of Figures

List of Tables

List of Abbreviations and Acronyms

ANRD	Active Noise Reduction Device
BBSAB	Broadband Shock-Associated Noise
BC	Before Christian era, or Boundary Conditions
BLAS	Basic Linear Algebra Subprograms
BPR	Bypass Ratio
CAA	Computational Aeroacoustics
CDS	Central Differencing Scheme
CFD	Computational Fluid Dynamics
CFL	Courant Friedrichs Lewy
CNPq	*Conselho Nacional de Desenvolvimento Científico e Tecnológico*
DDES	Delayed Detached Eddy Simulations
DES	Detached Eddy Simulations
DNS	Direct Numerical Simulations
EPNdB	Effective Perceived Noise in Decibels
FAR	Federal Aviation Regulations
FDM	Finite Difference Method
FEM	Finite Element Method
FFT	Fast Fourier Transform
FJR	Flight-Jet Rig
FOU	First Order Upwind
FVM	Finite Volume Method
HLD	High-Lift Device
HVAC	Heat Ventilation Air Conditioning System
ICAO	International Civil Aviation Organization
ISVR	Institute of Sound and Vibration Research (University of Southampton-UK)
JMN	Jet Mixing Noise
LAPACK	Linear Algebra PACKage
LES	Large Eddy Simulations

MFLab	Laboratory of Fluid Mechanics
NAAP	Noise Abatement Approach Procedure
NADP	Noise Abatement Departure Procedure
PNRD	Passive Noise Reduction Device
PSD	Power Spectral Density
QUICK	Quadratic Upstream Interpolation for Convective Kinematics
QUICKER	Quadratic Upstream Interpolation for Convective Kinematics Extended and Revised
RANS	Reynolds Averaged Navier-Stokes equations
RBAC	Regulamento Brasileiro de Aviação Civil
RMS	Root Mean Square
SIL	Sound Intensity Level
SIMPLE	Semi-Implicit Method for Pressure-Linked Equations
SIMPLEC	Semi-Implicit Method for Pressure-Linked Equations Consistent
SOU	Second Order Upwind
SPL	Sound Pressure Level
SWL	Sound Power Level
URANS	Unsteady Reynolds Averaged Navier-Stokes equations

Nomenclature

Roman

$\hat{g}^{a}_{\lambda k}$	Adjoint vector of Green's function
$\mathbf{k}$	Wavenumber vector
$\mathbf{x}$	Observer location
$\mathbf{y}$	Source location
$a_{m,l}$	Series coefficients
c	Sound speed
D_j	Jet diameter
h	Enthalpy
I_ω	Acoustic spectrum
L	Length scale
M	Mach number
M_a	Acoustic Mach number
p	Pressure
R	Specific gas constant for dry air
$R_{\lambda j \kappa l}$	Generalized Reynolds stress autocovariance tensor
$R^{M}_{\lambda j \kappa l}$	Moving-frame Reynolds stress autocovariance tensor
Re	Reynolds number
S	Eikonal
St	Strouhal number
T	Averaging time
t	Time
U	X-component velocity
V	Y-component velocity, or volume

W	Z-component velocity

Greek

α	Exponent
$\delta_{\lambda\kappa}$	Kronecker delta
γ	Specific heat ratio
$\Gamma_{\lambda j}$	Fourier-transformed propagator
$\gamma_{\lambda j}$	Propagator
λ	Wavelength
μ	Fluid dynamic viscosity
ν	Fluid kinematic viscosity
ω	Radian frequency
ϕ	Generic variable
$\psi_{\lambda j\kappa l}$	Generalized Reynolds spectral tensor
ρ	Fluid density
τ	Time delay
τ_w	Wall shear stress
θ	Observer polar angle measured from jet axis
$\tilde{\omega}$	Radian frequency
ε	Turbulence dissipation rate, or transformation rate of k

Subscripts

0	Related to stagnation
∞	Relative to ambient or far-field
λ,κ	Tensor indices $=$ 1,2,3,4
i,j,k,l	Tensor indices $=$ 1,2,3
w	Related to the wall, western neighbor

Physicals Constants

g	Gravity	$9.81\,m/s^2$

Mathematical Operator

∇	Laplacian operator

Contents

1 Introduction

> There is geometry in the humming of the strings. There is music in the spacing of the spheres.
>
> ---
>
> *Pythagoras of Samos*
> *570 BC - 495 BC*

The term *'Aeroacoustics'* refers to the study of the sound generated by fluid flows, such as air. This chapter provides an initial overview of the main issues in this field: the importance of understanding jet mixing noise (JMN), the main trends, and the perspectives around this theme in scientific and technical research. It briefly explains the bigger picture on the noise generation by jets, and how it affects the daily lives of many people and why it demands significant attention from both industry and the scientific community. The text also introduces the theme of the thesis and presents some surveys around this matter; as an important research field, the aeroacoustic around JMN have been increased and has brought the spotlight to the topic. In addition, the main contributions of this work developed code and techniques are presented, along with a few topics and goals intended, which is the central focus of this work. Finally, the chapter concludes with a summary of the thesis structure.

1.1 Relevance of The Topic

There is a well-established knowledge around the JMN matter, in several meanings, such as: from discharge of gaseous fluid or vapor in industrial facilities to the noise production by jet engines in the aircrafts. Specifically on the noise produced by jet engines, the interest in the generation of noise and techniques or technologies to mitigate it has been initiated with the jet era in the aviation. An example of this is the de Havilland DH 106 Commet, the first pressurized and jet powered commercial aircraft, that was introduced in the decade of 1950 – epoch when the first scientific contributions around this theme initiated by Lighthill (1952, 1956). The crescent air traffic in urban areas revealed a new demand to understand noise generation and possible solutions for wellness in airports and nearby.

Efforts were concentrated to reduce fuel consumption and maximize efficiency in the later decades to develop more efficient engines based on Brayton cycle. Consequently, with the introduction of turbofan engines and the enlargement of the bypass ratio in these engines, the noise generated by the engines was significantly reduced, if compared to the early turbojets. As justified by Newton's second law, a slight acceleration in a huge amount of mass of cold air by an engine is more effective to produce thrust than a great acceleration in a small portion of gas. Due to it, turbofan engines, which have a coaxial configuration of cold air flowing around the hot gasses exhausted by the engine, reduce the shear layer strength between the fluid layers during the mixing regions of the jet, reducing the noise signature, as experimentally demonstrated by Almeida et al. (2014); Proença (2013, 2018). However, jet engine-powered aircraft are likely to continue to be the bottleneck for the introduction of quieter vehicles and the insurance of low-levels of noise in urban areas.

In a simple search in scientific report platforms, for instance the Scopus platform in Elsevier[1], one might find the tendency of publication around some subject. Scopus is a widely used abstract and citation database that provides access to a vast collection of research literature, including journals, books, and conference proceedings. It's known for its comprehensive coverage of scientific, social science, and arts and humanities fields, making it valuable for researchers and scientists. This type of survey is a good tool that enables users to explore research, identify trends, and connect with other researchers. The Figure 1.1 presents a brief overview of the scientific publications on the subject over the years (a) and the metrics of the main contributions of countries and territories (b) for the same subject. The keywords used in this initial search were: *jet noise*, *reduction*, and *mitigation*.

The mitigation of JMN has been a central challenge in aeroacoustics since the mid-20th century, reflecting both technological and societal pressures. Early studies, spanning from the 1950s to the 1970s, were largely exploratory, with a modest number of publications per year, as shown in Figure 1.1 (a). During this period, theoretical foundations such as Lighthill's acoustic analogy (Lighthill, 1952, 1956) and subsequent refinements by Lilley (1974); Ffowcs Williams and Hawkings (1969) and others laid the groundwork to understand noise generation in turbulent high-speed flows. However, research was limited by computational capacity and experimental techniques, resulting in modest progress in translating theoretical insights into effective mitigation strategies. The relatively low and fluctuating publication output observed during these decades reflects the nascency of the field (Aeroacoustics), where attention to jet noise was overshadowed by primary concerns of propulsion efficiency and thrust generation in the rapidly growing aviation industry. The introduction and evolution of turbofan engines after the 1970s is likely a reason for a reduction in publications in subsequent decades. Due to their quieter noise levels, turbofan engines brought a pleasant and careless time for the industry and regulators.

---

[1] URL: https://www.elsevier.com/pt-br/products/scopus

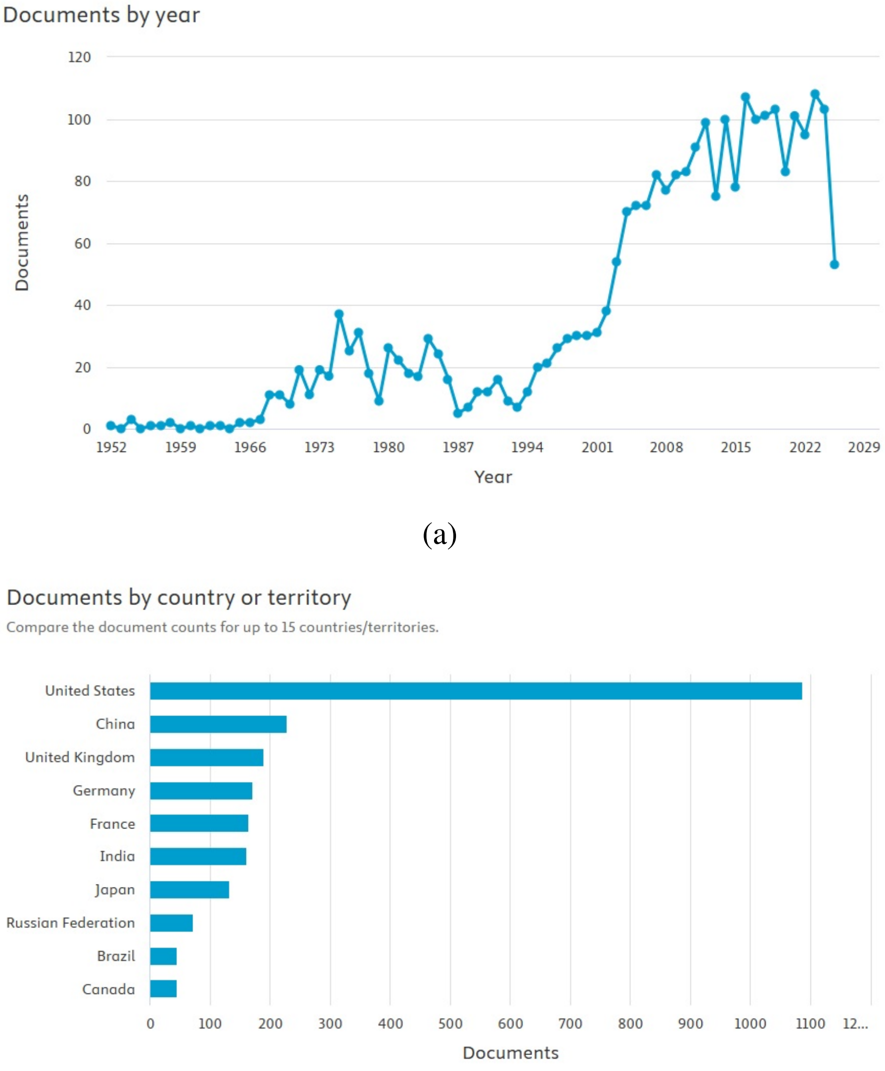

(a)

(b)

Figure 1.1: A tendency of publications over the years. Publications by year(a), and publications by country or territory (b). (Metrics reported by Scopus platform).

In passing, a marked shift in research activity occurred from the late 1990s up to the early 2000s, as shown by the steep increase in publications in Figure 1.1 (a). This transition is closely aligned with regulatory developments, particularly the progressive tightening of noise certification standards under the International Civil Aviation Organization (ICAO) Annex 16 (Tam, 1998). The introduction of Chapter 3 in the late 1970s, followed by Chapter 4 in 2006 and more recently Chapter 14, imposed increasingly stringent noise limits on civil aircrafts. These international policies, coupled with the growing societal awareness of environmental impacts, created strong incentives for both industry and academia to pursue innovative solutions for jet noise reduction. At the same time, technological advances, such as high-fidelity large-eddy simulations (LES), as presented by Meira and Souza (2020); Ricciardi et al. (2019), hybrid computational aeroacoustics (CAA) methods, and advanced flow diagnostics (e.g., particle image velocimetry, microphone phased arrays) enabled a more accurate characterization of jet turbulence and the acoustic fields it generates. The result is a sharp expansion in the knowledge base, reflected in the publication surge, and the maturation of noise control strategies, including chevron nozzles, fluid injection, and optimized acoustic liners – patents presented at the end of Chapter 2.

From 2010 onward, the publication trend appears to plateau, stabilizing at a relatively high annual output. This suggests the consolidation of jet noise mitigation as a mature research field. Although incremental advances continue, the fundamental noise generation mechanisms and baseline passive control strategies are now well established (Goldstein, 2003; Goldstein and Leib, 2008; Leib and Goldstein, 2011). Current efforts focus on the integration of noise reduction with other performance requirements, such as fuel efficiency, emissions reduction, and structural integrity, within the broader context of sustainable aviation. Emerging research directions include hybrid-electric propulsion, distributed propulsion systems, and novel nozzle architectures designed for next-generation aircraft (Ishii et al., 2019; Câmara et al., 2026). Nevertheless, the apparent stabilization of publication rates reflects not stagnation but rather a transition from foundational exploration to the refinement and integration of established knowledge, as observed in the Dunning-Krüger plateau of philosophy.

The geographical distribution of publications, presented in Figure 1.1 (b), reveals the global but asymmetrically concentrated nature of jet noise research. The United States dominates the field, a result of sustained investment in aerospace research and development, particularly through NASA's noise reduction programs such as the Advanced Subsonic Technology (AST) initiative in the 1990s and the more recent Quiet Aircraft Technology (QAT) and Subsonic Fixed Wing projects. These initiatives explicitly targeted compliance with International Civil Aviation Organization (ICAO) (2016, 2022) noise standards and aimed to ensure the competitiveness of U.S. aircraft manufacturers in the global market. China and the United Kingdom also emerge as leading contributors, reflecting the rapid expansion of Chinese aerospace research capacity (see codes CN109800488A, CN103133180B, CN106481455B in Table A.1) and the strong academic tradition of the United Kingdom in fluid mechanics and aeroacoustics, represented by institutions such as Imperial College London, the University of Cambridge, and Southampton University. Germany, France, and Japan also maintain robust programs, often in collaboration with major aerospace companies and European consortia (European Civil Aviation Conference, 2005a,b) such as Airbus (2007), highlighting the strong industrial-academic links driving progress in this domain.

Although smaller in scale, contributions from countries such as India, Brazil, Canada, and the Russian Federation underscore the recognition of jet noise as a global challenge, with environmental, regulatory, and operational implications that transcend national borders. These efforts often align with broader strategies for participation in international aviation markets and the need to comply with International Civil Aviation Organization (ICAO) (2022) noise certification standards for both domestic and export-oriented aircraft programs. Importantly, the diversity of contributing countries reflects not only the global impact of aircraft noise but also the shared technological and policy challenges that compel collaborative research efforts. In this sense, jet noise mitigation research represents a clear example of how international regulation, scientific innovation, and industrial competitiveness converge to shape the trajectory of a specialized yet globally significant research field.

In summary, the bibliographic trend analysis presented in Fig. 1.1 (a) and (b) provides information on the historical evolution and geographical distribution of jet noise research. From its theoretical foundations in the mid-20th century, through regulatory-driven expansion in the early 2000s, to its current stage of consolidation and refinement, jet noise mitigation has become a mature and globally distributed research area. The strong influence of ICAO standards, the role of national aerospace programs, and the enabling advances in computational and experimental methods have all contributed to this trajectory. Future research will likely continue to emphasize multidisciplinary integration, addressing not only noise reduction but also efficiency, sustainability, and emerging propulsion concepts in the pursuit of quieter and cleaner air transportation systems.

Based on these evolving trends and the relatively well-established knowledge, the noise prediction for JMN is not a simple task. There are several numerical approaches to estimate noise generation with a satisfactory accuracy; however, these approaches demand a high computational cost and execution time. When the interest zone is the far-field, sound propagation, interferences, and surface/flow interaction, it makes the calculation more and more difficult. In addition, this work presents a series of techniques and a novel method implemented in an in-house code (FastJetNoise) with the aim of producing fast and feasible results for different non-axisymmetric nozzle geometries. The main objectives of this thesis are discussed on the next section.

1.2 Objectives of The Thesis

In order to simulate and mitigate the noise produced by transonic jets in static conditions, the fundamental mechanisms of the turbulence source region, the pressure, and velocity field along the jet turbulence transition must be well understood. In an ample sense, the objective of this thesis is to improve the techniques used in jet noise prediction tools which are fast and reliable to be used by the industry during conceptual phases of nozzle designs. We investigated the flow pattern and characteristics obtained by commercial CFD solvers, such as ANSYS Fluent$^{\mathrm{TM}}$, and an in-house code, named FastJetNoise, was implemented, verified, and validated in contrast to the experimental results along this document. More specifically, the main objectives of this thesis are briefly summarized below.

1. establish a robust patch of techniques to use CFD RANS results to obtain a more correct analysis of transonic jet nozzles;
2. propose a methodology with a considerable low computational cost to obtain the SPL of convergent nozzles;
3. to evaluate and validate different techniques of domain discretization of the problem, such as the adoption of axisymmetry (and rotational symmetry) of different nozzles;
4. to present results of the well-known schemes (available in literature) performed by a second-order methods;
5. to present an in-house code able of solve the CAA problems in 4th order interpolation schemes for Green's function, named FastJetNoise.
6. to evaluate different geometries of passive noise reduction devices (PNRD) and their implications in PSD reduction.

1.3 Dissertation Outline

This work was developed at the Federal University of Uberlândia (UFU) and, more specifically, in the Fluid Mechanics Laboratory (MFLab). The majority of the experimental results presented here were accessed by a cooperation with the Institute of Sound and Vibration Research (ISVR) located in University of Southampton. The experimental campaign was conducted in ISVR during the season from July 2020 to June 2021. All the numerical simulations and their results were performed in the MFLab at UFU.

This work is divided into six main chapters. In each of them, an introduction, a development, and a conclusion is made about the subject in question.

Chapter 1 gives a brief introduction to the Acoustic and Aeroacoustic research fields. It states a bigger picture of the subject in scientific and technical field and its relevance during its hype cycle.

The basic theory and the main concepts on the Fluid Mechanics of turbulent jets are presented in Chapter 2. Therefore, some important researches and researchers are mentioned in this section, and their efforts of understanding and modeling the Physics beneath noise production.

Chapter 3 shows the methodologies taken in this work to solve the problem in circular transonic nozzles. The main models, such as: physical, mathematical and numerical ones, were described more precisely. All assumptions, simplifications, and constraints of the problem are explained in this part of the document.

Chapter 4 presents the results of the numerical simulations. It is divided into three main parts: one of that contains the validation results – performed in a 2D approach – for the $40\,mm$ smooth circular nozzle (R40), the second and the third that present the results for two different passive noise reduction devices (PNRD) in 3D simulation cases (SC03, SC06, SC09, SC12, and IN). A significant reduction in the PSD signature of these PNRDs was observed and the behavior of the flow downstream to the nozzle was investigated. It was observed that the PNRDs directly affect the turbulence variables in near-field, consequently, altering the PSD observed in the far-field.

The conclusion of this dissertation is dealt with in Chapter 5, general comments and observations are made in this section. A summary of the objectives of this work is discussed and the main considerations are pointed out to ensure the robustness of the methodology. In the end, there are several highlights and contributions of the work, as well, future steps (Chapter 6) for subsequent investigations in the Aeroacoustic of jet mixing noise (JMN) are suggested, as contintuity of this work.

2 Background Theory

> No man ever steps in the same river twice, for it's not the same river and he's not the same man.
>
> *Heraclitus of Ephesus*
> *535 BC - 475 BC*

Flow-induced noise refers to sound generated by the interaction of a fluid flow with solid surfaces or within the flow itself, as pointed in Chapter 1. It arises when unsteady flow features such as turbulence, vortices, or pressure fluctuations interact with objects (e.g., ducts, cavities, blades) or boundaries, producing acoustic waves that propagate as noise.

The present chapter is divided in four main items, which are 1) an introduction to the concepts of sound and noise, their impacts in human life, and the first contributions around the noise control techniques; 2) a state around the aircraft noise problem, the noise standards and regulations, and future perspectives for new generation of aircraft; 3) a brief appreciation around the aerodynamics in JMN, for instance the physics involved in compressible flows and turbulence. Afterwards, a review of acoustics in JMN is presented, the early models, and their evolution. A literature review on the main models discussed in Aeroacoustics and the methodology used in this work; such as, Lighthill's and Goldstein's analogies. In the last part, the review then moves to important patents in PNRD, where the approaches used in each PNRD is inferred and the involved principles in noise reduction an its effectiveness. The chapter ends by summarizing the essential points and outlining their relation to the chapters that follow.

2.1 General Context

By the concepts of Physicis, as pointed by Gerges (2000) and Howe (1998, 2003), the sound is defined as a series of fluctuations on the pressure field in an elastic medium, such as: gaseous, liquid or solid. As disposed in the scheme of the Fig. 2.1 (a), the sound obey the wave mechanics laws and, as any wave, can suffer reflection, refraction, diffraction and absorption by surfaces or other mediums. However, a specific band of frequencies and amplitude of pressure fluctuations is considered sensible by human ears. Quantitatively, pressure amplitudes lower than the hearing threshold (20 μPa) are not perceptible, on the other hand, pressure pulses greater than 60 Pa might cause pain sensation (threshold of pain) or severe damage to the inner ear tissues or the eardrums. The band of frequency felt by human ears is between, in average, 20 Hz and 20 kHz; sounds lower than these limits are named infra-sound, while the superior ones, are denominated ultrasound.

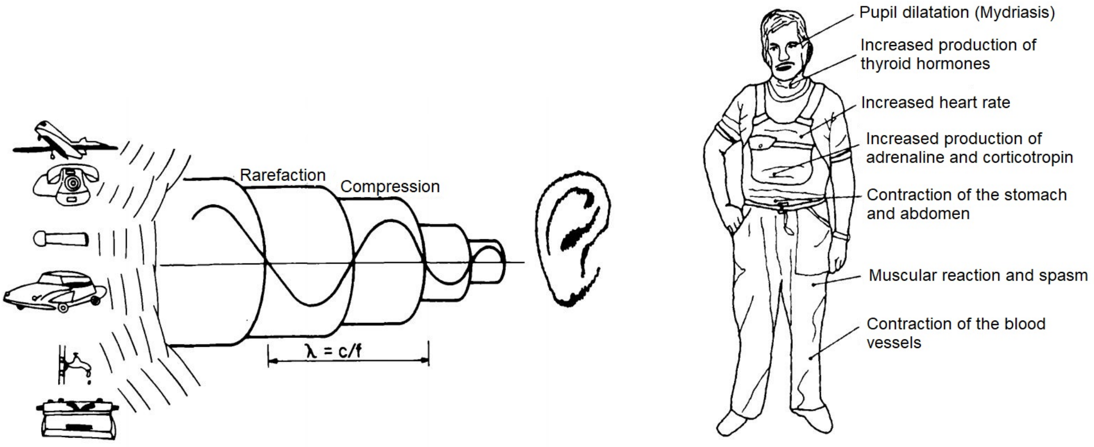

(a) (b)

Figure 2.1: Wave behavior of sound propagation (a), and effects of noise in human body (b). Adapted from (Gerges, 2000).

Although sound is a recurring part of everyday life, the treatment and use of this information must represent several important situations. The modern life is an intense demonstration of sound stimuli, such as: music, working machines, wind passing through buildings and structures, notifications in phones, etc. However, a variety of these stimuli are defined as inconvenient, unwanted, or unhealthy, and, to this class of sounds it is given a name of *noise*. Recently, several studies have shown that long exposure in noisy places can cause psychological disturbances, sleep problems, and mood disorders. Likewise, there are other physiological effects related exposure to noise, as the increasing rate of arterial hypertension and infertility, according to T Munzel and Basner (2014) and Min and Min (2017), respectively. Systematic health studies, such as Hansell et al. (2013), discuss the influence of aircraft noise exposure and cardiovascular disease around Heathrow Airport in London. For easy understanding, Gerges (2000) presents a sketch pointing out different consequences of exposure to high-level noise, as shown in Figure 2.1 (b), disturbances in hormonal levels in the thyroid gland, adrenaline, other hormonal glands, and neurotransmitters levels can cause several mood disorders, such as: irritability, stress, fatigue, and other behavioral problems.

The Table 2.1 presents an envelope of intensity levels (IL) and sound pressure levels (SPL) found in several noise sources. As exposed by Rienstra and Hirschberg (2006), one notices that the level of amplitude of pressure waves can vary from orders of 20^{-6} Pa up to 200 Pa, while in energy levels (intensity) from $10^{-12}\,\mathrm{W/m^2}$ up to $100\,\mathrm{W/m^2}$, respectively. For a better understanding about these levels, a supersonic jet, such as Concorde, during take-off, is not able to produce sufficient acoustic energy to warm a cup of tea; on the other hand, it is capable to cause severe and irreversible damages to hearing in people nearby.

Table 2.1: Sound intensity level (SIL), sound pressure level (SPL), and pressure amplitude.

Source	SPL [dB]	SIL [W/m^2]	Pressure [Pa]
Atomic bomb, 5 m away (estimation)	250	1,00e+13	6,32e+7
Rocket, 30 m away; Blue whale vocalization, 1 m away	180	1,00e+6	2,00e+4
Fighter jet, 30 m away	150	1,00e+3	6,32e+2
Threshold of pain; Riffle shot, 1 m away	140	1,00e+2	2,00e+2
Train horn, 1 m away	130	1,00e+1	6,32e+1
Rock concert; Jet takeoff, 100 m away	120	1,00e+0	2,00e+1
Superbike, 5 m away	110	1,00e−1	6,32e+0
Pneumatic driller, 2 m away	100	1,00e−2	2,00e+0
Heavy truck, 1 m away	90	1,00e−3	6,32e−1
Limit by regulation NR-15 (8 **hours)**	85	3,16e−4	3,56e−1
Vacuum cleaner, 1 m away; Intense city traffic	80	1,00e−4	2,00e−1
City traffic, à 5 m	70	1,00e−5	6,32e−2
Office interior or restaurant	60	1,00e−6	2,00e−2
Cinema, not loud	30	1,00e−9	6,32e−4
Human breath, à 3 m	10	1,00e−11	6,32e−5
Human hearing threshold	0	1,00e−12	2,00e−5

Adapted from (Marangon, 2020)

2.2 Early Studies in Acoustics

On the year of 2020 was celebrated the International Year of Sound (IYS 2020), extended to 2021 due to the COVID-19 pandemic. As an international initiative to highlight and discuss the importance of sound in all aspects of life on earth. The event brought towards an understanding of sound-related issues at the national and international level, ensuring a good future for the next generations and modern and quieter ambient, as disposed in International Commission for Acoustics (ICA) (2021); Berg (2025).

In a brief timeline of Acoustics evolution, we see that the first issues around sound and noise began before Christian era. The early systematic studies in acoustics are generally attributed to the ancient Greek philosopher Pythagoras in the 6th century BC. Pythagoras' work focused on the relation between musical sounds and mathematics, precisely his experiments with vibrating strings. He discovered that harmonious musical intervals could be produced by strings whose lengths were in simple integer ratios. For instance, any string on a tuned guitar can produce the same note (in overtones) with the half of its length, this is known as *harmonics*.

However, the field of Acoustics as a formal science continued to evolve over centuries with significant contributions from other key figures:

- Aristotle (4th century BC) correctly hypothesized that sound propagates through the motion of air;
- The Roman architect Vitruvius (1st century BC) documented his knowledge of sound transmission in his writings on theater design, demonstrating an early understanding of architectural acoustics.
- Galileo Galilei (16th-17th centuries) laid the groundwork for modern acoustics by elevating the study of vibrations to a science, correlating the pitch of a sound with the frequency of its source.
- The term "acoustics" itself was coined by the French physicist Joseph Sauveur in the early 18th century. He used the french term "*acoustique*" to refer the science of sound.
- In the 19th century, Hermann von Helmholtz and Lord Rayleigh solidified the field with extensive theoretical and experimental work, with Rayleigh's two-volume book The Theory of Sound (1877 and 1894) marking the beginning of modern acoustics as a distinct discipline.

I his masterpiece, John William Strut, well-known as 3rd Baron of Rayleigh (1894), discusses about the theory of sound in its second edition. An introduction around the previous decades in experimental determination of the speed of sound by french scientists is mentioned, as to as the used techniques with canons and chronometers converged to the approximated value of 337 m/s in an quiet atmosphere at a temperature of 0^o C – which is reasonably close to the value of 331.29 m/s by mean the Equation 2.1

$$c = \sqrt{\gamma RT}, \tag{2.1}$$

where c is the speed of sound in the air, γ is the specific heat ratio (c_p/c_v), R is the universal gas constant (287 J/kgK for the air), and T is the temperature in Kelvin.

Rayleigh (1894) and other researchers of this epoch, such as Helmholtz (1877), studied several phenomena with open cavities and resonators. These pioneer analytic studies were the cornerstone in the understanding of the properties of resonators as we know them today. Simple solutions have still been used on the basis of these two-centuries-old findings.

Although these studies are based on pure analytic models and simplified analysis, they are a rapid solution to many engineering problems related to internal flows today. One example of this is the use of well-sized resonators in exhausting pipes in high-performance cars. A rule of thumb in the *gearhead* technical community states the sizing of Helmholtz resonators in exhausting pipes, as depicted in Figure. 2.2 (a)[1]. These bottle shape resonators create a phase opposition wave signal in a specific frequency, that aims into mitigate or cancel surging peaks in noise signal named *droning*. In this condition the resonator acts as a passive noise reduction device (PNRD) of noise-induced frequencies by internal flow.

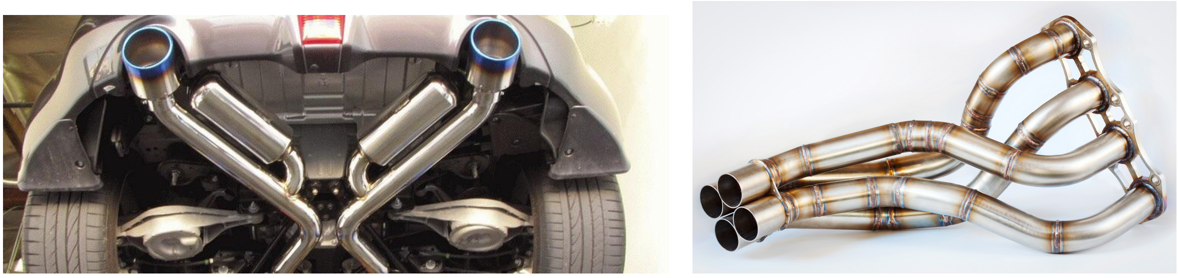

(a) (b)

Figure 2.2: Helmholtz resonators in a car exhausting pipe (a), and seized exhausting pipe for scavenging effect (b).

---

[1] URL: https://tinyurl.com/4tk975sy

The sizing of this type of resonator can be achieved by means Equation 2.2. The total length is divided by 4 due to the nature of phasing opposition of the resonator, named quarter-wavelength resonator. Some studies, for instance Field and Fricke (1998); Cambonie et al. (2018), investigate these devices in noise attenuation in HVAC (Heating, Ventilation and Air Conditioning) systems and curvature effects, respectively. The first one presents pure experimental results and the second presents both experimental and numerical simulations in curved resonators.

$$l = \frac{1}{4}\frac{c}{f_{res}} - \epsilon\,, \tag{2.2}$$

where c is the speed of sound in the air, f_{res} is the resonant frequency, ϵ is a correction due to the diameter of the tube.

Another advance in internal flow acoustics is the use of stationary waves with applications that are both familiar and advanced. An acoustic stationary wave, also known as a standing wave, is a non-propagating, self-reinforcing interference pattern of sound that oscillates in time with a fixed spatial amplitude profile. It is formed by the superposition of two or more identical sound waves traveling in opposite directions. One example of standing waves usage in internal combustion engines is the process named *scavenging*. According to Heywood (2018), engine scavenging is the process of expelling burnt exhaust gases from the cylinder and replacing them with a fresh fuel-air mixture for the next cycle. The exhaust manifold in Figure 2.2 (b)[2] is an example of well-sized tubes that promote engine scavenging, i.e. an acoustic stationary wave maintain its low pressure region during the exhaust valve aperture, which enhance the discharging process of naturally aspirated engines.

Although these simple solutions are easily predictable and feasible, they are limited to a specific value of frequency that depends directly on the sound speed, and this speed is directly dependent to the working temperature, as observed in Eq. 2.1. Due to this, to attenuate a range of frequencies, it is necessary to understand the main sources of flow-induced noise.

The relevance of research and the importance of studying noise generation have been a significant concern in modern engineering analysis and acoustical comfort in new designs. Noise sources have their cause, mainly, in cases that involve solid-solid interactions, vibrating systems, chemical reactions (e.g. combustion), fluid-structural interactions, and purely fluidynamic. Consequently, with the continuous development of the aerial transport and the expansion of urban centers, a new concern emerged: the mitigation of external noise in airports and nearby

---

[2] URL: https://tinyurl.com/3zxy6dj7

areas. This is an important phase in the certification of aircrafts under constant pressure of civil aviation authorities in recent decades (Airbus, 2007, 2019). More recent studies, however, have sought to understand the influence of flow over cavities or on benchmark vehicle structures, such as the works of Henshaw (2000) and Allen et al. (2005), which investigated the aeroacoustic interaction of a missile bay door (M219) in the transonic regime and its impact on noise generation. In turn, Islam et al. (2008) experimentally assessed the influence of an open sunroof in a passenger vehicle on the phenomenon of buffeting and the associated acoustic comfort.

From the perspective of Computational Fluid Dynamics (CFD), the investigation of noise sources has proven to be a highly challenging task. Since modeling the transport of low levels of energy (acoustic waves) involves, significant efforts have been devoted to high-fidelity simulations and high-order methods, for instance studies of aeroacoustics of deployed landing gears, wings and high lift devices (Ricciardi et al., 2019, 2020; Zhang, 2010). Other studies, focused in DES simulations of aeroacoustics in internal flow and evaluation of numerical methods of tonal noise prediction in HVAC systems (Meira and Souza, 2020), and tonal noise mitigation by PNRDs (Cambonie et al., 2018). Based on that, going into the opposite direction, the present thesis aims to employ a simplified CFD and CAA based methodology, with relatively low computational cost established in the workhorse RANS simulations with 2nd-order methods and generalized acoustic analogies (GAA) for jet mixing noise. The findings summarized at the end of this document is a feasible and valuable technique in industrial and conceptual projects of convergent transonic nozzles.

2.3 Aircraft Noise

Aircrafts are a major source of environmental noise pollution, particularly in the airports and nearby regions. According to International Civil Aviation Organization (ICAO) (2016, 2022), with the continuous growth in air travel demand (depicted in Figure 2.3), the global passenger traffic experienced an unprecedented decline in history. With an overall reduction of over 2.7 Bi passengers (-60%), resulting in approximately U$D 372 Bi loss of gross passenger operating earnings of airlines in 2020 alone, compared to its earlier year. Despite the Covid-19 pandemic, the aviation market has had an quasi-constant growth pattern for decades. Surpassing several challenges, such as: Oil Crisis (1973), several Middle East wars, terrorist attacks (9/11/2001), and 2008 financial crisis; the tendency of progress of world air traffic is almost a certainty.

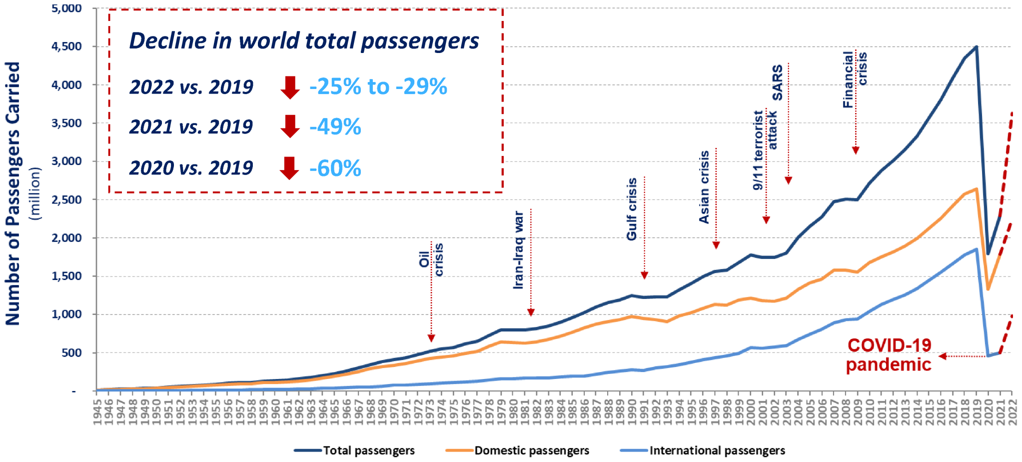

Figure 2.3: World traffic evolution from 1945 to 2022. (International Civil Aviation Organization (ICAO), 2022)

Due to this strength, reducing aircraft noise exposure for communities living near airports has become a central concern for both aircraft manufacturers and aviation regulators (Hansell et al., 2013). Over the past fifty years, steady progress in reducing noise at the source has been achieved, mainly through advances such as increasing the engine bypass ratio (BPR). Figure 2.4 presents a quantitative graph of cumulative noise relative to ICAO Chapter 4 over the years. One notices that the increase in turbofan BPR marks a significant improvement in noise reduction. However, meeting the strict noise limits established by the International Civil Aviation Organization (ICAO) has become an increasingly difficult challenge for the aviation industry as aircraft continue to grow in size and power.

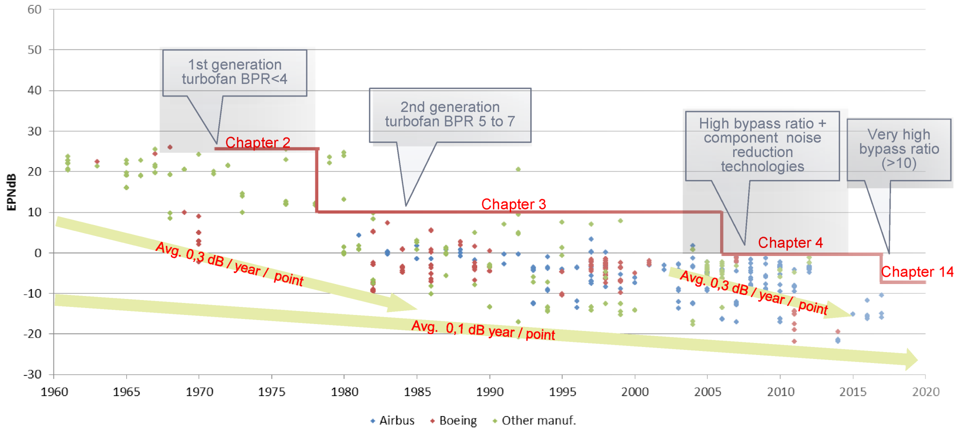

Figure 2.4: Cumulative noise reduction relative to Chap. 4. (Airbus, 2019)

2.3.1 Aircraft Noise Sources

This section presents the principal noise sources associated with aircraft powered by turbofan or turbojet engines and provides a brief overview of the JMN. As stated by Smith (1989), the main sources of aircraft noise are concentrated in the propulsion system (turbofan or turbojet engines) and airframe (HLD, cavities, wings, flaps, landing gear, etc). Looking at the engines, the turbulence downstream created due to a jet mixing region arises from the interaction between the jet by itself and the adjacent atmosphere, which can be in rest (quiescent) or with a freestream velocity (in-flight), producing the acoustic waves and generating noise. The in-flight condition is briefly demonstrated by the experimental results in Cap. 3, however the numerical inveestigation of this type of scenario is beyond the scope of this work.

Aircraft noise originates, according to Hubbard (1991), from multiple physical mechanisms and can be broadly classified into two categories: (1) propulsive or engine noise, and (2) non-propulsive or airframe noise. As illustrated in Figure 2.5 (b), the fan, turbine, compressor, combustor, and exhaust jet constitute the primary sources of engine noise during take-off. Conversely, airframe noise arises from unsteady aerodynamic interactions over structural components such as the fuselage, landing gear, wings, high-lift devices, and stabilizers. These elements represent the most significant individual contributors to the total acoustic emission of an aircraft in approaching phase (Airbus, 2007, 2019).

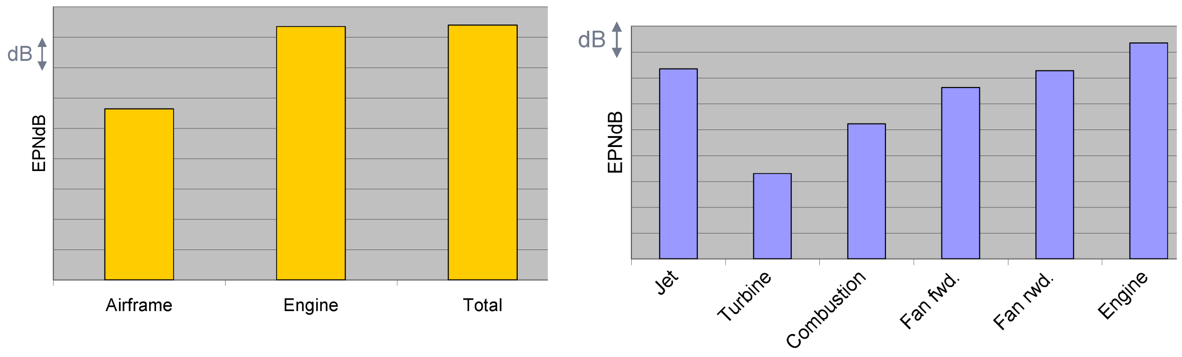

(a) Aircraft noise sources.

(b) Engine noise sources.

Figure 2.5: Parcels of noise contribution in a modern aircraft during take-off. (Airbus, 2007)

Once the present work deals with the noise generated by JMN, some concepts around the engine noise sources must be stated. Noise generated by jet or turbofan engines can be broadly classified into two principal categories: turbomachinery noise and jet noise – as divided by Hubbard (1991).

Turbomachinery noise originates within the engine itself and is primarily associated with the internal mechanical and aerodynamic processes occurring in the fan, compressor, turbine, and combustion core. Each of these components contributes to noise production through mechanisms such as pressure fluctuations, blade–wake interactions, and combustion instabilities. This category of noise is therefore referred to as internal or source-based noise, as it is generated by the operation of the rotating and combusting elements. A crucial determination in this type of noise source, is the fan blade pass frequency (PBF), whose phenomenon is a perceptible noise pattern (Howe, 1998).

In contrast, jet noise is produced externally, downstream of the engine exhaust. McGuirk and Feng (2021) states that the main noise signature in near-field occurs downstream to the jet potential core ($x/D_j \approx 5 - 10$). It arises due to turbulent mixing between fluid streams of different velocities and temperatures—specifically, between the hot core flow and the cooler bypass flow, and between the bypass flow and the surrounding ambient air. The velocity gradients at these shear layers create fluctuating shear stresses that radiate as acoustic waves. Under subsonic operating conditions ($M_a < 1$), this process gives rise to what is commonly referred to as jet mixing noise (JMN), which constitutes the focus of the present investigation.

At supersonic jet velocities (Tam, 1995; Goldstein and Leib, 2008), additional noise mechanisms become significant, including broadband shock-associated noise (BBSAN), generated by the interaction of turbulent structures with shock cells, and screech tones, which are strong tonal emissions resulting from feedback loops between the jet flow and the nozzle lip. However, the physical mechanisms governing these supersonic noise sources are beyond the scope of this work.

2.3.2 Noise Standards and Regulation

Aircraft noise certification is a critical part of the process for getting an aircraft type approved for service. The primary goal is to ensure that modern aircrafts are designed to incorporate the best available noise reduction technology and to mitigate the impact of aviation on communities near airports. Some limitations are imposed in certain airports around the globe due to its high populated areas nearby.

The international standards are set by the International Civil Aviation Organization (ICAO) in Annex 16, Volume I (International Civil Aviation Organization (ICAO), 2016, 2022). These standards are then adopted by national aviation authorities, such as the Federal Aviation Administration (FAA) in the United States, the European Union Aviation Safety Agency (EASA), and the brazilian regulatory of civil agency ANAC (Agência Nacional de Aviação Civil), as described:

- **FAA**: The FAA's regulations are detailed in 14 CFR Part 36, *Noise Standards: Aircraft Type and Airworthiness Certification*.
- **EASA**: The equivalent of EASA is CS-36, titled *Certification Specifications for Aircraft Noise*.
- **ANAC**: The equivalent of brazilian regulation is the RBAC 36 titled *Requisitos de Ruído para Aeronave* (Noise Requirements for Aircraft), is the direct equivalent of the U.S. Federal Aviation Regulations (FAR) Part 36.

Both sets of regulations align with the ICAO framework, establishing the procedures for noise measurement and the maximum noise limits for different types of aircraft.

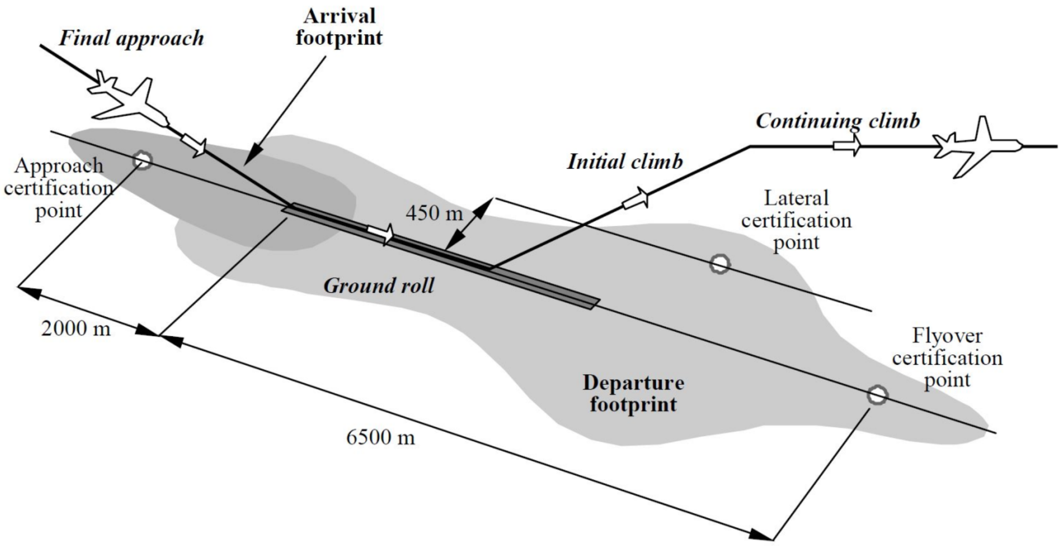

Figure 2.6: Noise measurement points in aircraft certification. (European Civil Aviation Conference, 2005a)

The regulation details the required noise measurement procedures, including the use of specific equipment, test environments, and the three-point measurement system (flyover, lateral, and approach) as defined by ICAO. The final noise level is expressed in EPNdB. According to European Civil Aviation Conference (2005a,b), the flight path used in noise certification campaign are defined in Figure 2.6. In this flight path the three basic points are depicted in each distance from their references. ICAO states that an airplane cannot exceed the EPNdB in acoustic certification tests measured in the reference points of an airport runway. The approach point, under the descent path $2000\,m$ before the landing threshold, lateral (or sideline), where noise is louder on a line 450 m to the side of the initial climb after lift-off, and flyover, under the departure climb path, 6500 m from the Start Of Roll (SOR)[3] (International Civil Aviation Organization (ICAO), 2016).

During a noise certification test, a prototype aircraft performs specific flight maneuvers under controlled conditions while a grid of microphones on the ground records the sound, as depicted in Fig. 2.6. To perform this test, some variables must to be accounted, such as:

- **Test Environment**: The tests must be conducted in specific weather conditions, including limits on wind, temperature, and humidity, to ensure consistent and comparable results. The test area must be flat and free of obstacles that could reflect sound.
- **Measurements**: Microphones are strategically placed at the three reference points mentioned previously. The recorded data is then processed to calculate the Effective Perceived Noise Level (EPNL) in units of EPNdB, which accounts for the duration of the noise, the frequency content, and how loud it sounds to the human ear.
- **Data Correction**: The recorded noise levels are corrected to a standard set of reference conditions (e.g., standard atmospheric pressure and temperature) to remove the influence of varying test conditions.
- **Documentation**: If the noise levels are below the maximum limits for its stage, the aircraft is issued a noise certificate. This document is a critical part of the aircraft's airworthiness certification and must be carried on board for international flights.

According to technical reports, for instance in Airbus (2007), significative noise reduction might be achieved by means of flight path changes and noise-optimized take-off and landing. Although the new PNRDs and geometries evolution, the aircraft operation pattern affects directly the amount of produced noise. Some aircraft manufacturers claim that accomplish an expressive EPNdB reduction with more heavier aircrafts if compared with earlier models using noise abatement procedures (NADP for departure and NAAP for approach).

---

[3] During take-off, an airplane accelerates between the point of brake release (alternatively termed start-of-roll) and the point of lift-off, where speed changes dramatically over a distance of 1500 to $2500\,m$ (4921 to $8202\,ft$), from zero to between 80 and $100\,m/s$.
URL: <https://www2.anac.gov.br/anacpedia/ing-por/tr6803.htm>

2.4 Jet Mixing Noise (JMN)

As seen previously, JMN is one of the dominant components of the overall noise generated by high-speed jets. It arises from the turbulent mixing process between the high-velocity jet exhaust and the surrounding ambient fluid. As the jet issues from the nozzle, strong velocity gradients and shear layers develop, giving rise to large-scale turbulent structures that evolve, interact, and break down into smaller scales. These turbulent fluctuations generate pressure perturbations that radiate as acoustic waves, forming what is commonly referred to as mixing noise (Tam, 1998; Pope, 2000).

A fundamental characteristic of jet mixing noise is its dependence on the jet Mach number. At subsonic jet velocities, the noise is broadband in nature, with most of the energy concentrated at low to mid frequencies. However, as the jet approaches supersonic conditions, additional noise components, such as broadband shock-associated noise (BBSAN) and screech tones, may appear, complicating the acoustic signature (Tam, 1995; Viswanathan, 2009). The classical work of Lighthill (1952) laid the foundation for understanding jet noise by establishing the acoustic analogy, showing that turbulence in a jet behaves as a quadrupole source of sound, with the acoustic power scaling approximately with the eighth power of the jet velocity.

Several experimental and numerical studies have sought to characterize jet mixing noise in both laboratory and practical conditions, studies as Tanna (1977); Lyu and Dowling (2019); Giraldo (2019). Large-eddy simulation (LES) (Rosa et al., 2016) and detached-eddy simulation (DES) methods, for instance, have been widely applied to capture the unsteady turbulent structures responsible for noise generation (Bodony and Lele, 2008). Experimental investigations have complemented these studies by providing detailed acoustic measurements and flow visualizations, allowing for a deeper understanding of the scaling laws and spectral features associated with jet noise (Bridges and Brown, 2004; Jordan and Colonius, 2013).

From an engineering standpoint, the mitigation of jet mixing noise is of great importance due to stringent noise regulations imposed by international aviation authorities. Techniques such as chevron nozzles, fluidic injection, and acoustic liners have been proposed and implemented to weaken large-scale turbulent structures and reduce noise radiation (Brown and Bridges, 2006; Saiyed et al., 2000). However, the complexity of turbulent jet flows and their strong non-linear interactions with acoustics continue to make jet noise prediction and control an ongoing challenge in aeroacoustics research.

2.4.1 Compressible Flow in Convergent Nozzles

As seen in the literature review, compressible flows are incorporated into the flows with Mach numbers equals to or greater than 0.3 ($M = U/c \geq 0.3$), where U is the flow velocity and c is the speed of sound, defined in Eq. 2.1. If the variation in density is substantial, due to the equation of state (Eq. 2.3), then the variations in temperature and pressure are also substantial. Large temperature variations imply that the energy equation can no longer be ignored. Consequently, the governing equations is doubled from two basic equations to four (mass-balance, momentum, thermal energy, and equation of state). According to White and Corfield (2006); White (2011) the variables to be solved comprehend into pressure, density, velocity components, and temperature (p, ρ, $\vec{V}$, and T) due to compressible effects.

$$PV = mRT \therefore P = \rho RT\,. \tag{2.3}$$

Mach number is a non-dimensional parameter with great importance in compressible flow characterization and analysis. This dimensionless quantity honors the physicist Ernst Waldfried Josef Wenzel Mach (1838-1916) and accounts the ratio of fluid velocity over the sound speed of the medium. Once the cases presented here comprehend from $M \approx 0.7$ up to $M \approx 0.8$, the flow behavior is considered in subsonic or in transonic regime, where the density effects are important and does not present shockwave.

In such situations, the main assumption carried out in further analysis is the adoption of an adiabatic reversible flow approach, or isentropic flow. For that, some properties are adopted as constant, such as: the specific gas constant ($R = c_p - c_v = 287\,[J/kg.K]$) and the specific heat ratio ($\gamma = c_p/c_v = 1.4$), both of them for air.

The variation in entropy can be calculated by means the first and second law of Thermodynamics (Incropera et al., 2008; Cengel and Cimbala, 2013). For a pure substance, it turns:

$$Tds = dh - \frac{dp}{\rho}\,, \tag{2.4}$$

where dh is the differential of enthalpy and can be expressed by $dh = c_p dT$ for an ideal gas. Combining Eq. 2.3, Eq. 2.4, and solving ds, it becomes:

$$\int_1^2 ds = \int_1^2 c_p \frac{dT}{T} - R \int_1^2 \frac{dp}{p}\,, \tag{2.5}$$

where c_p is assumed constant, then:

$$s_2 - s_1 = c_p \ln \frac{T_2}{T_1} - R \ln \frac{p_2}{p_1} = c_v \ln \frac{T_2}{T_1} - R \ln \frac{\rho_2}{\rho_1}\,, \tag{2.6}$$

Once the problems investigated in this work deals with subsonic flow ($M < 1$), the hypothesis of isentropic flow is adopted ($s_1 = s_2$), which produces the following relation:

$$\frac{p_2}{p_1} = \left(\frac{T_2}{T_1}\right)^{\frac{\gamma}{\gamma-1}} = \left(\frac{\rho_2}{\rho_1}\right)^{\gamma}\,. \tag{2.7}$$

As mentioned by White and Corfield (2006); White (2011); Cengel and Cimbala (2013), this first relation forms the cornerstone of compressible fluid dynamics and is essential to analyze, a priori, flow through a series of devices such as nozzles, diffusers, and supersonic wind tunnels. It is frequently used in the simulated cases, presented in 4 for verification of results and numerical validation with experiments.

Other relations used during this work can be found by means the adiabatic, isentropic and steady flow. Assuming the fluid in a specific streamline, the energy equation can be expressed by the Eq. 2.8, in its steady state form with no heat transfer and work.

$$h_1 + \frac{V_1^2}{2} + gz_1 = h_2 + \frac{V_2^2}{2} + gz_2 = h_0\,, \tag{2.8}$$

where, h is the enthalpy of the gas, V is the velocity, gz is the parcel responsible for the gravity potential energy, that can be neglected for air, if compared with the values of enthalpy and velocity for transonic flows.

The stagnation enthalpy (h_0) is the maximum value achieved by the enthalpy in its adiabatic stagnation. Based on this, for an ideal gas $h = c_pT$ and $h_0 = c_pT_0$, which gives:

$$c_pT + \frac{V^2}{2} = c_pT_0\,, \tag{2.9}$$

where, dividing RHS and LHS by c_pT, gives:

$$1 + \frac{V^2}{2c_pT} = \frac{T_0}{T}\,, \tag{2.10}$$

where, by ideal gas law, $c_pT = \gamma R/(\gamma - 1)T = a^2/(\gamma - 1)$, which modify the Eq. 2.10 into:

$$1 + \frac{(\gamma - 1)V^2}{2a^2} = \frac{T_0}{T}, \tag{2.11}$$

where, introducing the Mach number, gives:

$$\frac{T_0}{T} = 1 + \frac{(\gamma - 1)}{2}M^2\,. \tag{2.12}$$

Continuing in the isentropic flow theory, other relations can be obtained by the combination of Eq. 2.12 and Eq. 2.7, which gives:

$$\frac{p_0}{p} = \left[1 + \frac{(\gamma - 1)}{2}M^2\right]^{\frac{\gamma}{\gamma-1}}\,, \tag{2.13}$$

$$\frac{\rho_0}{\rho} = \left[1 + \frac{(\gamma - 1)}{2}M^2\right]^{\frac{1}{\gamma-1}}\,. \tag{2.14}$$

These relations (Equations. 2.12, 2.13, and 2.14) display a role of the specific heat ratio (γ) as the exponent of all relations. This exponent dictates the "stiffness" of the fluid's response to changes in pressure, temperature, and density in compressible flows.

In reference to stagnation conditions, the use of the subscript '0' (p_0, T_0, ρ_0) indicates a relationship to stagnation conditions. Stagnation properties are the properties the fluid would have if it were brought to rest isentropically. These values are constant along a streamline in an isentropic flow and serve as a useful reference point for calculating the local static properties at any given point in the flow. The Figure 2.7 presents a graph of the evolution of the adiabatic and isentropic relations by Mach number, as depicted the regions of cases presented in this work ($M_a = 0.7$ and $M_a = 0.8$). Notice that, for convenience, is presented the ratio of the property by its stagnation value, i.e. the inverted relations of Equations. 2.12, 2.13, and 2.14.

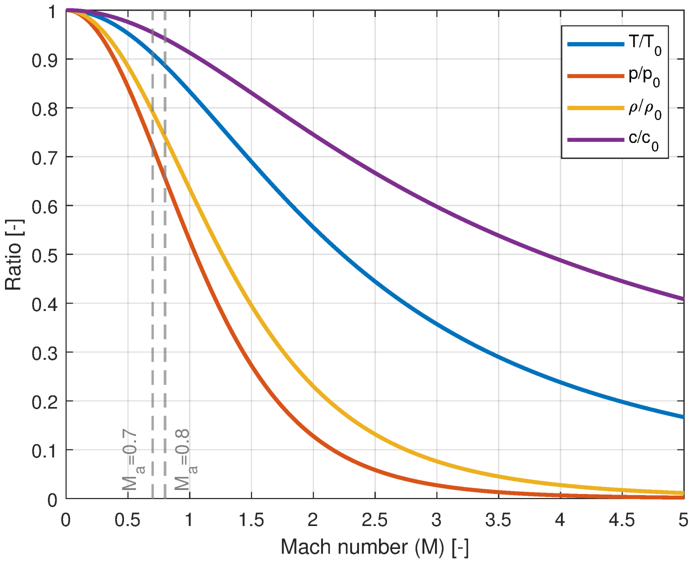

Figure 2.7: Adiabatic and isentropic relations by Mach number for a $\gamma = 1.4$, with acoustic Mach used in simulations (M_a).

2.4.2 Turbulence in Fluid Flows

One of the biggest challenges in Fluid Mechanics is to study and understand the Turbulence in fluids. Considering a dynamic system with great instabilities and unpredictability (in instantaneous cases), these types of flow are present in our life, being part of natural or artificial phenomena. The Turbulence is widely discussed in the scientific middle. As noted by Silveira Neto (2020), it is a process with high nonlinearities and complicated instantaneous prediction. However, it can be modeled, predicted, and measured in an averaged (filtered) analysis. The Turbulence is widely discussed in the technical and scientific community. For dealing with a transformation process extremely nonlinear, Turbulence can be modeled, predicted and gauged in averaged patterns; this turns it in, according to Silveira Neto (2020), in a philosophical meaning, a chaotic deterministic process.

Observations initiated by Leonardo da Vinci around the sixteenth century, as shown in the Figure 2.8, one notices that there are some well-described details and a mount of scales, eddies and turbulent structures represented by the artist. The sketch shows a frozen snapshot described in a pure artistic draft; da Vinci had used the bubble path and the distortion of two-phase (air and water) interface as flow tracers, which reveal the pathlines and fluid flow behavior.

The Reynolds number, a dimensionless quantity that honors Osborne Reynolds (1842-1912), is used as a main dimensionless parameter in defining the possible presence of turbulence in fluid flows. The word 'possible' was intentionally used due to some experiments in

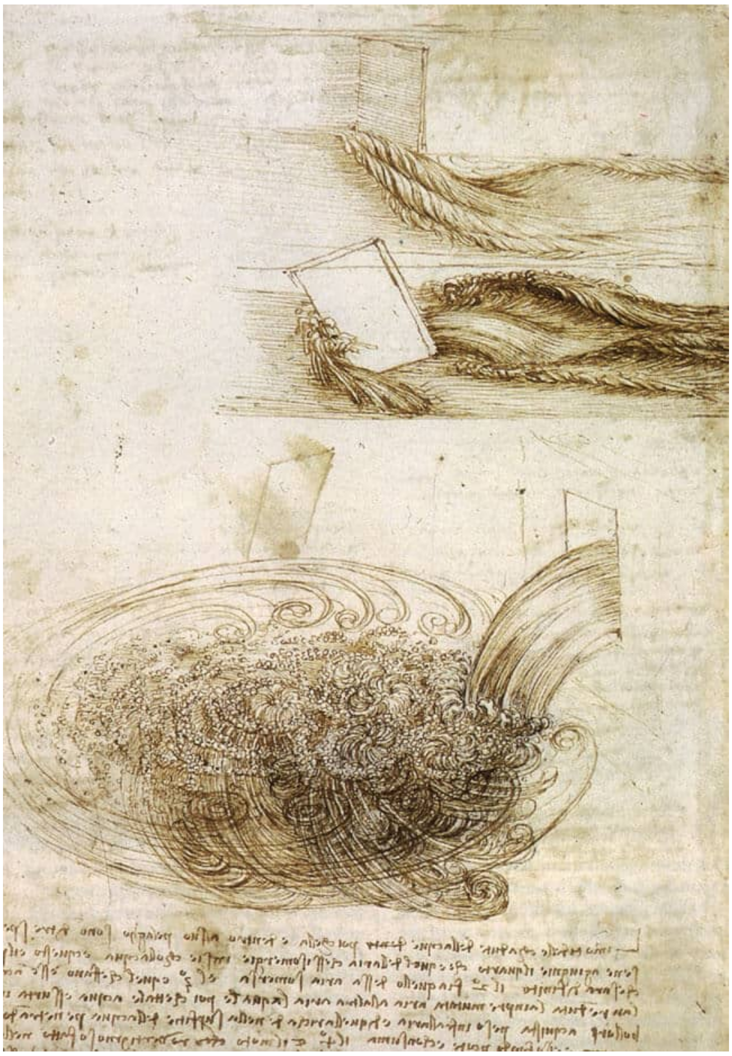

Figure 2.8: Sketches by Leonardo da Vinci in the XVI century, showing different length scales of turbulence in the water passing obstacles and a waterfall. (da Vinci, XVI)

high Reynolds numbers that present the behavior of laminar flows. Reynolds number defines a relation between inertial and viscous tensions, as expressed in Eq. 2.15. The higher the Reynods number, the more instabilities appear in the flow, and as a 'trigger' mechanism, according to White and Corfield (2006), the amplification of these instabilities occurs.

$$Re = \frac{\rho V L}{\mu} = \frac{V L}{\nu}\,, \tag{2.15}$$

where, ρ is the density of the fluid, V is the flow velocity, L is the characteristic length, μ and ν are the dynamic and kinematic molecular viscosity, respectively.

Several situations, that present small Reynolds numbers, the viscous forces overtake the inertial forces and, based on it, the instabilities are damped and the flow is named laminar. On the other hand, with the increase in Re, inertial forces begin to predominate and, by inducing strong nonlinear interactions with the flow variables, the growth of instabilities is amplified, ultimately leading the flow to become in transition and then, fully turbulent.

Although complex, the phenomenon of turbulence in fluids is extremely necessary and widely encountered in natural phenomena as well as in industrial applications. The unpredictable nature of velocity and pressure fluctuations, for example, enhances thermal diffusion over a heated plate, as pointed by Incropera et al. (2008); Cengel and Cimbala (2013), or contributes to drag reduction in a bluff body, according to White (2011). The knowledge around the turbulence in fluids is a key to produce more optimized designs, such as: heat exchangers, low-drag vehicles, or, as matter of this work, more silent nozzles.

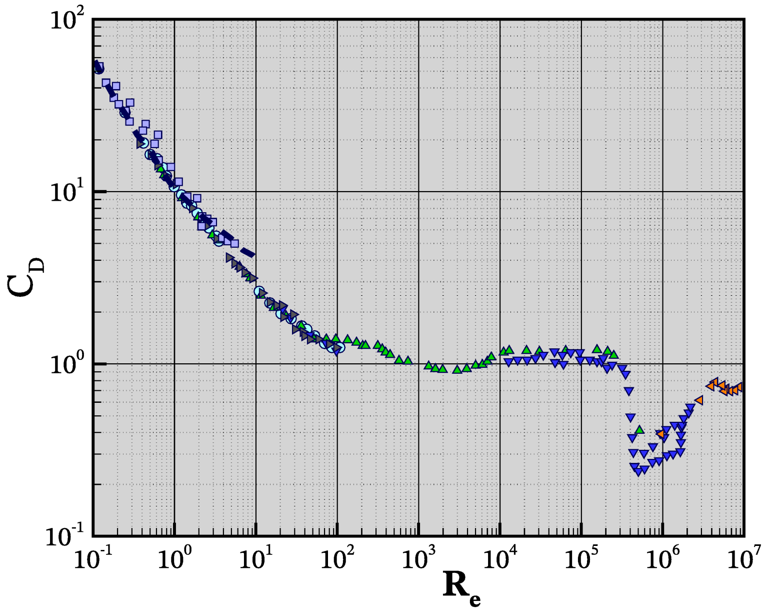

Figure 2.9: Drag coefficient due to flow around a cylinder of various diameters. (Katopodes, 2019).

For centuries, the chaotic nature of turbulence has been reported in the scientific community and, with advances in experimental approaches, design capabilities, and the evolution of mathematical models, in recent years it has been possible to predict several fluid dynamic solutions with good accuracy. However, according to Silveira Neto (2020), the characteristics of turbulent flow go beyond the presence of vortices/eddies. The main characteristics of Fluid Turbulence are listed as:

- It is composed of vortical structures — since the literature points to the presence of vortices in the flow, these may also occur in unstable or transitional laminar flows, as the statistical concept of a vortex requires invariance of statistical moments throughout the vortex region;
- It is composed of multiple scales — the multiplicity of spatial and temporal scales is related to the vortical structures, their sizes, frequencies, and lifetimes within the flow. A fully turbulent flow is permeated by structures ranging from the order of the characteristic length of the geometry of the problem to the smallest scales (Kolmogorov scale);
- It can be modeled as a continuous phenomenon — provided that the length of the smallest structures is greater than the molecular mean free path, the continuum hypothesis can be adopted in turbulence modeling;
- It accelerates molecular diffusion of information — due to the multiple degrees of freedom in flow variables such as velocity, pressure, temperature, and concentrations, spatiotemporal fluctuations enhance the diffusive process of these quantities;
- It occurs at high Reynolds numbers — advective effects are nonlinear and responsible for the onset and maintenance of turbulence. An increase in Reynolds number promotes this nonlinear interaction, giving rise to flow instabilities;
- It is three-dimensional and rotational — the interaction and amplification of instabilities disturb variables in all flow directions, leading to vorticity fluctuations. The stretching of vortical structures is a purely three-dimensional and rotational mechanism;
- It is transformative — due to the coexistence of different scales, turbulence, in regions with high-wavenumber and high-frequency scales, promotes the transformation of flow kinetic energy into an increase in internal energy;
- It can be regarded as deterministic chaos — in principle, the solutions of the Navier–Stokes equations would provide exact and deterministic results, if initial and boundary conditions were prescribed with the same precision. However, due to strong nonlinearities, the process of turbulence development becomes chaotic and extremely sensitive to initial conditions. Nonetheless, it remains statistically predictable.

2.4.2.1 The Scales of Turbulence

A developing turbulent flow begins with the amplification of disturbances present in the flow, which eventually causes the first instabilities. With the continuous injection of kinetic energy into the system, simultaneous interactions among the various scales of motion occur until a statistically steady regime is established. Figure 2.10 illustrates the spectral density distribution of specific turbulent kinetic energy as a function of wavenumber. It can be observed that, as time progresses, the spectrum broadens, and at t_4 the slope of the curve exhibits the $k^{-5/3}$ behavior, in accordance with Kolmogorov's theory. At this stage, t_4, the flow is considered to be in a fully developed turbulence state.

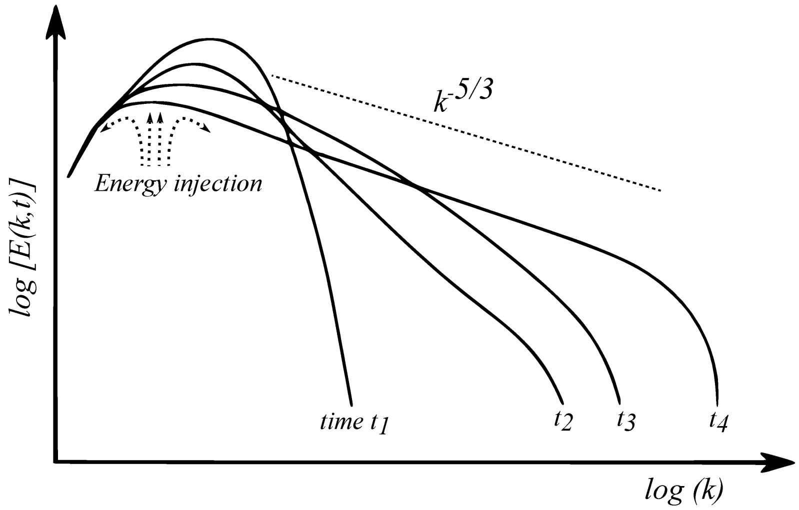

Figure 2.10: Sectral density of the specific turbulent kinetic energy E as function of the wave number k and time t. (Adapted from Silveira Neto (2020)).

With the full development of turbulence, the injection of turbulent kinetic energy is sustained within a certain range of scales. However, the simultaneous and nonlinear interactions among scales —- ranging from the largest (with characteristic lengths on the order of the geometry of the problem) to intermediate and smaller ones -— maintain the energy spectrum broad until its abrupt decay at a given wavenumber k. Since the wavenumber refers to the number of structures present per unit length, it follows that structures with higher wavenumbers correspond to those of extremely small size.

The smallest structures present in the flow are referred to as Kolmogorov structures, named after the 20th-century Soviet mathematician Andrei Kolmogorov. These structures are exceedingly small, and when examining the Reynolds number associated with them, one observes a predominance of viscous effects over inertial effects; in other words, for Kolmogorov structures, $Re \approx 1$. This condition enables the transformation of turbulent kinetic energy into other forms of energy through viscous diffusion. However, the length, time, velocity, and vorticity scales associated with these structures vary from one flow to another.

As presented by Silveira Neto (2020), the greater is the Reynolds number for a specific flow, the smaller are the length (l_d), time (τ), velocity (u), and kinetic energy (e) scales associated to the Kolmogorov scales, according to Equations 2.16 to 2.19,

$$\frac{L}{l_d} = Re_L^{3/4}, \tag{2.16}$$

$$\frac{t}{\tau} = Re_L^{1/2}, \tag{2.17}$$

$$\frac{U}{u} = Re_L^{1/4}, \tag{2.18}$$

$$\frac{\omega}{W} = Re_L^{1/2}, \tag{2.19}$$

$$\frac{E}{e} = Re_L^{1/2}, \tag{2.20}$$

where, L, t, U, W e E, are the scales for length, time, velocity, vorticity, and kinetic energy related to the integral scales of the flow, respectively; l_d, τ, u, ω e e, are the scales for length, time, velocity, vorticity, and kinetic energy related to the Kolmogorov scales, respectively; Re_L is the Reynolds number of the integral scales of the problem.

It can be observed from these equations that the length, time, velocity, and energy scales decrease as the Reynolds number increases. The increase in vorticity (ω) is proportional to the increase in Re_L, due to the higher rotational levels of the smallest turbulent structures as Re_L increases, i.e. the smaller structures present a high vorticity, then high frequencies.

As described by Silveira Neto (2020), Pletcher et al. (2012) and Wilcox (1993), the reduction of length scales with increasing Reynolds number non-linearly amplifies the emergence of multiple degrees of freedom in the flow. According to Silveira Neto (2020), Eq. 2.21 expresses the number of degrees of freedom per unit volume, while Wilcox (1993) defines in Eq. 2.22 the approximate number of degrees of freedom for fluid flow in a channel,

$$\left(\frac{L}{l_d}\right)^3 = Re_L^{9/4}\,, \tag{2.21}$$

$$N_{dof} = 0{,}088(Re_L)^{9/4}\,, \tag{2.22}$$

where, L and l_d are related to the characteristic lengths of the larger and smaller eddies, respectively; and N_{dof} is the number of possible DOF (turbulent structures or eddies) in the flow.

Equation 2.21 establishes a fundamental relationship between the scales of turbulence and the Reynolds number. It states that the ratio of the volume of the largest eddies (L) to the smallest eddies (l_d) is proportional to the Reynolds number raised to the power of $9/4$. In a turbulent flow, energy is transferred from large, slow-moving eddies down to progressively smaller ones in a cascade until they reach a size where viscosity can dissipate their energy into heat. The term $(L/l_d)^3$ effectively represents the volume of this turbulent cascade and, therefore, the number of possible independent degrees of freedom needed to describe the flow's complexity. As a practical example, a turbulent jet flow of diameter of $0.05\,m$ at a Reynolds number of 1×10^6 will present a possible minimal length scale of order $1.6 \times 10^{-6}\,m$.

Although the second derivation is derived from a channel, the Equation 2.22 directly translates this physical relationship into a quantifiable measure: the probable number of degrees of freedom (N_{dof}) that can occur in the flow. Both equations present a proportionality in order of Reynolds power of $9/4$. In the context of turbulent flow, an increasing Reynolds number signifies a higher fluid velocity or larger scale, which leads to more chaotic and unpredictable flow. This means the number of independent variables required to describe the flow's chaotic motion – its degrees of freedom – grows rapidly and non-linearly. This explains why simulating or solving for high-Reynolds number turbulent flows is computationally intensive and challenging, as the number of active turbulent eddies becomes enormous.

These two equations describe the complexity of a turbulent fluid flow by relating the number of turbulent scales to the Reynolds number. They show that as the Reynolds number increases, the flow becomes significantly more complex and chaotic and they are a good starting point to define some assumptions in CFD simulations, for instance, domain definition and discretization.

2.4.2.2 Mathematical Models for Turbulence

The governing equations of Fluid Mechanics are described by the following equations. For a Newtonian, compressible, single-phase, isothermal fluid with constant properties, these equations fundamentally represent the conservation of mass (continuity), Equation 2.23, and the conservation of linear momentum, Equation 2.24, both presented in their index form,

$$\frac{\partial \rho}{\partial t} + \frac{\partial \rho u_i}{\partial x_i} = 0\,, \tag{2.23}$$

$$\frac{\partial \rho u_i}{\partial t} + \frac{\partial}{\partial x_j}(\rho u_i u_j) = -\frac{\partial p}{\partial x_i} + \frac{\partial}{\partial x_j}\left[\mu\left(\frac{\partial u_i}{\partial x_j} + \frac{\partial u_j}{\partial x_i}\right) - \frac{2}{3}\mu\delta_{ij}\frac{\partial u_k}{\partial x_k}\right] + f_i\,, \tag{2.24}$$

where, μ is the dynamic viscosity of the fluid, δ_{ij} is the Kronecker delta, which is 1 when $i = j$ and 0 otherwise, and f_i represents any source term of linear momentum.

Assuming an isothermal flow, these equations are sufficient to represent the physics of fluid flows at any Reynolds number and in any geometry. However, since they are partial differential equations (PDEs) that are difficult to solve analytically, numerical-computational techniques can be applied to obtain solutions, provided that the criteria described in Equations 2.21 and 2.22 are respected.

Regarding the computational cost involved in Direct Numerical Simulation (DNS), even for simple laminar flows, the demands can be considerable. As an example from Silveira Neto (2020), a two-phase problem involving an air bubble rising with a diameter of $3\,mm$ at a Reynolds number of 150 requires a discretization of around 780,000 cells per unit volume. This problem is manageable with current computing technology, as a standard desktop computer has the processing power to solve it.

However, for a channel flow at the same Reynolds number (150), the discretization escalates to tens of millions of control volumes per unit volume, making the problem much more expensive computationally. While not impossible, it requires a high-performance computing cluster, as noted by Wilcox (1993).

This approach is known as Direct Numerical Simulation (DNS), where all scales of the flow are explicitly calculated, and all turbulent structures are resolved in the solution. This ensures a high-fidelity representation of the flow physics but at an extremely high computational cost, making it impractical for most industrial applications and high-Reynolds-number flows. DNS is primarily used for fundamental research, helping to understand flow physics and to validate and develop less computationally expensive turbulence models.

On the other hand, a Direct Numerical Simulation (DNS) of an atmospheric flow, such as those used in weather forecasting, would lead to an absurdly large discretization and require solving linear systems on the order of 10^{32} simultaneous equations, according to Silveira Neto (2020). This type of problem is currently unfeasible, if not impossible.

Because of this difficulty, the scientific community has dedicated itself to finding methodologies that "model more" and "compute less" the effects of turbulence and its structures.

2.4.2.3 Unsteady Reynolds Navier Stokes Equations (URANS)

Assuming that any flow property (ϕ) can be represented as the sum of a mean component and a fluctuating component, $\phi = \overline{\phi} + \phi'$, as exemplified for the velocity component u in Figure 2.13, it becomes possible to use time-averaged methodologies. The original Navier-Stokes equations, which describe fluid motion, are then time-averaged using this decomposition.

This type of consideration makes it possible to model the diffusive effects of Turbulence at a low computational cost, if compared to DNS approach. Proposed by Reynolds (1895) and Boussinesq (1877), the filtering process through the application of a temporal averaging filter is expressed in the following equations. Equations 2.25 and 2.26 are, respectively, the conservation of mass and the conservation of linear momentum with applied temporal averaging, conferring a damped behavior for rapid transients, as qualitatively demonstrated in Fig. 2.13,

$$\frac{\partial \overline{u_i}}{\partial x_i} = 0\,, \tag{2.25}$$

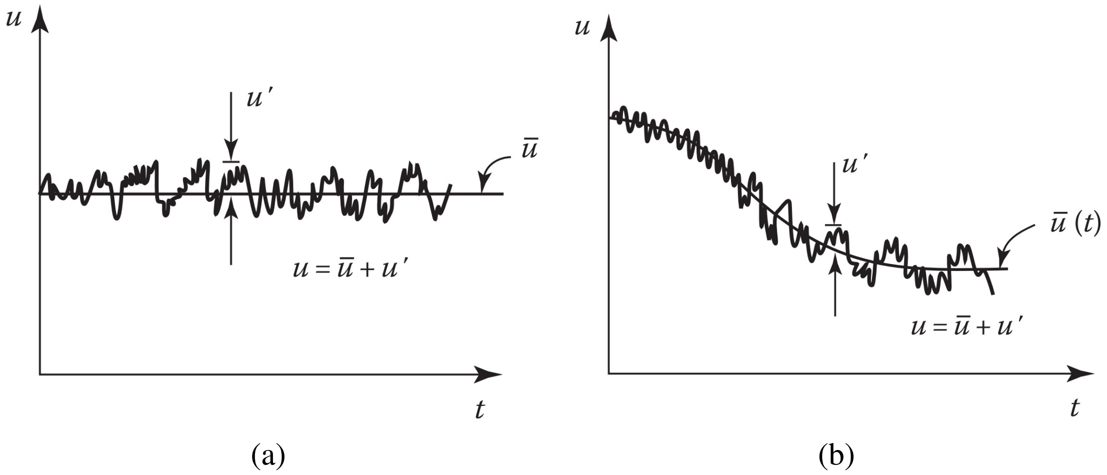

Figure 2.11: Velocity component u, mean velocity $\overline{u}$ and fluctuation u': steady state (a), and unsteady state (b) (Pletcher et al., 2012).

$$\frac{\partial \overline{u_i}}{\partial t} + \frac{\partial}{\partial x_j}(\overline{u_i}.\overline{u_j}) = -\frac{1}{\rho_0}\frac{\partial \overline{p}}{\partial x_i} + \frac{\partial}{\partial x_j}\left[\nu\left(\frac{\partial \overline{u_i}}{\partial x_j} + \frac{\partial \overline{u_j}}{\partial x_i}\right) - \overline{u_i' u_j'}\right] + \frac{f_i}{\rho_0}\,. \tag{2.26}$$

The Reynolds averaging process gives rise to the methodology of Unsteady Reynolds Average Navier-Stokes (URANS) equations, or in its steady state RANS, which is explained in detail by Silveira Neto (2020) and Pletcher et al. (2012). The use of this type of filtering (temporal averaging) introduces the tensor $\overline{u_i' u_j'}$, made up of six unknown variables. This is called the Reynolds stress tensor and it is placed on the RHS of the equation, where it is treated as a diffusive process associated with turbulent effects. The closure models that handle this new diffusion process are known as eddy viscosity-based models (ν_t).

Other models, such as the Reynolds Stress Model (RSM), can account for the transport of the components of the Reynolds stress tensor directly. According to Silveira Neto (2020), this type of modeling does not directly use the concept of turbulent viscosity.

2.4.2.4 Turbulence in Jets

Several studies were conducted to elucidate the turbulence around the mixing jets. Quite a number of publications and results are disposed in literature. The transition to turbulence, identified by Reynolds (1883), originates from the appearance of instabilities in a flow that is initially stable or in laminar condition. The highly non-linear advective effects are responsible for the amplification of perturbations and the generation of instabilities, according to White and Corfield (2006); Lesieur (2008); Silveira Neto (2020). The intense motion of the eddies (or turbulent structures) amplify and interact with each other, inducing a turbulent flow.

Mixing jets are included in the class of free shear flows. This class consists of transitional flows that are characterized by the absence of walls or obstacles. Their origin is linked to flow over submerged bodies (wakes), expansion in orifices or nozzles (mixing jets), or the merging of currents with different velocities (mixing layers). The transition in free shear flows is similarly characterized by the presence of so-called *coherent structures*, which exhibit a high degree of organization, leading to flow anisotropy and inhomogeneity. Figure 2.12 presents a Schlieren photograph of a turbulent subsonic jet, which beautifully captures the complex structure of the mixing region immediately downstream of a nozzle (Van Dyke, 1982). The visualization technique reveals gradients in the refractive index of the air, which correspond to variations in density and, therefore, pressure or temperature. These gradients make visible the intricate turbulent structures that develop as the high-speed jet interacts with the surrounding ambient air.

At the nozzle exit, the flow begins as a nearly uniform core, but it quickly becomes unstable due to Kelvin–Helmholtz (K-H) instabilities. These instabilities roll up into coherent vortex rings that grow, distort, and eventually break down into smaller turbulent eddies as the jet propagates downstream (Pope, 2000). This turbulent mixing process is the primary physical mechanism responsible for subsonic jet noise generation, often referred to as jet mixing noise. As mentioned by (McGuirk and Feng, 2021) the main noise source in jets occurs in the region downstream to the core length.

The instabilities that develop in this class of flows are called shear instabilities, since, according to linear stability theory, they can develop even in the hypothetical situation of inviscid flows. Lord Rayleigh (John William Strutt), established the inflectional criterion of the velocity field as a necessary condition for the generation of instabilities in free shear flows. In flows where instabilities develop under the influence of a wall, the transition occurs differently despite the absence of an inflectional velocity profile, presenting instabilities of another nature

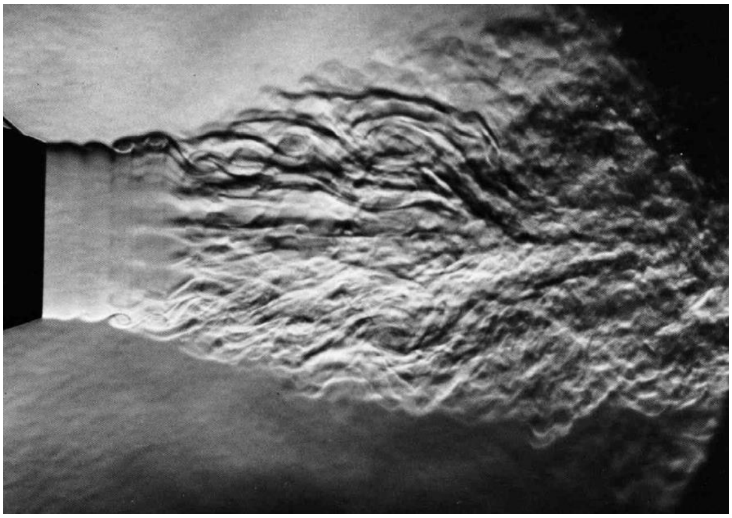

Figure 2.12: Development of a circular mixing jet in an experimental visualization (Van Dyke, 1982).

(Smagorinsky, 1963). Silveira Neto (2020) states that the transition can also have other origins, as the formation of instabilities can be caused by viscous effects (Tollmien-Schlichting or TS waves), or effects of rotation or thermal convection.

The transition in jets is characterized by the formation of primary Kelvin-Helmholtz-type instabilities, which in turn induce the formation of secondary filaments. The interaction of the longitudinal counter-rotating filaments with the turbulent structures will induce the formation of transverse oscillations, which amplify and eventually lead the flow to three-dimensional turbulence, as seen in the photograph by Van Dyke (1982).

Once the instantaneous movement of flow in a jet is nearly unpredictable, due to the chaotic behavior of turbulent flow, the mean field is relatively easy to predict in the core jet development. Proença (2018) presents a comparison between experimental data and a Gaussian mean profile of the jet velocity – Equation 2.27.

$$U(x,y)=\begin{cases} U_{\max}\exp\left[-\dfrac{(y\pm\delta_c/2)^2}{(\delta_\beta/2)^2}\right], & \text{if } |y|>\delta_c/2,\\ U_{\max}, & \text{if } |y|\leq\delta_c/2,\end{cases} \tag{2.27}$$

where, U_{max} is the maximum velocity in centerline, δ_β is the shear layer half-width, δ_c is the potential core width, and x and y are the axial and transversal coordinates. These parameters must be determined by numerical simulations or by means tabled experimental data, as the study of Witze (1974), or in a direct experimental observation (Morris and Zaman, 2010).

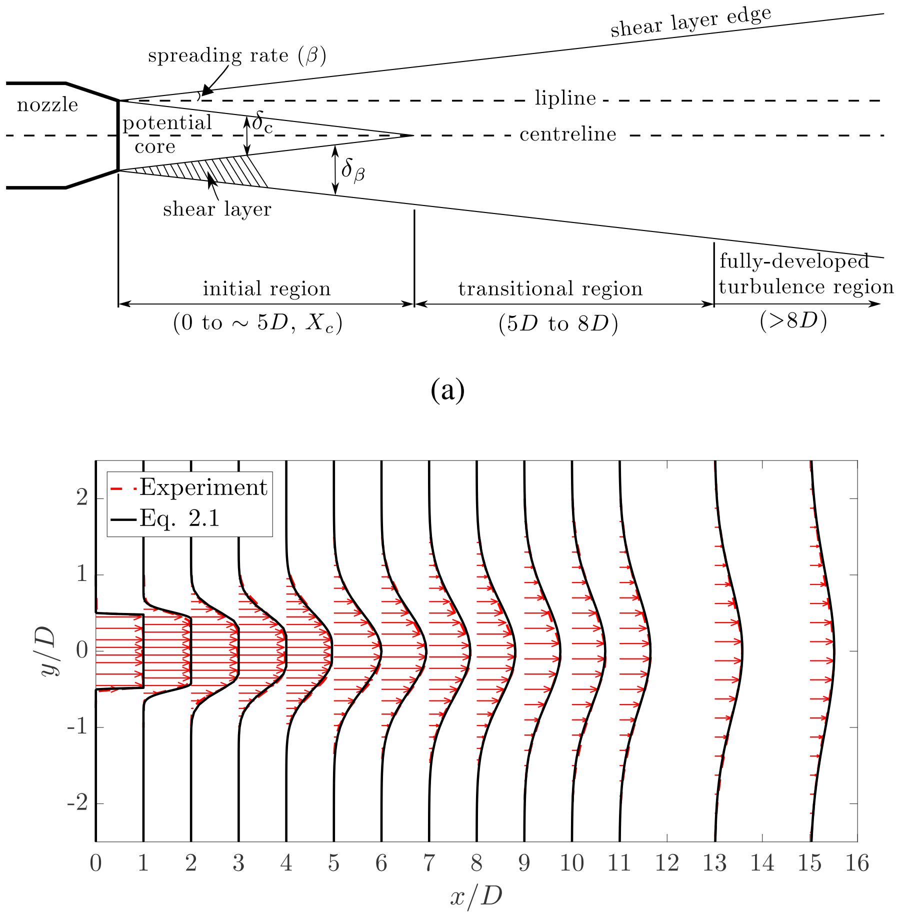

(a)

(b)

Figure 2.13: Diagram of a free jet in steady state in (a), and mean velocity profiles of a static, subsonic, round jet in (b). Adapted from (Proença, 2018).

2.4.2.5 Acoustic Properties

As described in Table 2.1, a wide range of acoustic power levels are perceptible to the human ear and they are present in everyday situations. This demonstrates that our hearing exhibits a logarithmic sensitivity to these levels; that is, from the threshold of hearing to the threshold of pain, there is a variation spanning 12 orders of magnitude in values of pressure. The SPLs, which refer to the amplitude of the pressure wave, may range from the order of μPa up to the order of hPa.

One way to linearize this scale is by using the log_{10} scale. The SPL is expressed in the unit of decibel (dB), which, as shown by Howe (1998); Gerges (2000), corresponds to one-tenth of the exponent in base 10, that is, $1\,dB = 10^{0.1} \approx 1.26$. This means that an increase of $1\,dB$ in SPL corresponds to a variation of 1.26 times the value of the sound pressure and, consequently, an increase of $3\,dB$ corresponds to a doubling of the SPL.

The acoustic intensity is proportional to the square of the acoustic pressure ($I = P^2_{rms}/\rho_0 c_0$), and the Sound Pressure Level (SPL), in dB, is given by:

$$SPL = 10 \log \left(\frac{P^2_{rms}}{P^2_0} \right) = 20 \log \left(\frac{P_{rms}}{P_0} \right) \,, \tag{2.28}$$

where P_0 is the human hearing threshold at $1000\,Hz$, which corresponds to the value of $20\,\mu Pa$ in pressure.

The Sound Intensity Level (SIL) represents the amount of energy per unit area carried by the sound wave, and its unit is expressed in W/m^2:

$$SIL = 10 \log \left(\frac{I}{I_0} \right) \,, \tag{2.29}$$

where I is the sound intensity level, expressed in W/m^2, and I_0 is the standard reference intensity in air, relative to the human hearing threshold ($10^{-12}\,W/m^2$) at $1000\,Hz$.

Another important acoustic quantity is the Sound Power Level (SWL).

$$SWL = 10 \log \left(\frac{W}{W_0} \right) , \tag{2.30}$$

where W is the acoustic power expressed in Watt and W_0 is the reference power value, corresponding to $10^{-12}\,W$.

Table 2.2: Increase in combined sound level as a function of level difference between two sources.

Level Difference Δ (dB)	Increment Over Louder Source (dB)
0	3.01
1	2.54
2	2.12
3	1.76
5	1.19
10	0.41
15	0.14
20	0.04
30	$\approx$ 0.00

The Figure 2.14, illustrates how the total sound level changes when a second sound source is added to an existing one. It specifically shows the increase in decibels (dB) over the louder source as a function of the level difference between the two sources ($\Delta\, dB$).

When the two sound sources have equal levels ($\Delta = 0dB$), the total sound level increases by $+3\,dB$ over the level of a single source. This is a fundamental principle of decibel addition, as doubling the acoustic power results in a $3\,dB$ increase. For instance, if two speakers each produce $80\,dB$, together they will produce 83 dB. Thus, the resulting SPL is calculated through a logarithmic process, and the provided Table 2.2 gives a practical method for quick estimation. This table shows the increment over louder source required to find the combined SPL, based only on the level difference (Δ in dB) between the two sources.

On the other hand, as the level difference between the two sources increases, the contribution of the quieter source becomes less significant. The curve shows that when the level difference (Δ) is $10\,dB$ or more, the addition is negligible (less than $0.5\,dB$). This is a widely used "rule of thumb" in Acoustics: if a second sound is $10\,dB$ quieter than the first, it has a minimal impact on the overall sound level. For example, if a jackhammer (or a pneumatic drill) is $100\,dB$ and a nearby car is $90\,dB$, the total sound level is still approximately $100dB$, dominated by the loudest source (Duarte, 1985; Teodoro, 1985).

The curve presents an asymptotic behavior to the X-axis, meaning that it gets closer and closer to zero but never quite reaches it. This demonstrates that even a very quiet sound source

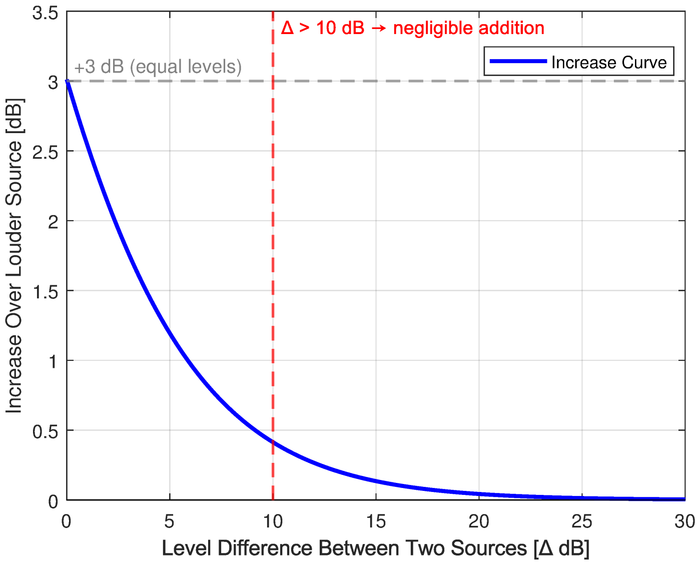

Figure 2.14: Increment in dB of the sum of two acoustic sources.

technically adds a minuscule amount to the total sound level, though the contribution quickly becomes imperceptible in a practical sense.

2.4.2.6 Lighthill's Acoustic Analogy

With the advent of commercial jet aircraft in the 1950s, such as the pioneering de Havilland DH-106 Comet, a scientific motivation emerged to study the mechanisms of aerodynamic noise generation and propagation. During the same period, the mathematician James Lighthill presented studies on the mathematical formulation of the main terms for converting the kinetic energy of a flow into aerodynamic noise Lighthill (1952). Lighthill's work, titled "On Sound Generated Aerodynamically II - Turbulence as a Source of Sound" Lighthill (1956), initiated the field of Aeroacoustics, which has since contributed significantly to the development of techniques and methods for understanding this physical phenomenon.

The theory of aerodynamic sound was initially developed through an analogous formulation of the Navier-Stokes equations Howe (2003). This set of equations and assumptions is known as Lighthill's Acoustic Analogy, proposed by Lighthill (1952). This approach results in a non-homogeneous equation where the source terms are most significant in regions with greater vorticity (turbulent regions), particularly in isothermal flows at high Reynolds numbers. For cases involving strong thermal gradients, the entropy term (discussed later) also becomes a dominant factor in noise production. Figure 2.15 illustrates the physics described by Lighthill's initial studies in Aeroacoustics.

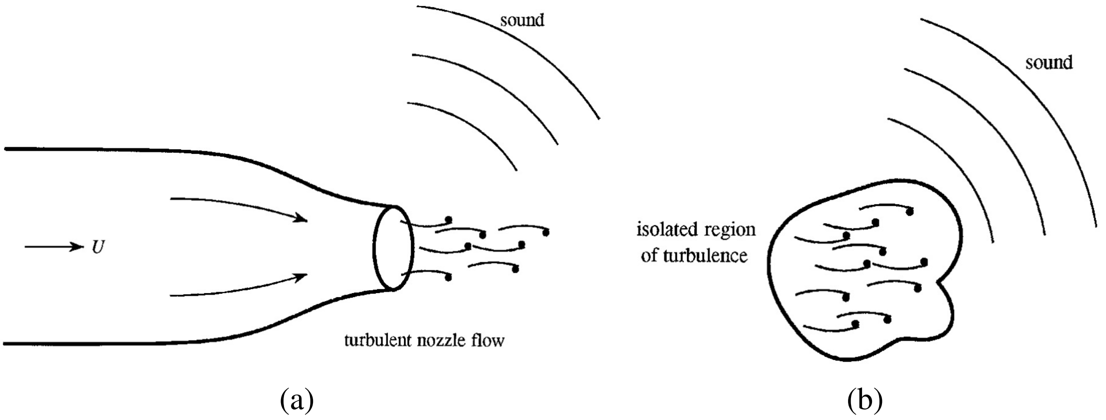

Figure 2.15: Regions of noise conversion adopted in Lighthill's analogies; Sound produced by turbulent jets (a) and sound produced by rotational regions (b). (Adapted from Howe (2003)).

To derive Lighthill's equations, one must begin with the mass conservation equation in its complete form (Equation 2.31) and the momentum conservation equation, neglecting the terms of body force and gravitational effects (Equation 2.32),

$$\frac{\partial \rho}{\partial t} + \vec{\nabla}.(\rho \vec{V}) = 0\,, \tag{2.31}$$

$$\frac{\partial (\rho \vec{V})}{\partial t} + \vec{\nabla}.(\rho \vec{V}\vec{V}) = -\nabla p + \vec{\nabla}.\overline{\overline{\tau}}\,, \tag{2.32}$$

where, in its vector formulation, $\vec{V}$ denotes the fluid particle velocity vector, ρ is the fluid density, p is the pressure term, and $\overline{\overline{\tau}}$ is the viscous stress tensor acting on the fluid particle.

By differentiating Equation 2.31 with respect to time and applying the divergence operator to Equation 2.32, one obtains:

$$\frac{\partial^2 \rho}{\partial t^2} + \frac{\partial}{\partial t}\vec{\nabla}.(\rho \vec{V}) = 0\,, \tag{2.33}$$

$$\vec{\nabla}.\frac{\partial(\rho\vec{V})}{\partial t}+\vec{\nabla}.[\vec{\nabla}.(\rho\vec{V}\vec{V})]=-\nabla^2 p+\vec{\nabla}.(\vec{\nabla}.\overline{\overline{\tau}})\,. \tag{2.34}$$

Assuming the commutation between the temporal derivative and divergence operators, Eq. 2.33 can be subtracted from Eq. 2.34, from which it follows that:

$$\frac{\partial^2\rho}{\partial t^2}-\vec{\nabla}.[\vec{\nabla}.(\rho\vec{V}\vec{V})]=\nabla^2 p-\vec{\nabla}.(\vec{\nabla}.\overline{\overline{\tau}})\,. \tag{2.35}$$

By adding the expression $-c_0^2\nabla^2\rho'$ to Eq. 2.35, where c_0 is the speed of sound in the quiescent medium and ρ' denotes the density fluctuation of the fluid, and by rearranging the terms related to density on the right-hand side, one obtains:

$$\frac{\partial^2\rho}{\partial t^2}-c_0^2\nabla^2\rho'=\vec{\nabla}.[\vec{\nabla}.(\rho\vec{V}\vec{V})]+\nabla^2 p-\vec{\nabla}.(\vec{\nabla}.\overline{\overline{\tau}})-c_0^2\nabla^2\rho'\,. \tag{2.36}$$

Assuming the density in the temporal term is written as $\rho=\rho_0+\rho'$, where ρ_0 is the mean value of the quiescent atmosphere and constant in time, and isolating the operator $\vec{\nabla}$, Eq. 2.36 rewrites as:

$$\frac{\partial^2\rho'}{\partial t^2}-c_0^2\nabla^2\rho'=\vec{\nabla}.[\vec{\nabla}.(\rho\vec{V}\vec{V}-\overline{\overline{\tau}})]+\vec{\nabla}(p-c_0^2\rho')\,, \tag{2.37}$$

where, commonly presented in the literature in its indicial form, it results in the Lighthill's equation.

$$\frac{\partial^2\rho'}{\partial t^2}-c_0^2\frac{\partial^2}{\partial x_i^2}\rho'=\frac{\partial^2}{\partial x_i\partial x_j}T_{ij}\,, \tag{2.38}$$

where, the tensor T_{ij} is named Lighthill's stress tensor, as denoted by:

$$T_{ij}=\rho u_i u_j-\tau_{ij}+\delta_{ij}(p-c_0^2\rho')\,, \tag{2.39}$$

where, τ_{ij} is the viscous stress tensor and δ_{ij} is the Kronecker delta (which assumes 1 when $i=j$, 0 otherwise).

In a first analysis of Equation 2.38, on the LHS, we have the propagation of acoustic in its mathematical form in terms of density fluctuations (ρ'). On the RHS, we have the transformation and source terms of energy that make the Lighthill's stress tensor (T_{ij}). This tensor, for its own sake, is known as a source term or an acoustic transformation term, once it can account for the transformation of kinetic energy of the flow into acoustic energy. Notice that the term $\rho u_i u_j$ is a strongly nonlinear term and is more expressive in a more turbulent flow, the viscous stress tensor (τ_{ij}) can be interpreted as an acoustic difusion mechanism, and the term $\delta_{ij}(p - c_o^2\rho')$ is responsible for taking into account the irreversibilities of the system (entropy increase), according to Flabes Neto (2018).

Lawrence (2014) states that Lighthill's equation assumes a hyperbolic behavior in the wave propagation at the speed of sound in a medium at rest. As mentioned above, the RHS of Equation 2.39 models the external noise sources by means of turbulent fluctuations. Analyzing the terms of these partial differential equations, we can infer about the type of the noise source. The temporal term ($\partial/\partial t$) represent the effects of a monopole source, the term $\partial/\partial x_i$ acts as a dipole source, $\partial^2/\partial x_i x_j$ acts as a quadrupole, and $\partial^3/\partial x_i x_j x_k$ carries out the hexapole effects.

Other advances were achieved by means of the Lighthill's analogy, and they are related to the dimensional analysis of the simplified solutions of the Eq. 2.38. In this equation, the nonlinear term ($\rho u_i u_j$) is considered predominant, and this assumption is valid for isothermal flows at high Reynolds numbers. Taking into account the perceived noise by an observer in the far-field, according to Howe (1998), we have the named Lighthill's "eight power" law, or by other nomenclatures, Lighthill's v^8 law. As presented in Eq. 2.40, one notice that the acoustic intensity level is proportional to the speed of the jet powered by 8. Whilst the acoustic intensity is affected by the square of nozzle diameter, i.e. the bigger is the nozzle diameter the more acoustic power and intensity levels it produces in far-field, to the same jet velocity.

$$I(R) \approx \frac{\rho_s^2 U_j^8 D^2}{\rho_0 c_0^5 R^2}, \tag{2.40}$$

where, U_j is the jet velocity; ρ_s and ρ_0 are the air densities in the medium and in the standard atmosphere condition, respectively; D is the diameter of the nozzle and R is the distance of the observer from the source.

Such observation justifies the evolution of engines from turbojets to turbofans with high bypass ratio and their significant contribution in noise reduction. By means of the aeroacoustic point of view, is more reliable and efficient to increase the diameter of the engine and, consequently the amount of air accelerated, instead of to increase jet speed in smaller nozzles to the same thrust requirement.

2.4.2.7 Goldstein Analogy

The presented GAA, developed by Marvin Goldstein in the 1970s (Goldstein, 1976), is a powerful mathematical framework used in aeroacoustics to analyze the sound generated by fluid flows. It is a refinement of the pioneering work by Lighthill (1952, 1954, 1956), who first proposed an acoustic analogy that treated all fluid motion as a sound source radiating into a quiescent medium – as mentioned in previous section. Goldstein's key contribution was to generalize this concept by properly accounting for the influence of a non-uniform mean flow – the steady-state motion of the fluid itself – on the propagation of sound. This crucial advancement makes the analogy far more applicable to real-world problems like jet engine noise, fan noise, and boundary layer noise, where the fluid's motion is complex and has a direct impact on how sound waves travel and are refracted. By isolating the effects of sound generation from sound propagation, Goldstein's analogy simplifies the analysis of complex flow fields and allows engineers to model and predict noise sources more accurately.

The Goldstein's analogy aims to provide a more solid and unified theoretical foundation for various methods used to study jet noise (Goldstein, 2003; Goldstein and Leib, 2008). It achieves this by taking the full, complex Navier-Stokes equations and mathematically rewriting them to resemble the much simpler linearized Navier-Stokes (LNS) equations. In this process, the paper cleverly absorbs the complex viscous and thermal non-linearities of the original equations into new, generalized terms, which it calls a generalized Reynolds stress and a generalized stagnation enthalpy flux. These terms will be briefly summarized in the next pages.

A key innovation is that this linearization is not done around a simple, uniform flow. Instead, it uses a highly adaptable "base flow" that can be specified to represent a wide range of fluid flow conditions. By carefully choosing the properties of this base flow, Goldstein (2003) demonstrates that many existing, seemingly different approaches to the jet noise problem can all be understood as specific applications of this single, generalized framework. This approach not only validates earlier work but also suggests new ways to tackle the problem. Although the derivation of GAA begins with a complete formulation of Navier-Stokes and thermal energy equation, Goldstein (1976) uses subsequent Reynolds and Favre averaging operators, as described in Eq. 2.41 and 2.42.

$$\overline{\phi} = \lim_{T\to\infty} \frac{1}{2T} \int_{-T}^{T} \phi(x,t) W(t) dt \,, \tag{2.41}$$

where, $\overline{\phi}$ is an ordinary transport variable (ϕ) averaged in time, and $W(t)$ is a weighting function such that equals 1. Depending on the case, Randall (2003) suggest that it can be a symmetrical gaussian "bell-shaped" function. Goldstein (2003) uses the first case ($W(t) = 1$) to deduce his GAA.

$$\tilde{\phi} \equiv \frac{\overline{\rho\phi}}{\overline{\rho}} \,, \tag{2.42}$$

where, $\tilde{\phi}$ is a Favre-averaged transport variable. It is weighted by the density ρ of the fluid.

The time-averaging process turns all deduction well-matched with RANS equations with its time-averaged variables. However, the flow need not be determined, of course, from a RANS simulation. It can, for example, be determined by applying the Equations 2.41 and 2.42 to a LES or a DNS computation. This extends the method for all flow field resolved numerically, independent of the approach.

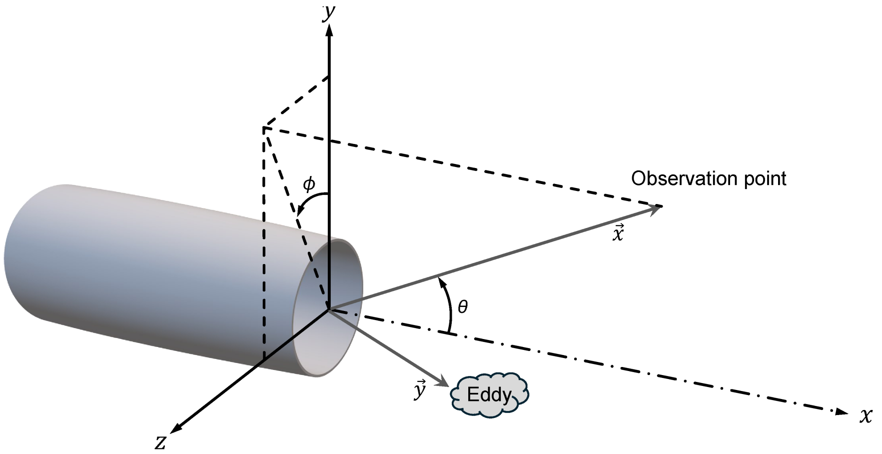

Figure 2.16: Coordinate system adopted in GAA.

Ultimately, Goldstein (2003) focuses on deriving these accurate theoretical results, treating the remaining non-linear complexity as a more manageable modeling problem. As determined by Goldstein (2003); Goldstein and Leib (2008); Leib and Goldstein (2011), the acoustic spectrum at an observation point in **x** (vector $\vec{r}$) due to unit volume of turbulence at source point **y**, as detailed in the coordinate system in Fig. 2.16, is given by:

$$I_\omega(\mathbf{x}|\mathbf{y}) = (2\pi)^2 \Gamma_{ij}(\mathbf{x}|\mathbf{y};\omega) \int \Gamma^*_{kl}(\mathbf{x}|\mathbf{y}+\eta;\omega) \mathcal{H}_{ijkl}(\mathbf{y},\eta,\omega) d\eta \,, \tag{2.43}$$

where, the integration is over the source correlation volume. The superscript star $(*)$ indicates the complex conjugate. Latin indices i, j, k, l can range $[1{,}2{,}3]$, and Greek incides λ, κ can range $[1{,}2{,}3{,}4]$. $\Gamma_{\lambda j}(\mathbf{xly};\omega)$ is a "propagator" function defined, for a locally parallel mean flow, by

$$\begin{aligned} \Gamma_j(\mathbf{x}|\mathbf{y};\omega) = \int_{-\infty}^{\infty} \Bigg[& \frac{\partial}{\partial y_j} e^{ik(x_1-y_1)} \hat{g}^a_{\lambda 4}(\mathbf{y}_T|\mathbf{x}_T;k{,}\omega) \\ & - (\gamma-1)\delta_{\lambda 1} e^{ik(x_1-y_1)} \frac{\partial U(\mathbf{y}_T)}{\partial y_j} \hat{g}^a_{44}(\mathbf{y}_T|\mathbf{x}_T;k{,}\omega) \Bigg] dk \,, \end{aligned} \tag{2.44}$$

where, $\hat{g}^a_{\lambda 4}(\mathbf{y}_T|\mathbf{x}_T;k{,}\omega)$, or simply $\hat{g}^a_{\lambda 4}$ in subsequent steps, is the adjoint vector Green's function. Its Fourier transform is given by:

$$\hat{g}^a_{\lambda 4}(\mathbf{y}_T|\mathbf{x}_T;k{,}\omega) = \frac{1}{(2\pi)^2} \iint e^{-i[k(x_1-y_1)-\omega(t-\tau)]} g^a_{A4}(\mathbf{y}{,}\tau|\mathbf{x}{,}t)\, d(t-\tau)\, d(x_1-y_1) \,, \tag{2.45}$$

where, it is given by Equations 4.8 to 4.11 disposed in Goldstein and Leib (2008). $U(\mathbf{y}_T)$ is the mean flow velocity component in the transverse direction ($\mathbf{y}_T$), γ is the specific heat ratio.

For a locally parallel mean flow, the components of the adjoint vector Green's function can be expressed in terms of a single (scalar), self-adjoint, Green's function, as expanded by Goldstein (2003). Remembering that $\hat{g}^a_{\lambda 4}$ and $\hat{G}_0$ are function of the respective variables $(\mathbf{y}_T|\mathbf{x}_T;k{,}\omega)$, and for simplification, thus:

$$\left.\begin{aligned} \hat{g}_{i4}^{a,0} &= \frac{\tilde{c}^2}{(\omega - Uk)^2}\frac{\partial \hat{G}_0}{\partial y_i}, \quad i = 2,3, \\ \hat{g}_{14}^{a,0} &= -\tilde{c}^2 k(\omega - Uk)\hat{G}^a = \frac{-ik\tilde{c}^2}{(\omega - Uk)^2}\hat{G}_0, \\ \hat{g}_{44}^{a,0} &= -(\omega - Uk)^2\hat{G}^a = \frac{-1}{\omega - Uk}\hat{G}_0, \end{aligned}\right\} . \tag{2.46}$$

Under some assumptions, Leib and Bridges (2022) demonstrated that it can be calculated using Eq. 3.7 in terms of coordinate systems θ and ϕ.

$$\frac{\partial}{\partial r}\frac{c^2}{(1 - M\cos\theta)^2}\frac{\partial \hat{g}_0}{\partial r} + \frac{\partial}{r\partial\phi}\frac{c^2}{(1 - M\cos\theta)^2}\frac{\partial \hat{g}_0}{r\partial\phi} + \omega^2\left(1 - \frac{\frac{c^2}{c_\infty^2}\cos^2\theta}{(1 - M\cos\theta)^2}\right)\hat{g}_0 = 0\,, \tag{2.47}$$

where, subject to the boundary conditions presented in Leib and Bridges (2022), the equation above is solved using the finite-volume method (FVM). Around each mesh vertex, a two-dimensional control volume (CV) is created – which is briefly described in the next section.

$$\begin{aligned} I_\omega(\mathbf{x}|\mathbf{y}) = \frac{(2\pi)^2}{x^2}\frac{2\pi\omega\sin\theta}{c_\infty(1 - M_\infty^2\sin^2\theta)^{3/2}}\Bigg\{ & \left[(C^4\Phi_{1111}^* + 2C^2(1 - C^2)\Phi_{1122}^* + (1 - C^2)^2\Phi_{2222}^*)\hat{g}_0\right]^2 \\ + 4\left|\frac{\sqrt{\tilde{c}^2}\cos\theta^s}{c_\infty(1 - M\cos\theta^s)}\nabla_T\left(\frac{\sqrt{\tilde{c}^2}\hat{g}_0}{\omega(1 - M\cos\theta^s)} - \frac{(\gamma - 1)c_\infty}{2(1 - M\cos\theta^s)}(\nabla_T M)\hat{g}_0\right)\right|^2 & \Phi_{1212}^* \\ + \; 2\big(|G_{23}|^2 - \operatorname{Re}\Gamma_{22}^*\Gamma_{33}^*\big)(\Phi_{2222}^* - \Phi_{2323}^*)\Bigg\}, & \end{aligned} \tag{2.48}$$

where, the Doppler-weighted cosine function C, which weighs the local sound speed ($\tilde{c}$), the far-field sound speed (c_∞), the local Mach number (M), and the angle of observation (θ), given by: is defined by:

$$C^2 = \frac{\tilde{c}^2\cos^2\theta^s}{c_\infty^2(1 - M\cos\theta^s)^2}\,, \tag{2.49}$$

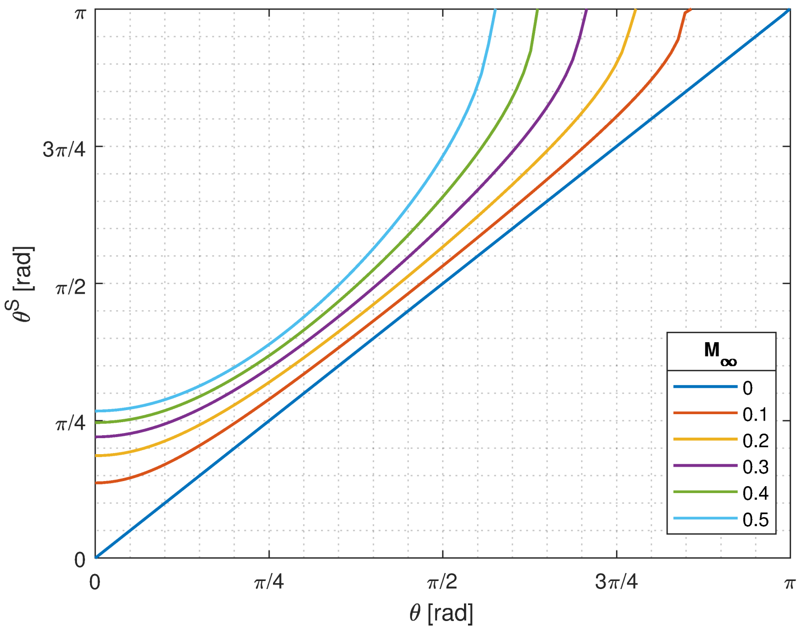

Figure 2.17: Radiation angle (θ^S) and observer angle (θ) at different free stream Mach numbers (M_∞).

where, θ^s is the radiation angle and, as it is function of the free stream Mach number, its relation is defined as

$$\frac{k_1^*}{\kappa_0} = cos\theta^s = \frac{1}{1 - M_\infty}\left(-M_\infty + \frac{cos\theta}{\sqrt{1 - M_\infty^2 sin^2\theta}}\right), \tag{2.50}$$

This graph illustrated in Figure 2.17 is a key result of the concept in linearized compressible flow theory (LNS), specifically demonstrating the effect of Mach number on noise deflection. The horizontal axis, θ, represents the physical position of the observer relative to the downstream jet axis, while the vertical axis, θ^s, represents the radiation angle.

The curve family shows how, for a given observer angle θ, the radiation angle θ^s shrinks significantly its limits as the free-stream Mach number (M_∞) increases. The straight line where $M_\infty = 0$ represents the absence of co-flow or a quiescent atmosphere flow case, where the physical angle equals the effective angle ($\theta = \theta^s$). As will be discussed in the next chapter (see Chap. 3) the studies conducted in this thesis are related with the condition of no free-stream velocity.

For any finite Mach number, i.e. the presence of a free-stream velocity, the curves bend upward and downward, indicating that the noise propagation is sensitive to a change in the incident free-stream velocity. This magnification of the flow's response is a fundamental consequence of compressibility effects and its contribution in the refraction of the noise path. Several studies are concerned around this phenomenon, such the experimental studies as Almeida (2009); Almeida et al. (2014); Lawrence (2014), and the numerical findings as Leib and Bridges (2023).

2.5 Patents of Noise-Control Devices in JMN

The rise of the jet engine in the mid-20th century inevitably brought with it the challenge of jet noise, which rapidly became a central concern for both industry and regulators. Since the 1950s, significant efforts have been directed at mitigating the acoustic footprint of jet-powered aircraft. What initially began as exploratory research into the turbulent mixing processes that generate noise has since evolved into a mature and highly diversified field of aeroacoustic engineering. Over the decades, numerous technologies, research initiatives, and industrial projects have sought to develop practical noise reduction strategies, many of which have been incorporated into the commercial aircraft in operation today.

A review of patent repositories reveals a vast and steadily growing portfolio of devices, techniques, and methods dedicated to jet noise reduction. Patents in this field reflect the translation of fundamental research in Aeroacoustics into applied engineering solutions, often representing intermediate steps between theoretical advances and large-scale industrial adoption. The range of solutions is notable, encompassing nozzle geometries, active and passive flow-control devices, acoustic liners, and hybrid systems that combine multiple strategies. The Table A.1 summarizes the evolution and the main creative results for noise reduction in jet engines, in parallel to meet regulatory noise requirements while preserving or improving engine performance.

One of the first solutions implemented in business jets is related to lobular exhausting nozzle of hot gases from engine core. The working principle is based on the forcing mixture between the bypass air flow and core jet by means of entrances disposed circularly by metal lobed sheets. Concepts introduced by Lear Avia Coorp. in 1974 (US3934675A), see Tab. A.1, are used until nowadays. This type of device is feasible and efficient for business jets or small aircrafts powered by low-bypass ratio engines. Figure 2.18 presents the sketches of the patent in (a) and an example of a similar in an Embraer Phenon 300 in (c).

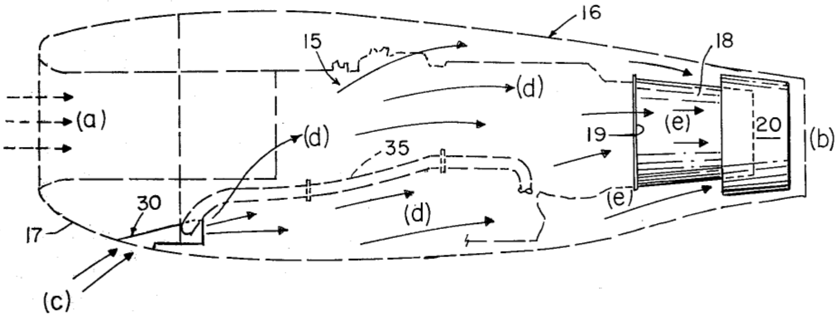

(a) US 3,934,675 A.

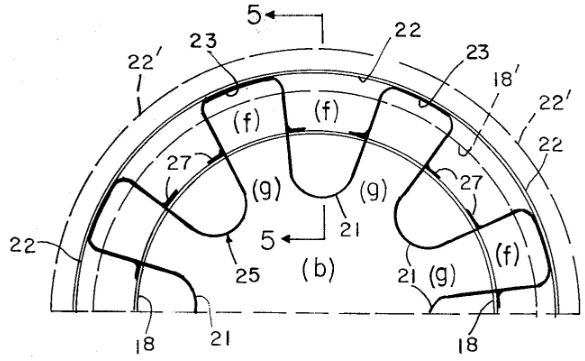

(b) Detail.

(c) Phenon 300 engine.

Figure 2.18: Metal sheets in a lobed shape disposed between bypass and core exhaust. Lear Avia Coorp. (a), detail (b), and an example in an Embraer Phenom 300 (c).

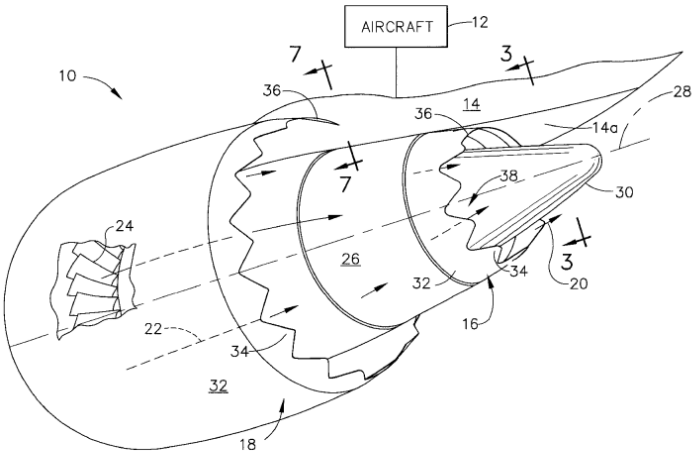

(a) *US6532729B2.*

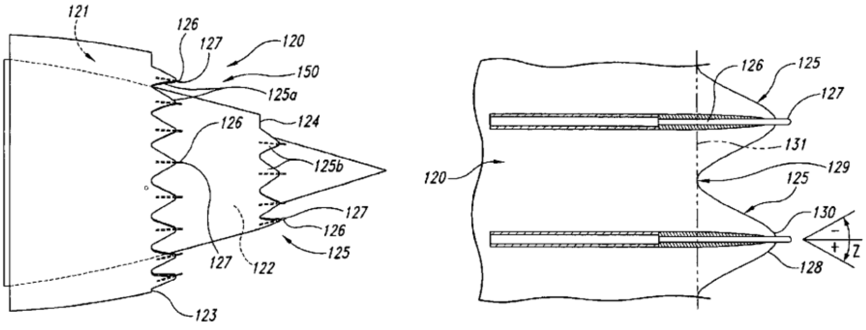

(b) *US7966826B2.*

Figure 2.19: Chevrons disposed at bypass and core exhaust. General Electric Co. in (a), and Boeing in (b).

One of the most influential patented technologies is the serrated or 'chevron' nozzle, widely adopted in modern turbofan engines. The word chevron comes from the old french that, in a direct translation, means *rafter* or *roof beam* due its triangular shape. Chevrons induce controlled streamwise vorticity into the mixing layer between the jet core and surrounding air, enhancing turbulent mixing and reducing the strength of large-scale coherent structures responsible for low-frequency noise. Early patents, such as patent *US6532729B2* (General Electric, 2001) and *US7966826B2* (Boeing, 2011), presented in Fig. 2.19, provided the foundation for the implementation of chevron nozzles on commercial aircrafts like the Boeing 787 and 747-8. These designs represented a balance between acoustic benefit and performance efficiency, becoming one of the most visible markers of jet noise reduction on contemporary airliners.

Another major class of patented technologies involves acoustic liners installed within engine nacelles. These devices, based on Helmholtz resonator principles, are designed to absorb specific frequency ranges of fan or engine-generated noise. Foundational work in this area is captured in studies from Dean (1974), whose results present a considerable noise reduction by increasing acoustic impedance by liners. More recent patents, including *US11353240B2* (NASA, 2019), focus on adaptive liners with tunable impedance surfaces capable of adjusting their acoustic response to different flight regimes. This evolution illustrates the continuous effort to refine noise-absorbing technologies in line with increasingly stringent noise regulations.

In addition to passive treatments, fluidic and active flow-control methods have generated a considerable body of patents, defined as ANRD in Table A.1. These include the use of micro-jets, synthetic jets, or fluidic oscillators to perturb the jet shear layer, thereby breaking down large-scale turbulent structures into smaller, less efficient noise radiators. For instance, *EP1493912A1* (General Electric, 2004) explores advanced fluidic actuators to dynamically control exhaust plume characteristics. Similarly, *US20180080408A1* (Safran Aircraft Engines, 2016) details a system of microjet injection at the nozzle exit for noise suppression. As presented on the experimental study of Laurendeau et al. (2006) these technologies represent innovative directions in active jet noise control and contribute to the noise reduction in jets.

Further diversification of the patent landscape can be seen in novel shape-memory material. Types of metal alloy with variable-geometry based in shaped-memory materials might slightly alter exhaust geometry. For example, *US6318070B1* (United Tech. Coorp., 2000), which consists in a series of flaps driven by shape memory alloy (SMA) actuators to vary fan exist nozzle area, while more futuristic concepts are seen in *GB2431720A* (Rolls-Royce, 2005), which describes a series of vortex generators based on shape memory properties. These patents suggest that noise mitigation strategies are increasingly to accomplish noise reduction goals, even with a slight performance degradation or increasing in energy consumption.

Patent activity in jet noise reduction is therefore more than a catalog of technical devices; it represents an evolving map of industry priorities, regulatory drivers, and technological opportunities. Historically, surges in patenting activity have closely followed revisions of International Civil Aviation Organization (ICAO) (2016) noise certification standards, as companies sought to secure intellectual property around emerging solutions.

In recent years, advances in CAA, machine learning optimization, and acoustic metamaterials have expanded the scope of patented concepts. For instance, *US12162618B2* (Boom Technology Inc., 2022) introduces a shaped aircraft nozzles with tandem mixing devices for their promising low-level noise supersonic jets (XB-1[4] and Overture[5]). As regarded by International Civil Aviation Organization (ICAO) (2022), the renascent supersonic projects are the new spotlight in noise issues, once the next generation of supersonic civil aircrafts must to avoid or mitigate sonic boom over populated areas. Figure 2.20 depicts the XB-1, which is in test cam-

---

[4] https://boomsupersonic.com/xb-1

[5] https://boomsupersonic.com/overture

(a) XB-1.

(b) *JP2022129373A*.

Figure 2.20: Novel projects and solutions for sonic boom mitigation. XB-1 by Boom Technology Inc. in (a), and JAXA in (b).

paign at the moment, and a sketch of a Japanese patent (see *JP2022129373A* in Tab. A.1), which aply methods for reducing engine and sonic boom noise.

In summary, patents serve as a valuable lens through which to view the technological evolution of jet noise mitigation. From early nozzle geometries (as evaluated in this thesis) to sophisticated adaptive liners and fluidic injection systems, patented innovations demonstrate how the field has responded dynamically to regulatory, industrial, and societal pressures. As the aviation sector moves toward new paradigms of propulsion and sustainability, the patent record suggests that noise reduction will remain a fertile ground for innovation, balancing environmental imperatives with the enduring demands of performance and efficiency.

3 Methodology

> Give me a lever long enough and a fulcrum on which to place it, and I shall move the world.
>
> *Archimedes of Syracuse*
> 287 – 212 B.C.

Several approaches make the research around the jet mixing nozzles (JMN) as part of an entire understanding of the physics involved in this problem. Hence the Computational Fluid Dynamical (CFD) techniques required to simulate the flow differ as well, and they must to represent the experimental campaign. This chapter is dedicated to present the provided benchmark cases on JMN with different PNRD geometries. Thus, the JMN fundamentals, some experimental tests and the numerical methods available to solve them, with their respective numerical results of the state of the art, are presented in the following. Nevertheless, is presented a description of the methods used for carrying the numerical simulations and its assumption to ensure a accurate and feasible execution. This chapter is divided into three sections. The first part furnishes the main details about the facilities where the experiments were performed and key information about the experimental hardware used for produce JMN acoustic signatures.

The second section presents the entire CFD modeling, being: physical, mathematical and numerical; adopted to deal with the problem of JMN in axisymmetric and non-axisymmetric nozzles. And a domain reduction strategy for PNRD geometries is conferred for RANS simulations.

The third section deals with the CAA modeling. Some assumptions and simplifications are presented in the GAA methodology used in FastJetNoise code. The CAA mesh is presented and its assumptions for PSD prediction in far-field.

3.1 Experiments and Benchmarking

Experiments have been conducted in the ISVR's Doak Laboratory, using the Flight Jet Rig (FJR), with three main nozzle models: a round baseline nozzle, a squared corrugated nozzle, and an internally-notched nozzle. The Doak Laboratory comprises a chamber, fully anechoic above 400 Hz, with dimensions approximately equal to 15 m-long, 7 m-wide and 5 m-high. Two separate air supply systems allow in-flight simulations of single stream jet flows using the FJR. The primary 'core' jet flow is supplied by a high pressure compressor-reservoir system, capable of producing a maximum inlet pressure of 20 Bar. The experimental campaign was conducted in ISVR during the season from July 2020 to June 2021, and the results used herein deals only with isolated, static, and cold jets.

An image of the anechoic chamber depicting the FJR and the far-field microphone array, from which the data presented in this thesis were recorded, is shown in Figure 3.1. Total temperature and pressure sensors are mounted both in the plenum (located far upstream of the nozzle exit) and along the pipework of the core and flight jet ducts. Ambient chamber properties, such as pressure, temperature and relative humidity, are also recorded. These readings are required to set the nominal jet exit velocity condition and to apply corrections to the data (e.g. atmospheric attenuation and NPR variation during the long hot-wire traverse measurements). Far-field data are obtained using a linear "flyover" array. Ten microphones are used to cover polar observer angles ranging from $40°$ to $130°$, at $10°$ intervals. The closest microphone, $\theta = 90°$, is located at approximately 55 jet nozzle diameters from the nozzle centerline.

An example of squared corrugated nozzle used in the experiments is shown in 3.2. Some probes are detailed in picture downstream to the tested geometry. The R40 geometry, represented in the 3D CAD in Figure 3.3, serves as the initial experimental benchmark to validate the FastJetNoise code, and sometimes it is referred as a 'baseline' geometry.

The SC geometry nozzles (Fig. 3.4) is a simple alternative PNRD; constructed with 16 pairs of alternate-slanted lips in its exit portion. The slant angle of the lips is represented by α and corresponds to the four different values ($3°$, $6°$, $9°$, and $12°$), i.e. the nomenclature of SC03 geometry refers to the squared corrugated nozzle with $\alpha = 3°$. This angle is relative to the baseline R40 nozzle lip with alternated inward and outward corrugation. Theoretically, by increasing turbulence downstream from the nozzle, this type of PNRD is expected to present a considerable reduction in the far-field PSD.

The IN geometry (Fig. 3.5) presents a total of 8 well-distributed notches around the nozzle trailing edge. A defined notch geometry is presented with its dimensions. Similar geometries were tested in several studies with promising experimental evidence in noise reduction (Oishi, 2010; Ishii et al., 2019).

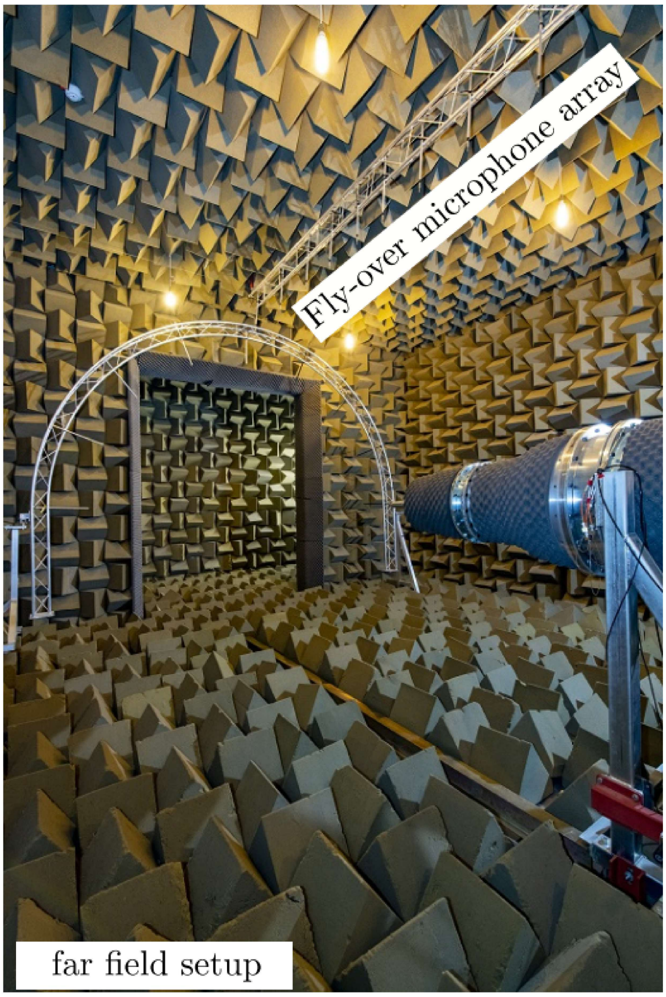

Figure 3.1: FJR in Doak Laboratory, at the University of Southampton. Adapted from (Proenca and Lawrence, 2022).

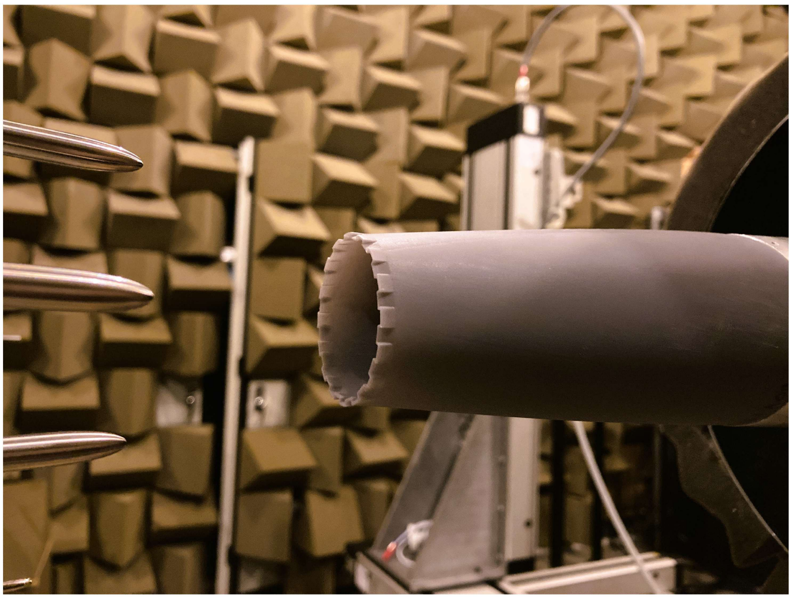

Figure 3.2: Detail of a SC nozzle geometry tested in Doak Lab.

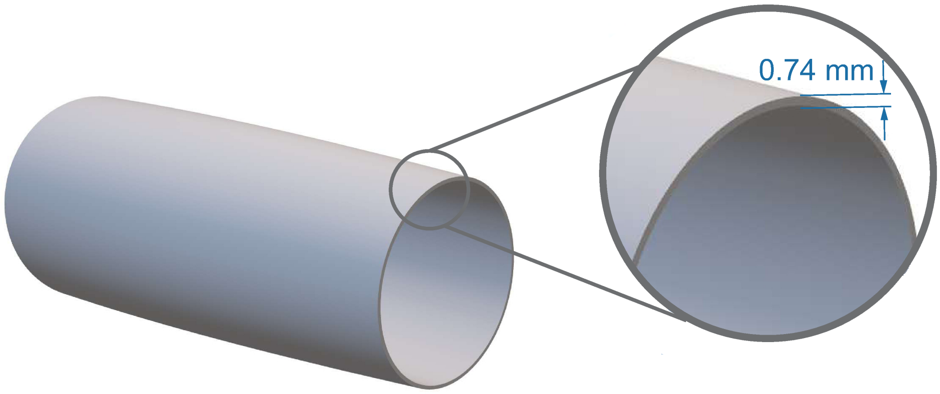

Figure 3.3: Round nozzle geometry (R40) and detail.

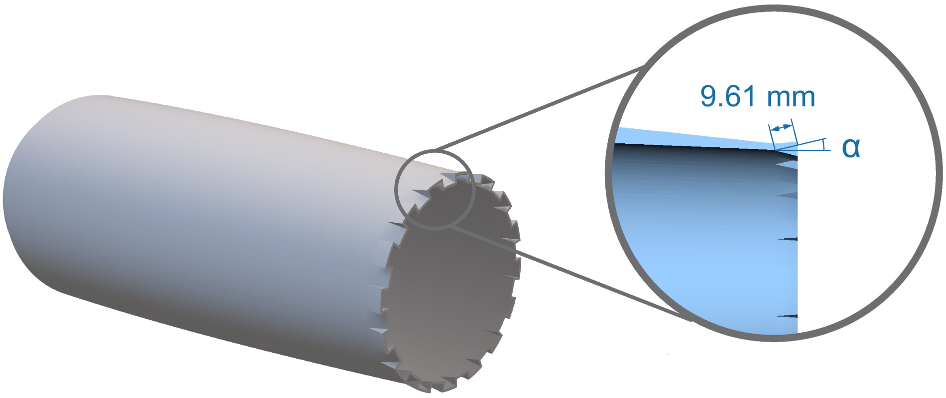

Figure 3.4: Squared corrugated geometry (SC) and detail.

3.1.1 Experimental Data and Inferences

As briefly discussed previously, the benchmark results obtained from the Southampton Doak Laboratory require careful analysis and interpretation prior to the numerical investigations. This section presents the main observation derived from these experimental datasets, emphasizing the observed effects of each PNRD configuration and their respective implications for jet noise reduction.

When analyzing experimental data, the provided Power Spectral Density (PSD) distributions serve as a robust foundation for comparative evaluation among the investigated geometries. Graphical comparisons, such as those shown in Figure 3.6, offer a clear and intuitive means of elucidating the relationship between the nozzle configuration and the resulting acoustic response. In this context, each pair of plots contrasts the baseline smooth circular nozzle

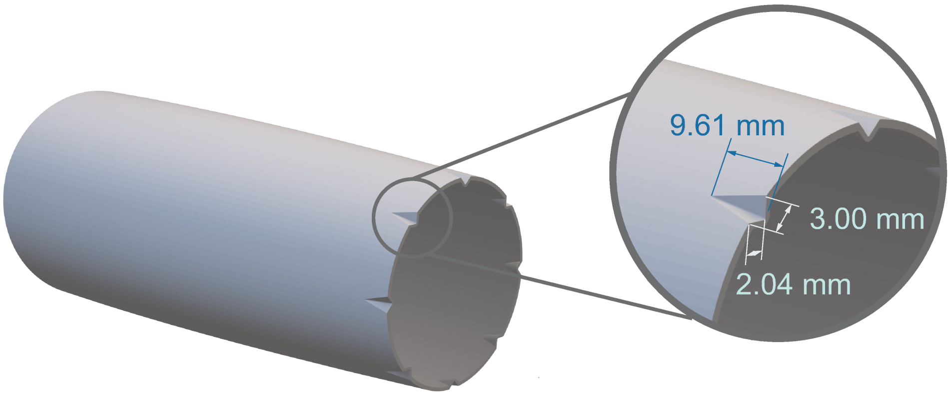

Figure 3.5: Internal notched geometry (IN) and detail.

(R40, in blue) with modified geometries – the squared corrugated (SC), at left, and the internal notched (IN) nozzle, at right – at three observer angles (43°, 61°, and 90°).

A consistent pattern is observed across all configurations: the introduction of corrugations influences the spectral distribution, particularly in the moderate to high Strouhal numbers. At $\theta = 43^\circ$ both SC geometries exhibit a considerable reduction ($\approx 2\,\mathrm{dB}$) in PSD amplitude relative to baseline, indicating a partial attenuation of the dominant jet noise components. This effect is more pronounced for the SC12 nozzle, suggesting that external corrugations enhance mixing and weaken large-scale coherent structures responsible for low-frequency noise. On the other hand, a trigger on mixing processes boosts the high frequency components (green line on Fig. 3.6 (a), (c), and (e)).

At the intermediate angle of 61°, which corresponds to the region of maximum acoustic radiation, the PSD reduction becomes more evident for both modified geometries. The IN nozzle maintains a similar spectral shape of $\theta = 43^\circ$ but with slightly higher energy content, especially at higher Strouhal numbers. This behavior implies that internal notches may alter the flow development differently, potentially shifting the turbulence structures and modifying their acoustic response.

Finally, at the sideline angle of 90°, the differences between configurations are more evident. The PSD levels diverge across SC geometries in the high frequency band, suggesting that lateral radiation is directly affected by nozzle modification, as seen in Fig.3.6 (e), where the SC spectra overtake the baseline R40 at $St > 3$. In contrast, the IN spectrum presents a controlled decay near the baseline. This pattern is also observed in other experimental studies of notched nozzles (Oishi, 2010; Ishii et al., 2019).

Overall, the experimental data reinforce the premise that geometric modification of the nozzle exit can significantly affect the acoustic field. Although both the SC and IN nozzles exhibit some degree of attenuation, the IN configuration provides a more uniform reduction across the spectrum, particularly at the most critical radiation angles. These observations suggest that the more intrusive PNRD, such as SC12, does not necessarily imply a significant noise reduction, especially in the high frequency band. It is observed in Figs. 3.6 (a) and (c) where SC06 (more intrusive) is louder than SC03 at low Strouhal numbers ($St < 0.4$) – the yellow line surpasses the red one.

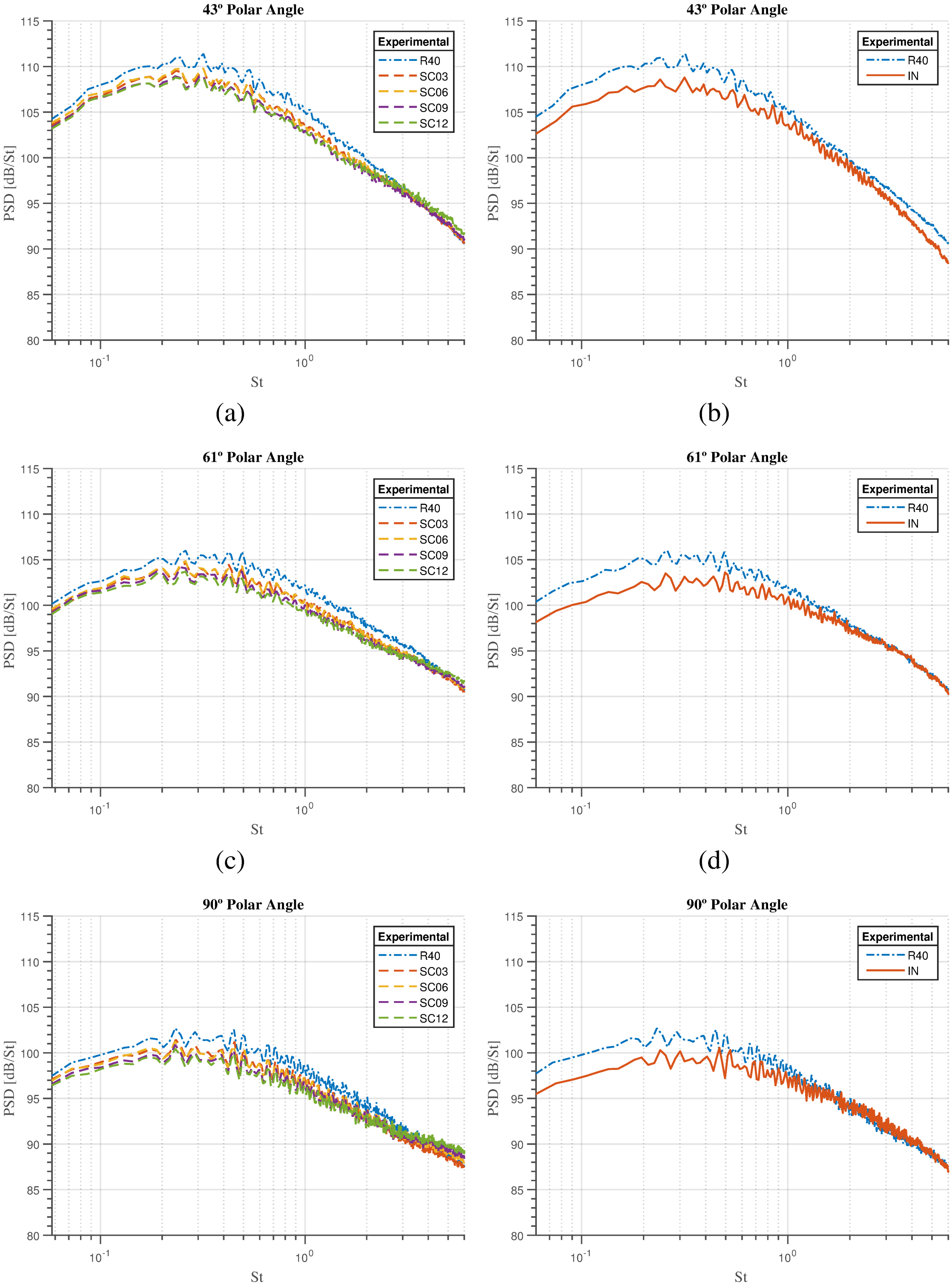

(a) (b)

(c) (d)

(e) (f)

Figure 3.6: Experimental PSD comparison between R40 and squared corrugated (SCs) nozzles (left) and R40 and IN nozzle (right) at $M_a = 0.8$.

3.2 CFD Modeling

The following sections provide a detailed overview of the physical, mathematical, and computational models used to simulate the jet flow in its fluid dynamic perspective. The primary objective is to represent the complex JMN dynamics using basic RANS simulations and commonly used turbulence closure models. This modeling approach is crucial for understanding the performance of passive noise reduction devices (PNRDs) and for validating the numerical methods against experimental data. Once the CFD results are used to feed the CAA code (FastJetNoise), more details are given in the following subsections.

3.2.1 Physical Modeling

The results used for validation in this work were carried out in a circular, smooth and transonic jet ($Ma \approx 0.8$) of the FJR. In this set, the inner surface of the nozzle presents a smooth roughness and the jet is tested in a static condition; i.e., the in-flight scenario is not considered. These PNRD geometries are modifications of the nozzle trailing edge, as described previously, focusing the noise reduction and alternative for noise reduction.

Table 3.1: Experimental parameters used in CFD and CAA setup.

	Round Nozzle$^{(1)}$	**Square Corrugated Nozzle**$^{(1)}$				**Internal Notched**$^{(1)}$
Description	R40	SC03	SC06	SC09	SC12	IN
D_j [mm]	40					
p_∞ [Pa]	101,533	100,390	100,380	100,340	100,330	100,090
T_∞ [K]	286.26	294.54	295.04	294.89	295.12	289.16
PR [-]	1.5994	1.6118	1.6234	1.6230	1.6200	1.5606
T_{0_j} [K]	291.09	293.82	294.41	294.18	294.66	294.99
U_j [m/s]	274.44	274.38	276.56	276.39	276.12	269.72
M_j [-]	0.8473	0.8548	0.8616	0.8614	0.8596	0.8234
M_a [-]	0.80	0.80	0.80	0.80	0.80	0.78
M_∞ [m/s]	0					

$^{(1)}$ Experimental data provided by Southampton University (UK).

In the current investigation, six different geometries in total were numerically evaluated and simulated. As presented in Table 3.1 these basic nozzles consist of a round smooth nozzle (R40), three squared corrugated nozzle (SC03, SC06, SC09, SC12), and an internal notched one (IN). All geometries have a diameter of $40\,mm$ and the static condition was numerically represented.

3.2.2 Mathematical Modeling

Dealing with a high Reynolds number and compressible flow problem ($Ma_j \approx 0.8$), a commercial CFD solver might be able to resolve the mass-balance equation, Eq. 3.1, *momentum*, Eq. 3.2, and thermal energy equation in their compressible and time-averaged formulation (ANSYS, 2021a).

$$\frac{\partial \overline{\rho}}{\partial t} + \frac{\partial}{\partial x_i}\left(\rho \overline{u_i}\right) = S_m \, , \tag{3.1}$$

where x_i are the spatial coordinates, $\overline{u_i}$ are the time-averaged velocity components, ρ is the fluid density, and S_m is the term of mass source, which is negligible for these studies.

$$\frac{\partial (\rho \overline{u_i})}{\partial t} + \frac{\partial}{\partial x_j}\left(\rho \overline{u_i}\,\overline{u_j}\right) = -\frac{\partial \overline{p}}{\partial x_i} + \frac{\partial}{\partial x_j}\left[\mu \left(\frac{\partial \overline{u_i}}{\partial x_j} + \frac{\partial \overline{u_j}}{\partial x_i}\right)\right] - \frac{\partial}{\partial x_j}\left(\rho \overline{u_i' u_j'}\right) + \rho f_i \, , \tag{3.2}$$

where u_i' are the velocity fluctuations, $\overline{p}$ is the averaged pressure, μ is the fluid viscosity.

3.2.2.1 Turbulence Closure Model

Once all methodology and simulations presented in this thesis are related to filtered Navier-Stokes equations, i.e. RANS modeling, a closure model which can model the turbulent viscosity and turbulent effects is needed. As presented on the previous section, the filtering process of mass-balance and momentum equations creates new needs for modeling and closing the resultant system of equations.

As a requirement of the Goldstein and Leib acoustic analogy, the CFD simulation must feature a specific turbulence closure model. As described in Goldstein (2003); Goldstein and Leib (2008); Leib and Goldstein (2011) the main turbulence entries for their AAC method are: turbulent kinetic energy and turbulent dissipation ratio; provided by k-ϵ model.

The k-ϵ is a two-equation turbulence model obtained by mean of averaged Navier-Stokes equations. It allows the determination of both, a turbulent length and time scales by solving two separate transport equations. The well-known k-ϵ model used in the present study is included in this class of models and has become the workhorse of several practical engineering flow calculations. It was proposed by Launder and Spalding (1972) and its evolutions feature an robust, economic and feasible accuracy for a wide range of turbulent flows, becoming an important alternative for industry in fluid flow and thermal simulations. It is a semi-empirical model, and the derivation of the model equations relies on phenomenological considerations and empiricism.

The following GAA modeling requires some specific turbulence properties, such as turbulent kinetic energy (TKE) and turbulence dissipation ratio (ε). Based on this, for the turbulence closure model, the solver might feature the standard k-ε model, Eq. 3.3 for k, and Eq. 3.4, with enhanced wall treatment, which blends the two-layer and wall function depending on y^+, due to the presence of inner and outer walls of the nozzle.

$$\frac{\partial}{\partial t}(\rho k) + \frac{\partial}{\partial x_i}(\rho k u_i) = \frac{\partial}{\partial x_j}\left[\left(\mu + \frac{\mu_t}{\sigma_k}\right)\frac{\partial k}{\partial x_j}\right] + G_k + G_b - \rho\varepsilon - Y_M + S_k\,, \tag{3.3}$$

$$\frac{\partial}{\partial t}(\rho \varepsilon) + \frac{\partial}{\partial x_i}(\rho \varepsilon u_i) = \frac{\partial}{\partial x_j}\left[\left(\mu + \frac{\mu_t}{\sigma_\varepsilon}\right)\frac{\partial \varepsilon}{\partial x_j}\right] + C_{1\varepsilon}\frac{\varepsilon}{k}\left(G_k + C_{3\varepsilon}G_b\right) - C_{2\varepsilon}\rho\frac{\varepsilon^2}{k} + S_\varepsilon\,, \tag{3.4}$$

where σ_k and σ_ε are the turbulent Prandtl number for k and ε, respectively; G_k is the production term of k due to the mean velocity gradients, G_b is the production term due to buoyancy effects (negligible), Y_M is the contribution of the compressible effects to turbulence. $C_{1\varepsilon}$, $C_{2\varepsilon}$, and $C_{3\varepsilon}$ are the default constants settled in model. S_k and S_ε are source terms defined by user (negligible).

Once the present work deals with steady state flows (RANS simulations) the temporal derivatives ($\partial/\partial t$) in Equations 3.1-3.4 are ruled out.

3.2.3 Domain Reduction Strategy

To ensure a low computational cost in the analysis carried out in this work, several assumptions were made, aiming to simplify the problem and produce rapid and feasible results. The most important one was the characteristic of geometries with axial symmetry. The axial symmetry, also known as rotational symmetry, means that an object's appearance remains unchanged when rotated by any angle around a central axis. This is different from objects that have a finite order of symmetry, like a square or a regular pentagon, which only look the same after being rotated by specific, discrete angles ($90°$ for a square, $72°$ for a pentagon). Since an axially symmetric body, such as a cylinder or a cone, can be rotated by any angle and still appear the same, it is said to have an infinite order of rotational symmetry.

The Figure 3.7 presents a simple sketch to explain visually the concept of order of symmetry for different geometries. Assuming a symmetry axis orthogonal to the plane of the figure, one notices that, for the regular square, we have an order of symmetry equal to 4. Thus, for a regular pentagon, the order of symmetry is 5. Due to the symmetry pattern, we can assume, basically, that the order of symmetry is obtained by dividing the entire circumference by the minimal representative sector of the geometry. At a first glance, one can ask: what is the order of symmetry in a circular cylinder or a solid of revolution? A rapid response is: assuming that for this type of cylinders its minimal sector tends to $0°$, a full revolution tends to an infinity of sectors, which gives a order of symmetry tending towards infinity (∞). Based on this, for the present work, the entire cylindrical domain was assumed in a pseudo-2D RANS simulation in a symmetric longitudinal plane for the R40 cases. For 3D cases, domain sectors are prescribed by the order of rotational symmetry, which is the smallest part of the geometry that represents its symmetry; for example, the SC12 geometry is made of 16 pairs of lips, giving a minimal sector of $1/16$ of the circumference, resulting in a sector of $22.5°$. On the other hand, the IN nozzle is made up of well-distributed notches, 8 along the nozzle exit, resulting in a sector of $45°$. Confirming this technical concept of domain reduction and increasing resolution, several studies were conducted with sliced or mirrored domains for a diverse range of CFD problems, for instance, Fontes et al. (2019); Lima et al. (2020); Meira (2018), among others.

The Figure 3.8 presents the mesh adopted for the round R40 nozzle with the boundary conditions (BCs) depicted in (a) and an example of a sectorial mesh adopted for the SC12 and IN geometries with the highlighted face of symmetry in (b). One notices a more refined region near the wall, downstream from the nozzle exit, and up to 20 diameters far from the nozzle. This is due to its being the most important region for CFD solution and data acquisition for the CAA inputs.

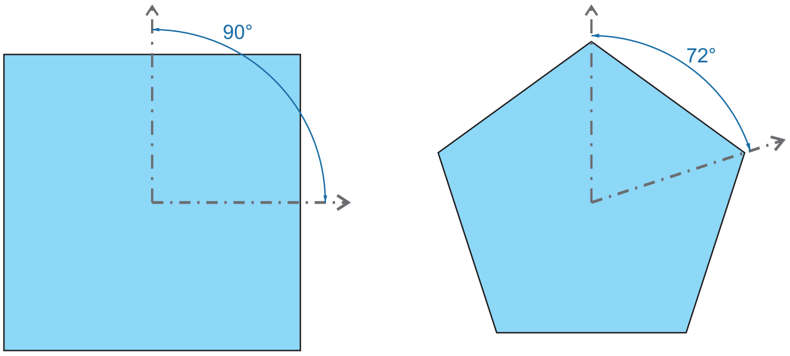

(a) Square.

(b) Pentagon.

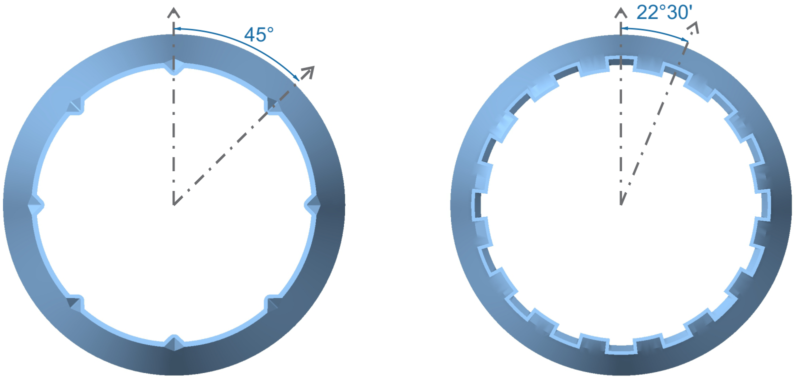

(c) IN.

(d) SC12.

Figure 3.7: Examples of order of symmetry.

3.2.4 CFD Solver Setup

To create a proper setup for CFD simulations in the Ansys Fluent, several steps were taken to ensure a correct configuration of the cases and the guarantee of stability, as recommended by ANSYS (2021a).

The numerical simulations were conducted using the pressure-based coupled solver available in ANSYS Fluent. This solver is particularly suitable for compressible flow calculations and ensures tight coupling between pressure and velocity fields, improving convergence stability in high-speed jet flows. The absolute velocity formulation was adopted, and all simulations were performed in steady-state mode. Air was modeled as an ideal gas, enabling the density to vary with temperature and pressure, which is essential for capturing compressibility effects in the jet plume. Constant specific heats, viscosity, and thermal conductivity were assumed for the gas properties, as provided in the Fluent materials database (ANSYS, 2021a,b).

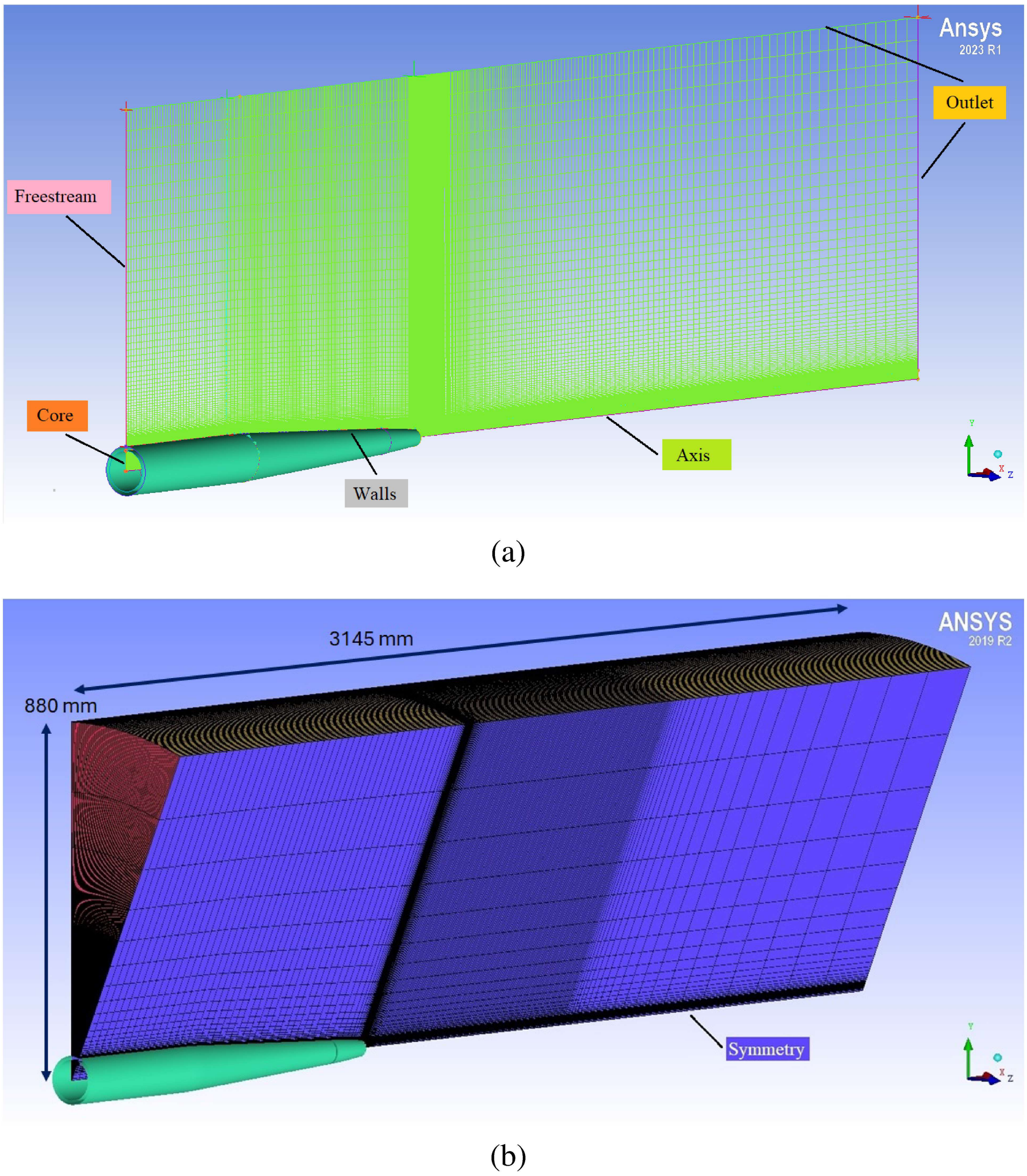

Figure 3.8: Axisymmetric mesh of the 40 mm circular nozzle with boundary conditions for R40 in (a) and an example of 3D mesh for SC12 in (b).

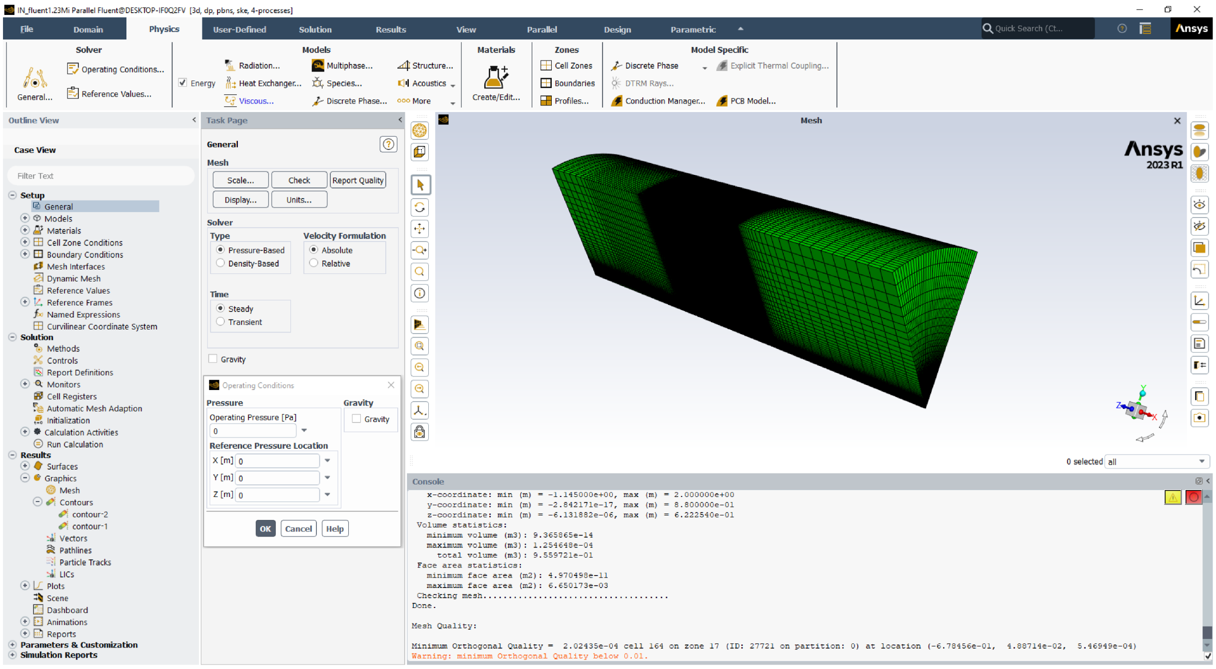

```
   x-coordinate: min (m) = -1.145000e+00, max (m) = 2.000000e+00
   y-coordinate: min (m) = -2.842171e-17, max (m) = 8.800000e-01
   z-coordinate: min (m) = -6.131882e-06, max (m) = 6.222540e-01
 Volume statistics:
   minimum volume (m3): 9.365865e-14
   maximum volume (m3): 1.254648e-04
     total volume (m3): 9.559721e-01
 Face area statistics:
   minimum face area (m2): 4.970498e-11
   maximum face area (m2): 6.650173e-03
 Checking mesh....................................
Done.

Mesh Quality:

Minimum Orthogonal Quality =  2.02435e-04 cell 164 on zone 17 (ID: 27721 on partition: 0) at location (-6.78456e-01,  4.88714e-02,  5.46949e-04)
Warning: minimum Orthogonal Quality below 0.01.
```

Figure 3.9: GUI of Ansys Fluent 2024 R2 and an example of IN case.

Figure 3.9 presents the main screen for a 3D setup case of the IN sector mesh. Notice that a warning message is displayed on the console that identifies the low orthogonal quality, achieving a minimum value of 2.02435×10^{-4}. The wedge-shaped sector did not contribute to a good orthogonal quality in the volumes near the wedge. Moreover, as a consequence of this, some strategies were taken to stabilize the solution and convergence.

Once the turbulent effects were modeled using the standard $k - \varepsilon$ model, whose formulation is ideal for free flows, as pointed by Menter (1994); Silveira Neto (2020). Due to this the wall effects of inner wall must to be accounted, and the Enhanced Wall Treatment (EWT) was employed. This approach combines the advantages of wall functions and near-wall resolution, allowing accurate prediction of both the viscous sublayer and the logarithmic region depending on the local mesh resolution. In Chapter 4 is presented brief results where the influence of y^+ in the inner wall is observed.

The computational domain was designed to replicate an axisymmetric jet issuing into a quiescent ambient medium. The boundary conditions (BCs) defined in the solver are demonstrated in different colors in Fig. 3.8, among them: *Core*, configured as pressure inlet condition with total pressure, supersonic initial pressure and total temperature according to the Table 3.1 for each case. The turbulence intensity and turbulent viscosity ratio were specified based on typical experimental conditions for fully developed turbulent jets; *Walls*, stationary walls with no heat flux (adiabatic); *Axis* as axis of symmetry; *Freestream* and *Outlet*, as pressure outlet condition with gauge pressure of 0 Pa (quiescent fluid in atmospheric pressure) and temperature of the experiment rounds in Table 3.1; *Fluid*: the air in simulation was adopted as an ideal gas,

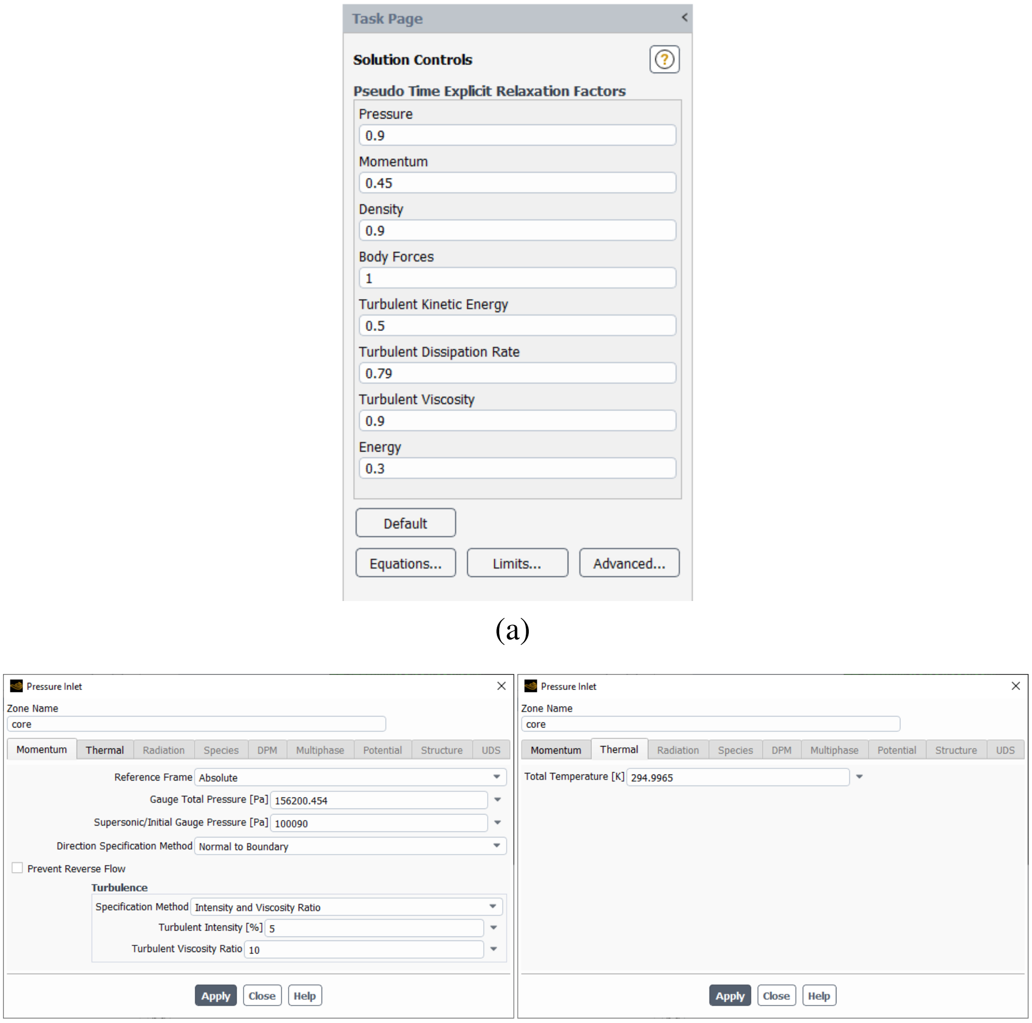

Solution Controls

Pseudo Time Explicit Relaxation Factors

Pressure: 0.9
Momentum: 0.45
Density: 0.9
Body Forces: 1
Turbulent Kinetic Energy: 0.5
Turbulent Dissipation Rate: 0.79
Turbulent Viscosity: 0.9
Energy: 0.3

(a)

Pressure Inlet

Zone Name: core

Reference Frame: Absolute
Gauge Total Pressure [Pa]: 156200.454
Supersonic/Initial Gauge Pressure [Pa]: 100090
Direction Specification Method: Normal to Boundary
☐ Prevent Reverse Flow

Turbulence

Specification Method: Intensity and Viscosity Ratio
Turbulent Intensity [%]: 5
Turbulent Viscosity Ratio: 10

Pressure Inlet

Zone Name: core

Total Temperature [K]: 294.9965

(b)

Figure 3.10: Under-relaxation parameters in (a), and the *Core* BC setup in (b).

whereas the pressure and density of the fluid coupling must be calculated; and *Symmetry*: in the faces of the radial symmetry is imposed that $\frac{\partial \phi}{\partial \vec{n}} = 0$, where ϕ is a generic variable and $\vec{n}$ is the normal direction to the volume face.

Spatial discretization was performed using second-order upwind schemes for all transport equations, including momentum, energy, and turbulence quantities. This choice provides higher accuracy in regions with strong gradients, such as the shear layers and mixing region of the jet. Pressure interpolation was handled using the second-order scheme to maintain consistency with the overall numerical accuracy.

Due to the low orthogonality of wedge volumes, the more adequate set of solution control is approximately that presented in Fig. 3.10. These parameters were carefully adjusted to ensure numerical stability and steady convergence of residuals. Convergence was assumed when all normalized residuals fell below 1×10^{-6}, and mass and momentum imbalances across the domain were within acceptable limits.

As recommended by good practices in ANSYS Fluent, forums, and tutorials, the operating conditions were modified from their default values. It means that the operating pressure was configured as $0\,Pa$, as seen in the floating window in Fig. 3.9. This ensures that the values of the working pressure is adopted in their absolute reference, i.e. the configuration of pressure in BCs, as seen in Fig. 3.10 (b), occurs directly using the values of Tab. 3.1 with no need to gauge pressure correction. All BCs dependent of pressure input were configured with the correspondent experimental value of absolute pressure.

After convergence, the flow variables were exported for further analysis, including the evaluation of velocity profiles, centerline decay, and turbulence characteristics, as available in Chapt. 4.

3.3 CAA Modeling

As briefly mentioned in Chapter 2, the mathematical model of the AAC used in this investigation is derived from the Goldstein analogy, according to Goldstein (2003); Goldstein and Leib (2008); Leib and Goldstein (2011); Leib and Bridges (2022). Resuming Equation 2.48, the acoustic spectrum per unit volume in the absence of a free-stream velocity, that is, jets under an atmospheric static conditions, reads:

$$\begin{aligned} I(x|y) = {} & \frac{4\pi^2}{x^2}\frac{2\pi\omega\sin\theta}{c_\infty}\left[C^4\Phi^*_{1111} + 2C(1-C)\Phi^*_{1122} + (1-C)^2\Phi^*_{2222}\right]\left\{\hat{g}_0\right\}^2 + \\ & \frac{16\pi^2}{x^2}\frac{2\pi\omega\sin\theta}{c_\infty}\left\{\frac{c\cos\theta}{c_\infty\omega(1-M\cos\theta)}\left[\nabla_T\left(\frac{c\hat{g}_0}{(1-M\cos\theta)}\right) - \right.\right. \\ & \left.\left.\frac{(\gamma-1)c_\infty\hat{g}_0}{2(1-M\cos\theta)}(\nabla_T M)\right]\right\}^2\Phi^*_{1212} \end{aligned} \tag{3.5}$$

where C weighs the local sound speed (c), the far-field sound speed (c_∞), the local Mach number (M), and the angle of observation (θ), given by:

$$C^2 = \frac{c^2 \cos^2\theta}{c_\infty^2 (1 - M\cos\theta)^2} \tag{3.6}$$

Equation 3.5 differs from Eq. 2.48 from Leib and Bridges (2022), in that axisymmetric turbulence is assumed ($\Phi^*_{2222} = \Phi^*_{2323}$), therefore the last term on the RHS of Eq. 2.48 is zero. For a given frequency f, C, local sound speed c, freestream sound speed c_∞, position x, observer angle θ, Mach number M and γ can be obtained based on operating conditions and physical properties. Φ^* represent the spectrum tensor components, which rely on RANS results and are calculated based on the source model described in Goldstein and Leib (2008). The source model constants were set as displayed in Table 3.2 and Table 3.3. Such values were adjusted by Goldstein and Leib (2008) considering isolated, cold, axisymmetric jets.

Table 3.2: Coefficients in truncated series for turbulence spectrum

Component	$a_{1,0}/a_{0,0}$	$a_{2,0}/a_{0,0}$	$a_{3,0}/a_{0,0}$
1111	0.073	0.070	-0.0008
2222=3333	0.519	0.049	-0.0097
1122=1133	0.103	0.079	0.0
1212	0.388	-0.126	-0.031

Table 3.3: Constants used in length scales

Component	C_0	C_1	C_T
1111	0.7	1.2	0.4
2222=3333	0.7	0.8	0.89
1122=1133	0.7	1.05	1.0
1212	1.05	1.0	1.1

The variable $\hat{g}_0$ is the adjoint Green's function, which acts as a propagator of the sources. Under some assumptions, Leib and Bridges (2022) demonstrated that it can be calculated using Eq. 3.7.

$$\frac{\partial}{\partial r}\frac{c^2}{(1 - M\cos\theta)^2}\frac{\partial \hat{g}_0}{\partial r} + \frac{\partial}{r\partial\phi}\frac{c^2}{(1 - M\cos\theta)^2}\frac{\partial \hat{g}_0}{r\partial\phi} + \omega^2\left(1 - \frac{\frac{c^2}{c_\infty^2}\cos^2\theta}{(1 - M\cos\theta)^2}\right)\hat{g}_0 = 0 \tag{3.7}$$

where, subject to the boundary conditions presented in Leib and Bridges (2022), the equation above is solved using the finite-volume method (FVM). Around each mesh vertex, a two-dimensional control volume (CV) is created – which is briefly described in the next section.

3.3.1 Numerical Modeling in CAA

The first derivatives, presented in Eq. 3.7, must then be calculated across all CV faces, following the scheme in Fig. 3.11. The Green-Gauss theorem was applied to achieve this discretization scheme – transforming the volume integrals into surface integrals and resulting in a problem of net flux in the volume faces (Souza, 2012; Meira and Souza, 2024). In the current work, the second-order centered scheme was implemented in geographic notation, (Ferziger and Peric, 2012)). The process is illustrated below for the first term on the LHS of Eq. 3.7:

$$\int_{CV} \frac{\partial}{\partial r} \frac{c^2}{(1 - M\cos\theta)^2} \frac{\partial \hat{g}_0}{\partial r} dV = \oint_S \frac{c^2}{(1 - M\cos\theta)^2} \frac{\partial \hat{g}_0}{\partial r} \vec{i}_r . d\vec{S} \tag{3.8}$$

The surface integral on the RHS of Eq. 3.8 runs over all CV faces, but since only faces s and n yield inner products which are not zero, it reduces to Riemann integrals across those faces:

$$\oint_S \frac{c^2}{(1 - M\cos\theta)^2} \frac{\partial \hat{g}_0}{\partial r} \vec{i}_r . d\vec{S} = \int_n \frac{c^2}{(1 - M\cos\theta)^2} \frac{\partial \hat{g}_0}{\partial r} r d\phi - \int_s \frac{c^2}{(1 - M\cos\theta)^2} \frac{\partial \hat{g}_0}{\partial r} r d\phi \tag{3.9}$$

The integrals on the RHS of 3.9 are evaluated numerically. For face n, for example:

$$\int_n \frac{c^2}{(1 - M\cos\theta)^2} \frac{\partial \hat{g}_0}{\partial r} r d\phi \tilde{=} \left[\frac{c^2}{(1 - M\cos\theta)^2} \frac{\partial \hat{g}_0}{\partial r} r \right]_n \Delta\phi = \frac{c_n^2}{(1 - M_n\cos\theta)^2} \left[\frac{\partial \hat{g}_0}{\partial r} \right]_n r_n \Delta\phi \tag{3.10}$$

First derivatives must then be calculated across all CV faces. In the current work, two alternatives were tested: second-order centered scheme (geographic notation, Ferziger and Peric (2012)):

$$\left[\frac{\partial \hat{g}_0}{\partial r} \right]_n \approx \frac{\hat{g}_{0N} - \hat{g}_{0P}}{\Delta r} \tag{3.11}$$

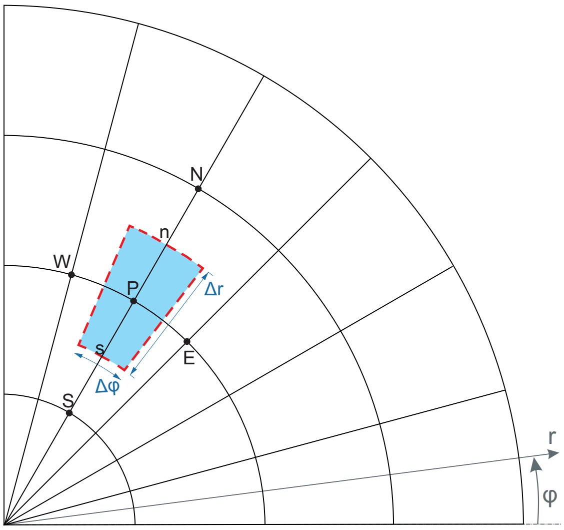

Figure 3.11: Schematic of the two-dimensional CVs in polar coordinates in geographic notation.

In addiction to further analysis, this work presents a high-order discretization scheme for the GF computation. In this innovative comparison against 2nd order well-established methods and codes, the fourth-order centered schemes (Ferziger and Peric (2012); Versteeg and Malalasekera (2007)) is given by:

$$\left[\frac{\partial \hat{g}_0}{\partial r}\right]_n \approx \frac{1}{\Delta r}\left(-\frac{1}{24}\hat{g}_{0_{NN}} + \frac{9}{8}\hat{g}_{0_N} - \frac{9}{8}\hat{g}_{0_P} + \frac{1}{24}\hat{g}_{0_S}\right) \tag{3.12}$$

where the subscripts n and s are the northern and southern faces, respectively, from the node P, and N and S are the CV nodes in the same notation.

Applying the operations above to the other CV faces gives rise to a sparse linear complex system for $\hat{g}_0$, which is solved numerically by a direct banded solver. The solution of the adjoint Green's function was validated in previous works, such as Goldstein (2003); Goldstein and Leib (2008); Leib and Goldstein (2011). The centered difference scheme was adopted due to its intrinsic less diffusive behavior, compared to the upwind schemes, as observed by Meira and Souza (2020) in HVAC simulations. Despite the fact that the nature of events is likely different for jet noise, although the fluid flow properties propagate hyperbolically in compressible flows, in transonic/subsonic conditions, the sound propagation follows a quasi-elliptical propagation pattern. Due to this, a more conservative scheme is mandatory for overtakes the diffusive and disappearance of acoustic information.

3.3.2 Aeroacoustic Meshing

In this study, the acoustic mesh for the Computational Aeroacoustics (CAA) code is the computational grid specifically designed to accurately predict far-field noise based in near-field flow properties. Unlike a standard Computational Fluid Dynamics (CFD) mesh, which is a three-dimensional domain discretization, the acoustic mesh used by FastJetNoise code is composed by several gauge lines (for 2D cases) or planes (for 3D cases) revolved in an structured cylindrical mesh performed by the code available in Annex B.

The most critical requirement for an acoustic mesh is that it must be fine enough to resolve the wavelength and capture the gradients of the flow properties properly. As described in the Chapter 4, a CFD and CAA mesh dependency studies were carried out.

If the mesh is too coarse, it can completely dissipate the acoustic signal. Furthermore, acoustic waves are sensitive to rapid changes in grid spacing. Therefore, the acoustic mesh should be as uniform as possible to avoid generating spurious numerical reflections that corrupt the solution and mimic false sound sources.

3.3.3 LAPACK Library

Once the FastJetNoise code uses the FVM technique, it requires to solve linear equation systems, (Meira and Souza, 2024). As described in *Numerical Modeling* section, it uses a public library package available in the numerical methods medium, named LAPACK. The Linear Algebra PACKage (LAPACK) is a widely-used and highly optimized library for numerical linear algebra, with its core routines written in Fortran F90. It is considered an industry standard for scientific and engineering computing. LAPACK provides a comprehensive set of routines for solving common linear algebra problems such as systems of linear equations ($Ax = b$), eigenvalue problems, and singular value decomposition.

The library, created in 1992, is designed to perform efficiently on a variety of modern computer architectures, including vector processors and shared-memory multiprocessors, largely by leveraging the highly optimized BLAS (Basic Linear Algebra Subprograms) library for its low-level, high-performance vector and matrix operations. LAPACK's design allows it to exploit memory hierarchies like CPU caches, which makes it significantly faster than its predecessors, LINPACK and EISPACK, on modern machines. The library's source code is freely available and has been used in countless commercial and academic software packages.

The main references and portals for more detailed information and access to the library itself, are: the *Netlib.org*[1]: This is the official home of the LAPACK project. In this repository one can find the source code, documentation, and user guides. The LAPACK User's Guide is a particularly valuable resource that provides a detailed overview of the library's design, routines, and calling conventions; *GitHub*[2]: The LAPACK development repository is also hosted on GitHub, which allows for community contributions and bug reports. This is a plataform to find the latest version of the code and track its development; and *NERSC*[3]: The National Energy Research Scientific Computing Center provides excellent documentation on how to use LAPACK, including how to link it with different compilers and access the C-language interface versions.

---

[1] URL: https://www.netlib.org/lapack/

[2] URL: https://github.com/Reference-LAPACK/lapack

[3] URL: https://docs.nersc.gov/development/libraries/lapack/

4 Results and Discussions

This chapter presents the main results and findings of this study, organized into three main sections to provide a clear and logical progression of the research. First, the provided experimental results are discussed and the Physics around the impact of each PNRD geometry in noise reduction is observed. Second, the credibility of the computational framework is established through a proper verification and validation campaign. This process is centered on the baseline 2D R40 nozzle, where the CFD methodology, performed using ANSYS Fluent, is meticulously verified for numerical accuracy and validated against known data. The CFD results, which describe the fluid dynamics of the jet, are then extracted and interpolated onto a cylindrical mesh to serve as the input for our CAA simulations. This section concludes with a detailed presentation of the Power Spectral Density (PSD) for the R40 case, which serves as a benchmark for subsequent analyses.

The final part of this chapter applies the verified methodology to more complex, three-dimensional geometries. Building on the insights and best practices derived from the R40 case, the analysis is extended to different Passive Noise Reduction Devices (PNRDs), specifically the SC and IN geometries. This extrapolation demonstrates the versatility of the method and its practical application in evaluating novel designs. The discussion will focus on comparing the performance of these PNRDs to the baseline R40 nozzle, with a particular emphasis on their noise reduction capabilities. Finally, the chapter sets the groundwork for the subsequent analysis, which delves into the intricacies of applying the CAA method to three-dimensional cases.

4.1 Verification and Validation

In the development of the FastJetNoise code for the acoustic simulation of transonic jets, establishing the model's credibility is paramount. This process is systematically achieved through the verification and validation campaign, described in this section. Verification is the process of confirming that the code accurately solves the underlying mathematical model. During this internal check, several steps where tested and confirmed for further analysis, such as: mesh generation, memory and variable management, output files, etc. For our acoustic simulation, verification involves comparing the code's output for simplified cases against known CFD results and baseline acoustic signatures for R40 nozzle. Mesh convergence studies to ensure the solution were performed and accounted. At the end of this section, an external check where the code's predictions for acoustic fields and sound pressure levels are compared directly with experimental data obtained from physical measurements of transonic jets, provided by FJR at Doak's Laboratory.

4.1.1 R40 Case ($M_a = 0.7$)

After setting up the previously described cases (see Chapter 3), the ANSYS Fluent, in its student version, solver was used to perform them on a common laptop, totaling 2.5 CPU.h on an Intel™ i3 5005U processor in a single serial run for the 2D R40 tests. This initial tests consists in the verification and validation of the FastJetNoise code, as to as the good practices to produce more reliable results.

The validation procedure was conducted using the round nozzle configuration R40 , which corresponds to a cold subsonic jet with an acoustic Mach number of $M_a = 7$. The main flow and thermodynamic parameters adopted for this configuration are summarized in Table 4.1. The nozzle has an exit diameter of $40\,\text{mm}$ and operates with a total pressure of $156{,}200\,\text{Pa}$, resulting in a pressure ratio of 1.4231 relative to the ambient conditions. The jet issues at a total temperature of $291.11\,\text{K}$, near to the ambient static temperature of $286.32\,\text{K}$, confirming that the flow can be classified as a cold jet. Under these operating conditions, the fully expanded jet Mach number is $M_j = 0.7282$, which corresponds to a measured exit velocity of $236.85\,\text{m/s}$.

Table 4.1: Parameters used in R40 ($M_a = 0.7$) for validation cases cases.

	Round Nozzle
Description	R40
Diameter [mm]	40
Ambient pressure [Pa]	101,540
Ambient temperature [K]	286.32
Pressure ratio [-]	1.4231
Jet total temperature [K]	291.11
Jet velocity [m/s]	236.85
Jet Mach [-]	0.7282
Acoustic Mach [-]	0.70
Freestream Mach [-]	0

Cold jets are particularly suitable for numerical validation because they minimize the influence of thermal gradients, allowing a clearer assessment of the turbulence modeling and numerical accuracy. The experimental results used herein and in several material studies (Almeida et al., 2014; Lawrence, 2014; Proença, 2018) deals with this type of cold jets or, in some situations, near isothermal (Jordan et al., 2002). In such flows, the dominant physical processes are associated with shear-layer development, turbulent mixing, and the decay of the mean axial velocity downstream of the nozzle exit. Therefore, the R40 case provides a well-controlled benchmark for evaluating the predictive capabilities of the simulation setup, especially regarding the representation of the jet potential core and its subsequent decay. The availability of high-quality experimental data for this configuration further strengthens its use as a reference case for the assessment of computational results.

4.1.2 CFD Mesh Independence Study

A mesh sensitivity analysis was performed to assess the influence of mesh resolution on the predicted flow field and flow properties. Six structured meshes were generated by means ANSYS ICEM CFD in a structured block approach. The produced meshes ranges from approximately $25{,}000$ to $120{,}000$ cells, as depicted in Figure 4.1. These meshes differ primarily in the axial and radial grid refinement, particularly within the jet shear layer and potential core region, which are critical zones for accurately capturing turbulence dynamics and noise generation. The coarser meshes were used to evaluate numerical robustness and computational cost, whereas the finer grids served to establish the asymptotic convergence of key flow quantities. This systematic approach is fundamental to establishing the credibility of the simulation results before they are used to predict complex phenomena related to JMN.

The cases performed to validate CFD results and findings around mesh resolution used the same inputs, as available in Table 4.1. As expected the coarse meshes produced extremely fast results, approximately dozen minutes, depending on the initialization of the cases. The most refine one – seen in Fig. 4.1 (f) – took approximately $1.5\,$CPU.h in a common laptop.

The main indicator for assessing mesh convergence was the time-averaged axial velocity decay along the jet centerline, normalized by the jet exit velocity, described by

$$\frac{\langle u \rangle_t}{U_j} \tag{4.1}$$

where, $\langle u \rangle_t$ is the time-averaged axial velocity and U_j is the maximum core velocity.

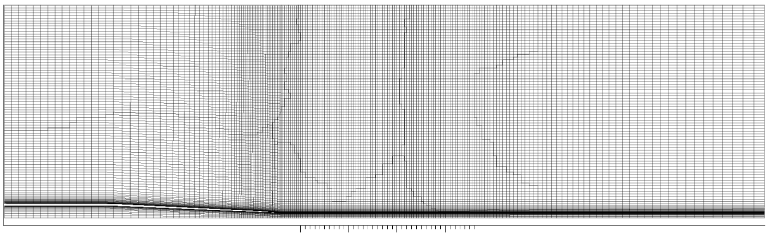

(a) 25 k.

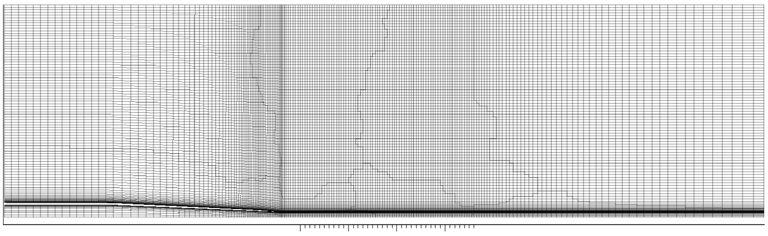

(b) 26 k.

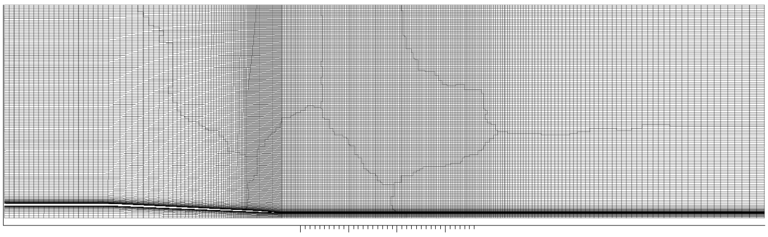

(c) 52 k.

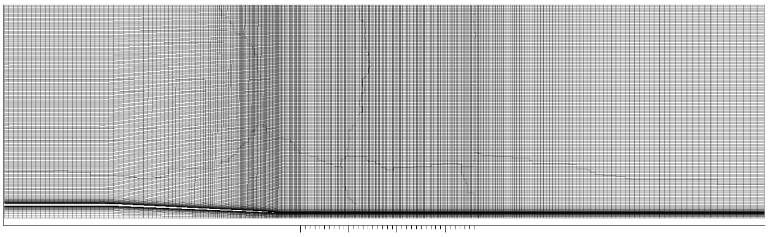

(d) 75 k.

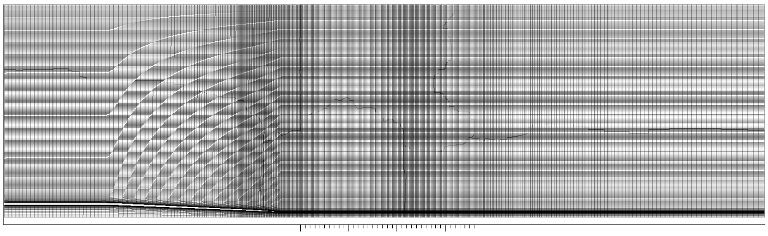

(e) 100 k.

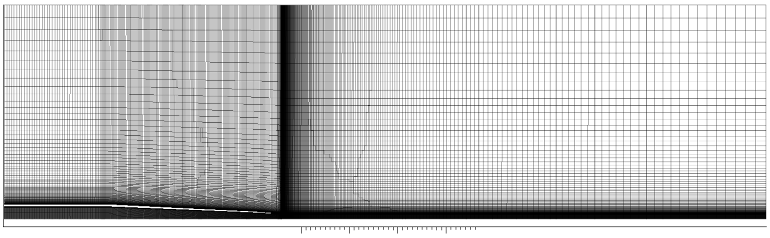

(f) 120 k.

Figure 4.1: R40 meshes used in validation.

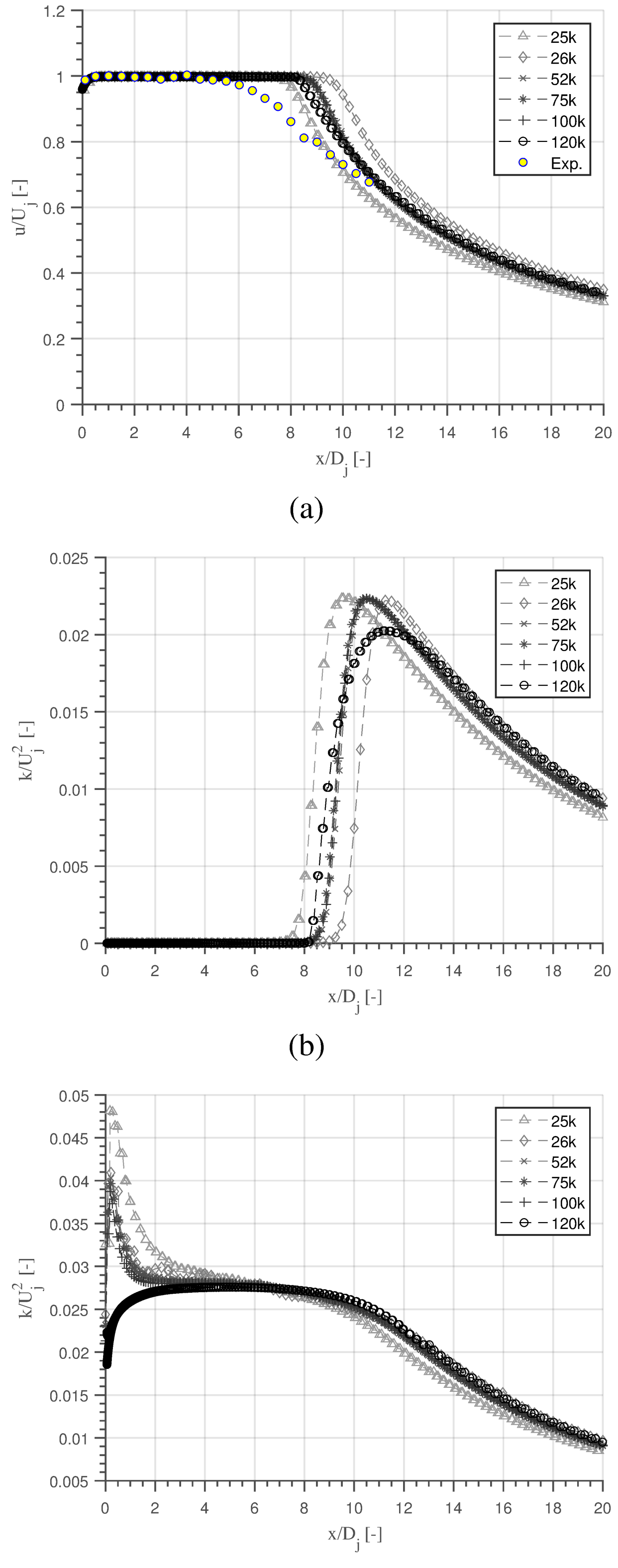

(a)

(b)

(c)

Figure 4.2: Centerline profile of time-averaged axial velocity (a), centerline profile of turbulent intensity (b), and lip line turbulent intensity (c) vs experiments by Jordan et al. (2002).

This quantity was compared against the experimental data obtained by Jordan et al. (2002), as shown in Figure 4.2. The comparison reveals that all computational meshes capture tendency of the potential core decay. However the numerical results presented a more intact and elongated core, extending up to approximately in the range of $8 \leq x/D_j \leq 9.5$. Within this range, it is observed that the most refined meshes converge to value of core length $L_c = 8.5D_j$.

While the 25k mesh reveals a sub-prediction in the core length, the 26k mesh presents an overshoot in this parameter. The main difference between these meshes states on the value of the adopted y^+ for the duct inner wall. The 25k was made with $y^+ = 30$, while the 26k was made with $y^+ = 1$; this difference affects directly the results in core length, which is more elongated for the 26k mesh. It suggest that, by means of the numerical diffusion of the 25k mesh predicted velocity remains nearly constant and in excellent agreement with the experimental measurements.

Beyond the potential core ($x/D_j \geq 5$), the flow starts to decay as turbulent mixing increases. Coarser grids (25k and 26k cells) exhibit a delayed decay and an overestimation of the mean velocity, indicating insufficient spatial resolution to properly resolve the turbulent shear layer development. As the grid is refined to 52k and 75k cells, the agreement with the experimental data improves significantly, particularly in the transition region ($5 \leq x/D_j \leq 10$). Further refinement to 100k and 120k cells results in only marginal differences, suggesting that the solution has reached grid convergence.

Based on these results, the 120k-cell mesh was selected as a more appropriate configuration for subsequent simulations. This grid provides a satisfactory compromise between computational cost and solution accuracy, ensuring that both mean flow and turbulence characteristics are adequately resolved. The observed convergence behavior confirms that the flow field predictions are mesh-independent, providing confidence in the reliability of the acoustic source data extracted from the second-order CFD results.

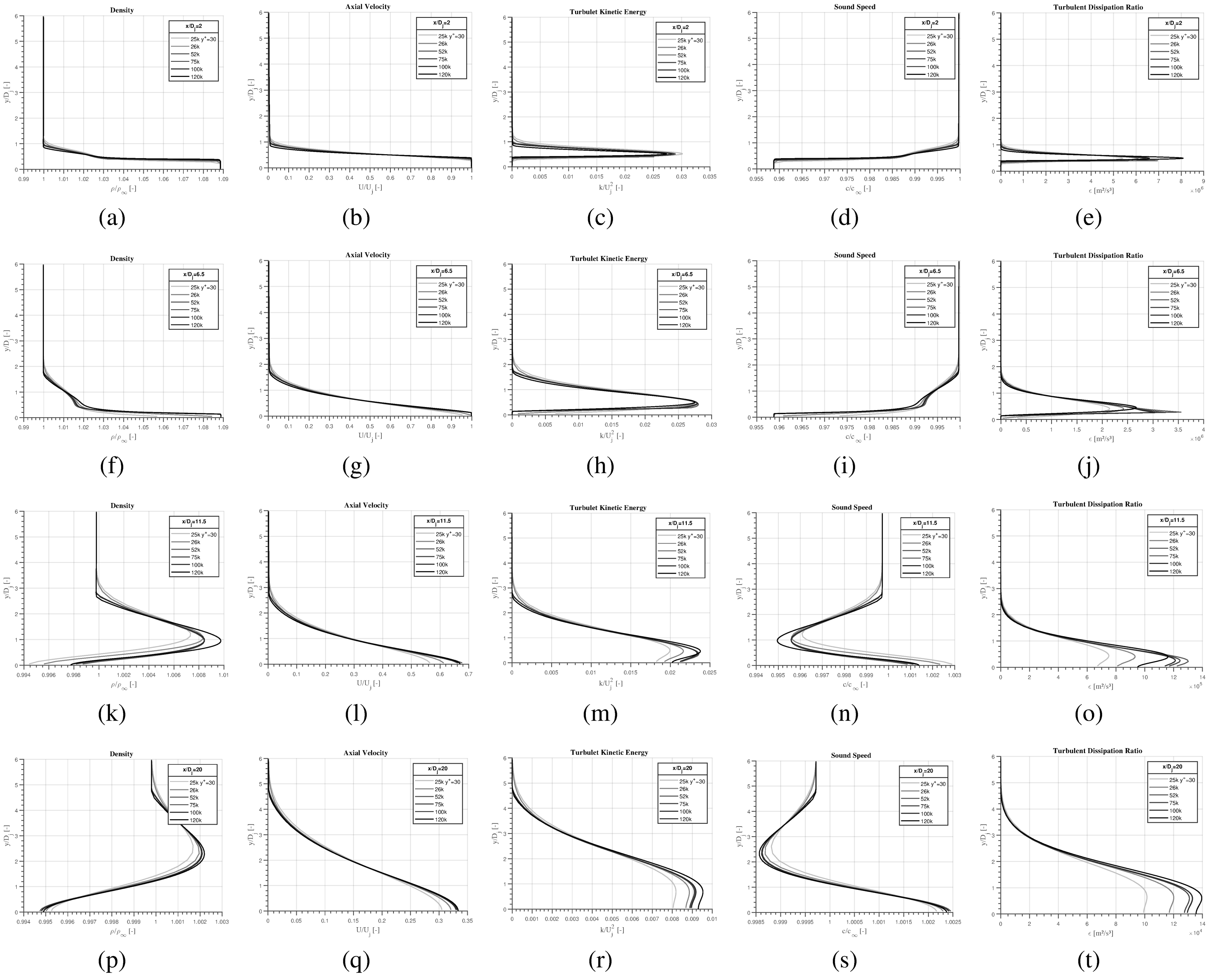

Figure 4.3: R40 radial profiles of extracted properties from CFD simulations.

The Figure 4.3 presents the radial profiles of key flow properties – axial velocity (U); density (ρ), turbulent kinetic energy (k), local sound speed (c), and turbulent dissipation/transformation ratio (ε) – at four different downstream locations ($x/D_j = 2.0, 6.5, 11.5, 20.0$) for all tested mesh resolutions.

This part of grid sensitivity study is to demonstrate that the CFD mesh and its topology affects directly the profiles that should be used as CAA input, and, consequently, the noise prediction in far-field. As can be seen in Fig. 4.3, the profiles for the coarser meshes (25k, 26k, and 52k) present a strong numerical diffusion, especially in farther downstream planes; this diffusion can be observed even radially in the profiles. It is observed that y^+ contributes significantly in the CFD solutions and the profile diffuseness; the 25k-cells does not represent correctly the boundary layer effects that occur inside the nozzle tube, and this sub-prediction propagates on subsequent downstream planes and profiles.

The figure clearly illustrates the evolution of the jet flow as it propagates downstream. At the near-field location ($x/D_j = 2.0$), shown in panels (a-d), the profiles are highly uniform across the jet core, with a sharp gradient occurring only within the thin shear layer at the jet's outer edge. The axial velocity remains close to the jet exit velocity, and the turbulent kinetic energy is minimal, peaking slightly at the shear layer interface. This signifies the presence of a potential core, where the flow properties remain largely unmixed.

As the jet progresses downstream, at ($x/D_j = 6.5$) (charts (f)-(i)), the shear layer has grown significantly. This growth is evidenced by the gradual reduction in the core's velocity and the widening of the region with a velocity gradient. The normalized turbulent kinetic energy (k/U^2) profiles now show a distinct peak within this growing shear layer, indicating the start of intense turbulent mixing. This trend continues at ($x/D_j = 11.5$) (panels (k)-(n)), where the potential core is largely decreased. The shear layer has expanded radially, leading to a broader region of reduced velocity and a more pronounced peak in turbulent kinetic energy. Finally, at the last extraction plane ($x/D_j = 20.0$) (charts (p)-(s)), the potential core completely decayed, and the velocity profile has become parabolic, characteristic of a fully developed jet. The turbulent kinetic energy is at its maximum intensity, and the turbulent mixing region spans a much larger radial extent.

In Figure 4.4, the three graphs present the PSD by Strouhal number of far-field noise spectra for the R40 nozzle at three different polar angles (43°, 61°, and 90°). The primary purpose of this graphs is to evaluate the effect of CFD mesh refinement on the acoustic prediction. In each plot, the dashed blue line represents the experimental data (Exp R40), serving as the benchmark against which the CFD results are compared. The CFD results are plotted with solid lines of varying shades, each corresponding to a different mesh size, ranging from 25 thousand (25k) to 120 thousand (120k) volumes.

For the shallow angle of 43° (Fig. 4.4 (a)), the primary effect of mesh refinement on the CFD-predicted PSD lines is a vertical shift across the entire Strouhal number (St) range. This PSD magnitude increase with refinement suggests that finer meshes are better able to resolve the near-field flow profiles (potentially seen in Fig. 4.4, which is assumed to be the correct reference), leading to a more representative noise source for shallow radiation angles. The implication is that the coarseness of the profile near the jet exit is directly influencing the overall predicted noise power.

Conversely, for the higher polar angles (61° and 90°) in Fig. 4.4 (b) and (c), the impact of mesh refinement appears to be characterized by a shift or "rotation" of the PSD lines, particularly in the direction of higher Strouhal numbers. This rotation indicates that, as the mesh resolution increases, the CFD computation is better able to preserve and predict the high-frequency acoustic components. This is an expected result, as modeling and preserving smaller, faster-moving turbulent eddies – the sources of high-frequency noise – requires a much finer spatial discretization. Thus, the finer meshes yield a more accurate representation of the acoustic energy distribution across the entire frequency spectrum at these broader angles by means the more defined profiles in near-field (see Fig. 4.3).

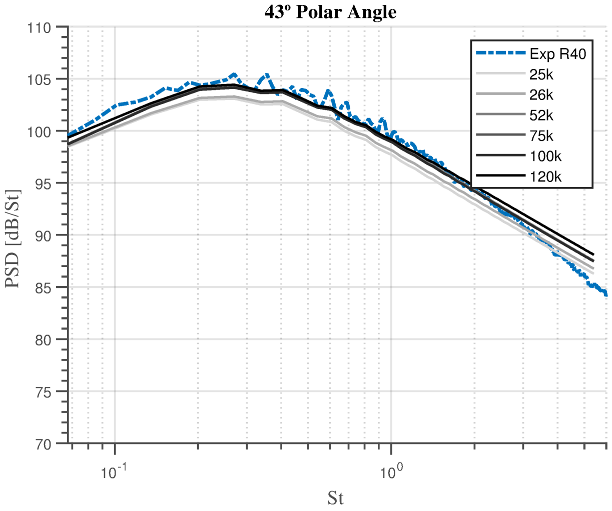

(a) 43°.

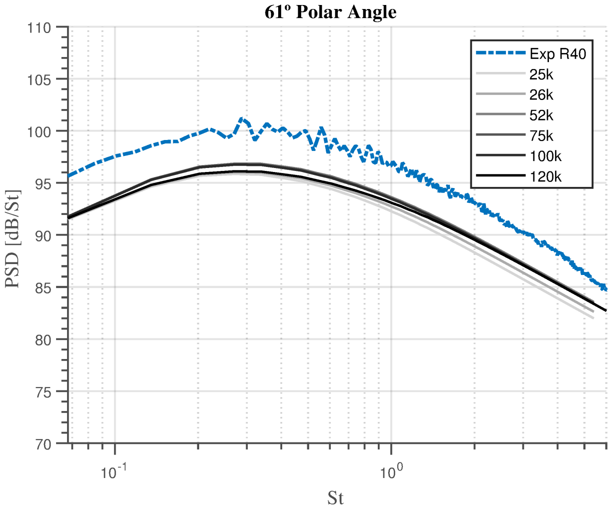

(b) 61°.

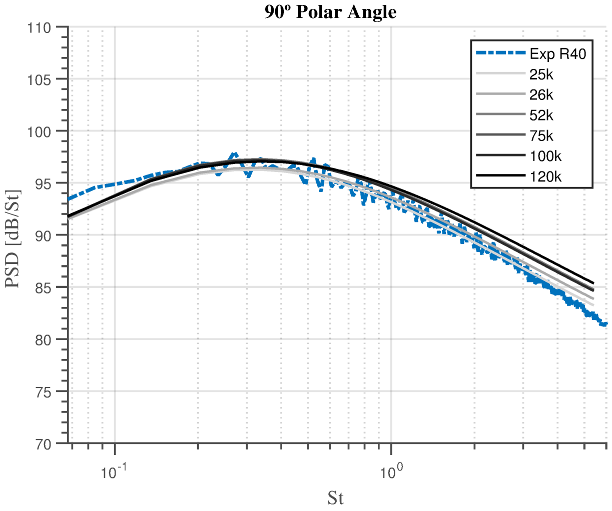

(c) 90°.

Figure 4.4: Far-field spectra of R40 nozzle performed with results of CFD mesh refinement.

In conclusion, the mesh sensitivity analysis highlights the crucial impact of near-wall mesh resolution. A significant difference is observed between the coarse 25k mesh ($y^+ \approx 30$) and the 26k mesh ($y^+ \approx 1$). The first mesh, which uses a wall function approach to model the boundary layer, fails to accurately resolve the flow properties, particularly in the near-nozzle region. For instance, in Fig. 4.3 (a)-(c), the 25k mesh exhibits a premature drop in axial velocity and an inaccurate representation of the turbulent kinetic energy profile. This discrepancy is a direct consequence of the wall function's inability to precisely model the boundary layer effects, for these coarse meshes. In contrast, the 26k mesh, with a non-dimensional wall distance ($y^+ \approx 1$) of approximately 1, directly resolves the viscous sub-layer. This characterization is important and evident in some authorship works that involve internal flows, such Meira and Souza (2020); Meier et al. (2023). This allows for a much more accurate prediction of the shear layer's initial development and, consequently, the downstream flow evolution. This difference underscores the necessity of a fine near-wall mesh (low y^+ values) to accurately capture the initial shear layer growth and the subsequent turbulent mixing behavior, which are fundamental to the jet's overall decay and noise generation characteristics. All the other meshes, greater than the 26k mesh, have the adoption of $y^+ \approx 1$ for the inner wall of the nozzle.

4.1.3 CAA Mesh Independence Study

Dealing with 2D cases, in an axisymmetric approach, a series of line probes were used to extract flow properties downstream from the nozzle, such as near-field properties. An example of the results extracted from CFD simulations is described in the Annex A. These properties are crucial to generate input for the FastJetNoise code, including position (x,y), local fluid density (ρ), axial velocity (U), turbulent kinetic energy (k), turbulent dissipation rate (ε), and local sound speed (c).

The FastJetNoise code generates a structured mesh using the properties extracted from CFD data through a revolution operation in cylindrical coordinates. The FORTRAN routine that creates this mesh is listed in Annex B. One notices that this function is called independently of the topology of the case, i.e. the 2D or 3D meshes are performed by the same code. The only point to note is the geometric parameters passed by the input card (Annex C), such as the type of CFD data (2D or 3D), the partial number of cells, and the number of sectors. As demonstrated by Goldstein (2003); Leib and Goldstein (2011), the region most important in obtaining near-field properties is in the range of ($2 \leq x/D_j \leq 20$), where x is the axial location of the line probe and D_j is the diameter of the nozzle. Due to the intrinsic nature of the CAA method, which uses a Riemann integral of the properties of the plans, the data must be sorted according to the axial reference. This concern is recommended by reason of some CFD solvers, such ANSYS Fluent, export data in non-structured meshes in an unsorted way, and it produces biased PSD results.

The results of the mesh refinement study for the Computational Aeroacoustics (CAA) simulations are presented in Figure 4.5. The figure displays the PSD spectra computed at a polar angle of 61°, for meshes ranging from 25k to 120k cells from CFD campaign. This polar position was specifically chosen because it represents one of the most challenging observer locations: previous tests have shown that predictions at 61° tend to exhibit the largest deviation from the experimental data. Thus, this direction provides a sensitive reference for evaluating the effects of grid resolution on the accuracy of the acoustic predictions.

The resolution of CAA mesh was set by changing the number of circular and radial discretizations, i.e. the N_ϕ and N_r were changed at the values of 200, 300, 400, and 500 divisions, assuming $N_\phi = N_r$ for a regular mesh analysis. These parameters are defined in the input card (see Annex C) labeled by the terms *n_phi* and *n_radial* for N_ϕ and N_r, respectively.

The increase in CAA mesh resolution did not present a real perceptive change in results. As seen in Figure 4.5 the curves are almost collapsed in the same PSD response. The more refined meshes, with $N_\phi \geq 400$, conferred a slight proximity to the experimental PSD at 61° for all inputs of CFD mesh, from 25k to 120k, presenting a difference less than 1% in the high-frequency band, compared to coarse meshes. These findings suggest that the CAA methods implemented in FastJetNoise is more susceptible to the CFD discretization than to the acoustic mesh resolution for 2nd order methods. Further results, described in the next sections, reveal that it does not apply to the 4th order methods, especially in high frequency components. The small remaining discrepancies, particularly at low frequencies, are likely due to modeling limitations rather than numerical resolution.

Overall, the mesh refinement study confirms that CAA predictions do not present a considerable sensitiveness to grid density, especially at observer angles where discrepancies are more pronounced. The use of 61° as a reference angle proved valuable in identifying the threshold convergence of the CAA mesh and ensuring that the PSD results were not artificially influenced by flow features that were not properly solved.

Despite the slight gains with CAA refinement, its computational cost must to be accounted. The Figure 4.6 plots the relationship between CPU time and the number of angular (and radial) discretization points ($N_\phi \times N_r$) for a given CAA mesh performed by FastJetNoise. This type of analysis is a critical part of a grid sensitivity study, which is essential for ensuring that the simulation results are reliable against their computational cost. The chart reveals a clear, non-linear trend between computational cost and mesh refinement. This is a common

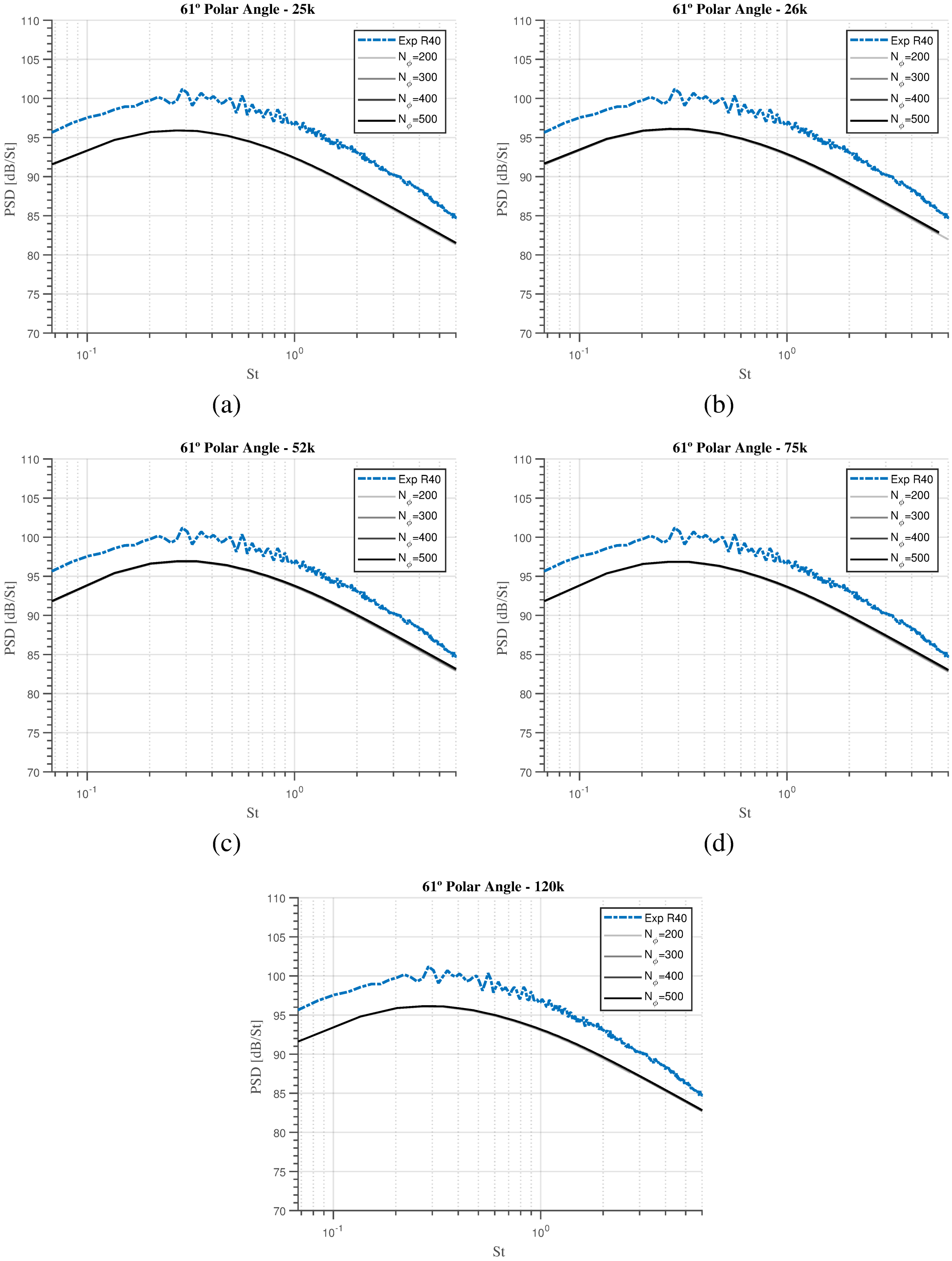

(a) (b) (c) (d) (e)

Figure 4.5: Far-field spectra of R40 nozzle ($\theta = 61°$) performed for different CAA meshes.

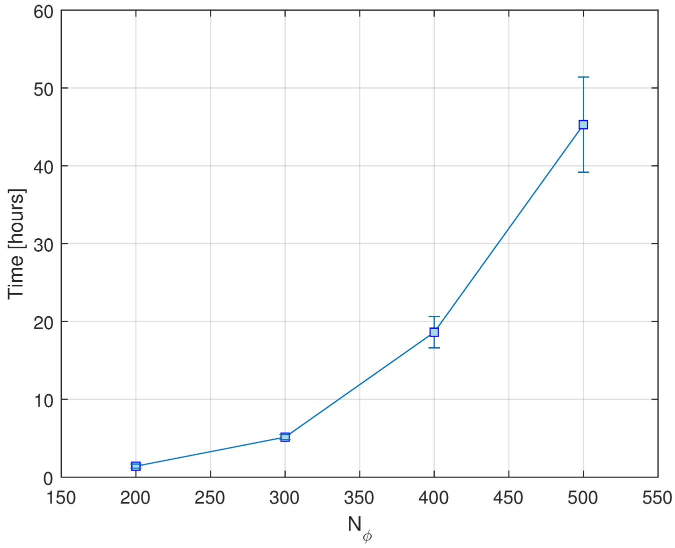

Figure 4.6: CPU time by N_ϕ AAC mesh discretization.

and expected result in CFD and CAA simulations, as pointed by Maliska (2010); Ferziger and Peric (2012); Hardin and Hussaini (2012). When a mesh is refined, the total number of cells or elements increases, but the computational cost scales with the number of cells raised to a power greater than one. This is because a finer mesh also contributes to a major number of iterations to maintain numerical stability, until the convergence.

This result also represents the fundamental trade-off between solution accuracy and computational cost in CAA. While a coarser mesh ($N_\phi = 200$) offers a significant reduction in computational time (in average $1h\,26min$), the accuracy of the far-field PSD prediction, may be partially compromised. On the other hand, a highly refined mesh ($N_\phi = 500$) demands a disproportionately large computational effort (in average $45h\,18min$), leading to a much longer and unfeasible simulation time, but provides a more accurate and robust solution, especially for high frequencies (high Strouhal numbers). As recommended by Goldstein and Leib (2008); Leib and Goldstein (2011) the values of N_ϕ do not produce practical results in ranges much smaller than 300, according to them it can causes certain deviations in high-frequency prediction, however they do not regards around the computational cost.

Although this indicates that while the finer meshes provide a more accurate solution, the marginal gain in accuracy might not justify the substantial increase in computational resources required. The error bars, which represent the uncertainty or variability in the measurements, also grow with increasing mesh size, highlighting the greater computational instability and complexity associated with finer meshes.

In the context of the implemented GAA (see Chapter 3), accurately resolving the flow properties is crucial. The increase in N_ϕ is directly related to the ability to capture higher-frequency acoustic modes and accurately model sound propagation (Green's function $\hat{g}_0$ in Eq. 3.7). Then is more important to produce reliable CFD results than to perform finer meshes in CAA simulations. These findings are central to the practical application of this acoustic analogy in real engineering problems.

4.2 Passive Noise Reduction Devices

Following the comprehensive verification and validation of the axisymmetric R40 jet case, the focus of this section transitions to an in-depth analysis of Passive Noise Reduction Devices (PNRDs). These devices, which rely on geometric modifications rather than active control systems, are a primary subject of this thesis due to their potential to significantly reduce jet noise. The investigation expands from the baseline axisymmetric nozzle (R40) to a brief, yet critical, study of non-axisymmetric geometries (see Figures 3.4-3.5).

The central contribution of this work lies in the Power Spectral Density (PSD) estimation for the previously presented PNRDs. The PSD, which quantifies the distribution of a signal's power over frequency, is a fundamental metric in aeroacoustics for characterizing jet noise. This study employs and evaluates two distinct numerical schemes for PSD estimation within the CAA code (FastJetNoise): a 2nd-order scheme and a 4th-order scheme. The application of these higher-order schemes is essential for accurately capturing the complex and broadband nature of jet noise, especially for non-axisymmetric flows where the sound field is no longer uniform in the azimuthal direction.

The methods and best practices established during the R40 validation campaign, including the grid independence study and the careful extraction of flow properties from CFD simulations, were directly applied to these more complex non-axisymmetric cases to ensure a consistent and rigorous methodology.

4.2.1 Non-Axisymmetric Nozzles at $M_a = 0.8$

Once the 3D cases demanded larger meshes, above 1 Mi of volumes, a proprietary license of ANSYS FLuent needed to be used in each run. Similarly with the R40 validation campaign, a brief mesh refinement study was carried out for SC03 geometry. This proved necessary to ensure the best radial discretization of the wedge sector to other PNRD geometries.

The results presented in Figure 4.7 summarize the mesh independence study conducted for the SC03 geometry used as further extrapolations for subsequent SC geometries. The axial profiles of the normalized time-averaged axial velocity (u/U_j), normalized turbulent kinetic energy (k/U_j^2), and their behavior along both the jet core and lip line demonstrate that the global flow characteristics remain virtually unchanged among the different mesh densities. The perceptible overlap of the profiles confirms that the essential flow quantities are fully resolved within the employed discretization levels. This agreement across all configurations attests to the numerical robustness of the RANS solution and ensures that the acoustic predictions derived from these fields are not contaminated by grid-related artifacts.

A slight deviation is only observed for the *corrected-lip* (CL) configuration, in which additional mesh refinement was applied along each corrugation of the nozzle lip. This local refinement produces marginal improvements in the resolution of the shear layer gradients without altering the global flow structure, as indicated by the preserved velocity decay and TKE peak locations. Such consistency demonstrates that the baseline grid already captures the relevant jet features with sufficient fidelity, while the CL refinement confirms that the flow solution is spatially converged even under localized mesh modifications.

Consequently, the simulations can be regarded as mesh independent for all practical purposes, providing a solid foundation for the subsequent acoustic analyses. The final mesh with the corrugation correction is used for all other SC geometries.

In a similar way, as seen in R40 validation campaign, the finer mesh in SC03 (1.68 Mi with CL) simulations presented more reliable PSD results with a slight difference of the other meshes, as seen in Fig. 4.7 (a) and (b). All CAA simulations with SC03 CFD results were performed with a $N_\phi = 300$, whereas, as seen previously, confer a good accuracy with no expressive computational cost (Goldstein and Leib, 2008).

As observed in R40 core decay, the SC03 meshes presented a more conservative and elongated core length, with $x/D_j \approx 8.7$. As can be seen in Fig. 4.7, the image describes how the model over-predicts the length of the jet's potential core, a common issue with turbulence models, especially in RANS approach. These models rely on simplified assumptions about turbulence and use coefficients that must be determined empirically for $k - \varepsilon$ model, often by calibrating them with experimental data.

The same pattern was obtained by Silva (2011) in entire domain RANS simulations. This approach has a notable drawback – the calibration process is limited by the specific conditions of the experimental data used. Consequently, a model calibrated for a simple flow may not accurately capture the more complex physics of other, different flows. This can lead to discrepancies and inaccuracies in the predictions.

As this issue is commented in the work of Pope (1978), named jet anomaly, this problem arises because many turbulence models fail to accurately predict the velocity decay of round or planar jets. He attributed this to vortex stretching, which causes greater dissipation and a

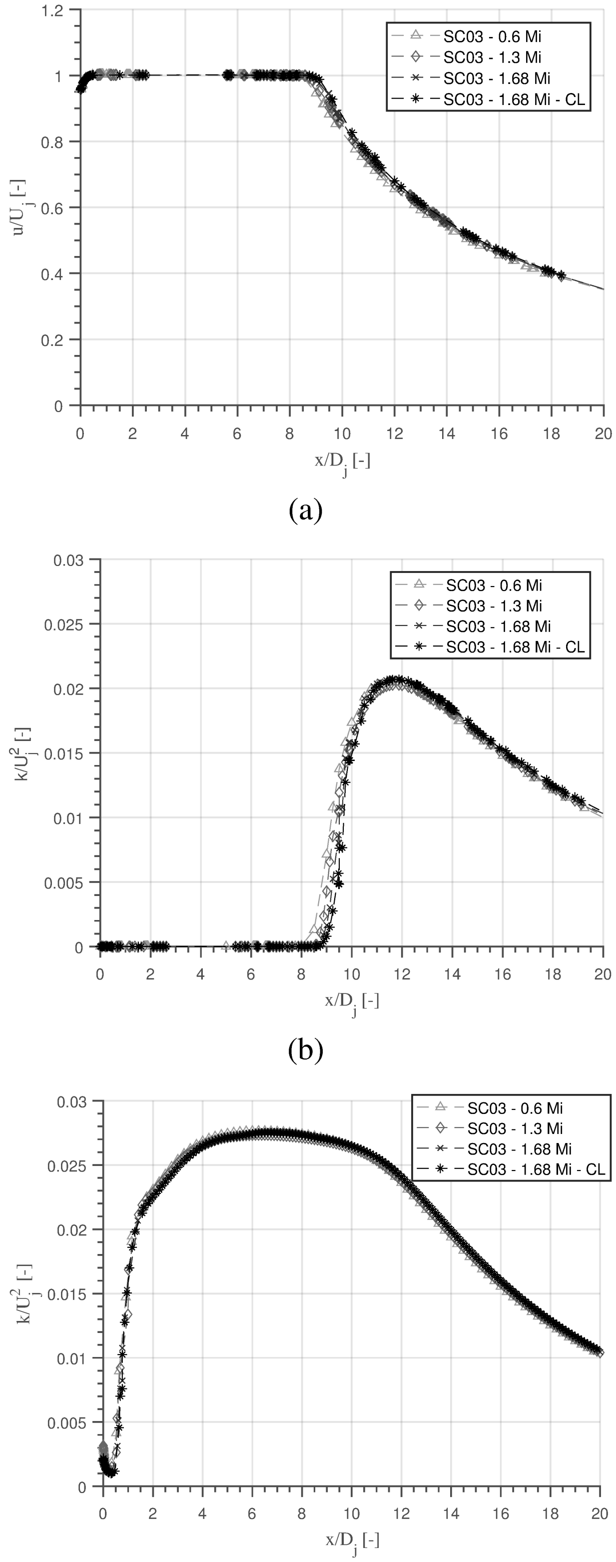

(a)

(b)

(c)

Figure 4.7: Axial profiles of time-averaged axial velocity at core (a), turbulent kinetic energy at core (b), and at the lip line (c).

lower effective viscosity, especially in axisymmetric jets. To fix this, he proposed modifying the constants in the dissipation equation of turbulence models, specifically $k-\varepsilon$.

A survey by Nallasamy (1999) on turbulence models used for jet noise computation also discus this issue. The main finding was that incorporating anisotropic turbulence characteristics would significantly improve the accuracy of jet flow predictions. As a recommendation, the correct prediction of core length and, consequently, the downstream properties profiles can be achieved by the use of tuned constants for $k - \varepsilon$ model (Eqs. 3.3-3.4). This possible future work is a key point to evaluate the robustness of the GAA implemented model.

Once the 3D simulation standard mesh was defined, it was adapted for the SC06, SC09, and SC12 nozzles. The main characteristics of the resolved fluid flow was first observed and investigated to, at another step, perform the CAA simulations in FastJetNoise code. For a better view, a batch of visualizations in downstream resolved field is disposed in Figure 4.8, where each row exhibits the geometry visualization for the baseline (R40), SC03, SC12, and IN nozzles. The columns present the properties, being: axial velocity (U), turbulent kinetic energy (k), turbulent dissipation ratio (ε), and temperature (T).

As a qualitative assessment of the differences between the cases, these visualizations provide a high-level overview of the main flow characteristics and allow for basic inferences around the correlations between the growth of instabilities in downstream direction, the mixing process, the strength of turbulence intensity caused by PNRD geometries, and, subsequently their implications in noise generation.

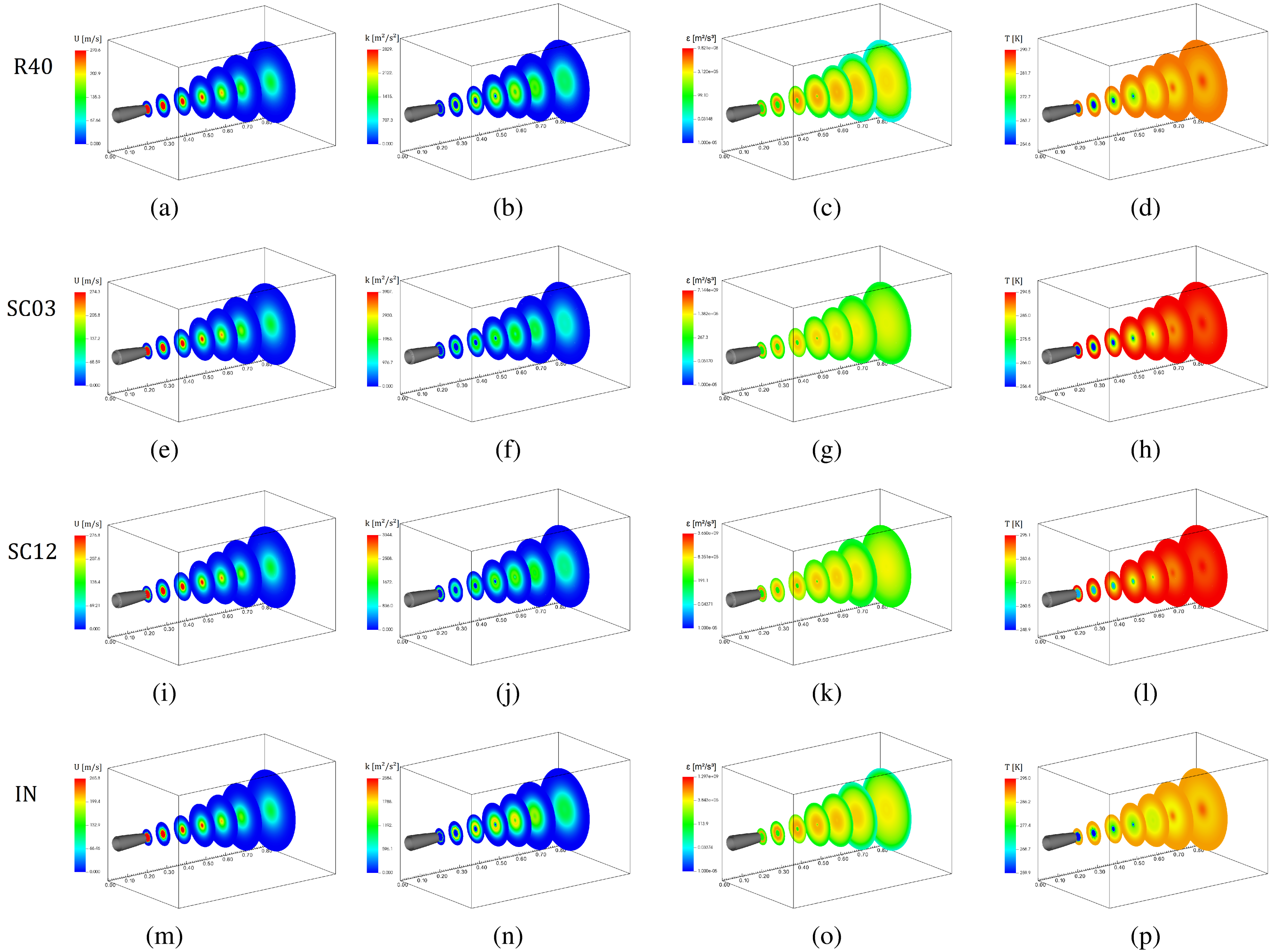

(a) (b) (c) (d)

(e) (f) (g) (h)

(i) (j) (k) (l)

(m) (n) (o) (p)

Figure 4.8: Flow field for different nozzles at $M_a = 0.8$.

For all cases, the axial velocity field (plots (a), (e), (i), and (m)) displays a clear potential core region near the nozzle exit, where the velocity remains high and uniform, and the potential core extends up to $x/D_j \approx 8$. As the flow moves downstream, the jet spreads and entrains ambient air, causing the velocity to decay. This decay is directly linked to the growth of the turbulent shear layer, which is visually represented by the increasing magnitude and spread of turbulent kinetic energy (k) in Figures (b), (f), (j), and (n). Similarly, the plots for turbulent dissipation/transformation ratio (ε) and static temperature (T) in the remaining columns follow a comparable pattern, showing the core region and the subsequent mixing with the surrounding fluid.

As observed, the baseline case (R40) presents a more natural diffusive pattern in all mixing layer. On the other hand, the induced turbulence promoted by the corrugations in SC03 and SC12 present a intense swirling movement of the fluid immediately downstream to the nozzle trailing edge, as seen in the first slice, at (e) and (i). As can be seen, these inductions are rapidly dissipated in subsequent downstream slices.

However, a more intricate pattern is observed in IN results, Figure 4.8 (m)-(p). As can be seen, the induction of turbulence occurs in a modest way, and there is the initiation and propagation of the first instabilities for farther downstream regions. The subsequent slices present a lobed shape preserved from the induced turbulence in flow field. This indicates that the induction of turbulence by PNRDs is a necessary condition for noise reduction, however, the intensity of this induction is not sufficient to reduce overall noise, especially in high frequency components, as can be seen by experimental and numerical results. Leib and Bridges (2022) observe this preservation pattern of the globular structure of the core in numerical simulations of chevrons. These geometries were experimentally tested by Bridges and Brown (2004) and, due to this intrinsic extreme low order of rotational symmetry, present different PDS depending on the azimuthal position (ϕ).

Following the contributions and validation of the primary computational methodology, the core of this investigation shifts to a detailed evaluation of the numerical schemes implemented for aeroacoustic prediction. The objective is to assess the accuracy and performance of different numerical orders when simulating the far-field noise spectra (PSD) of the four non-axisymmetric nozzles at an acoustical Mach number of $M_a = 0.8$. Figure 4.9 is a compilation of the far-field spectral results, where the predictions from both the 2nd-order and 4th-order schemes are directly compared against established experimental data. This comparison serves to validate the CAA code's ability to model complex jet noise phenomena and to highlight the advantages of using higher-order numerical methods for this purpose. Each row of this figure presents the three observer angles ($\theta = 43°$, $\theta = 61°$, $\theta = 90°$) for each non-axisymmetric geometry, which are: SC03, SC06, SC09, SC12, and IN.

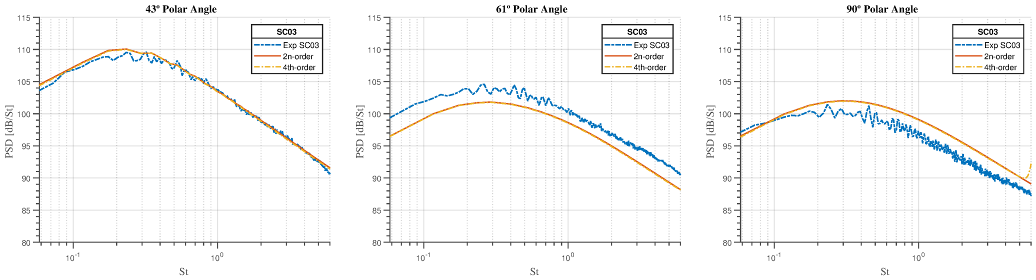

(a) 43°. (b) 61°. (c) 90°.

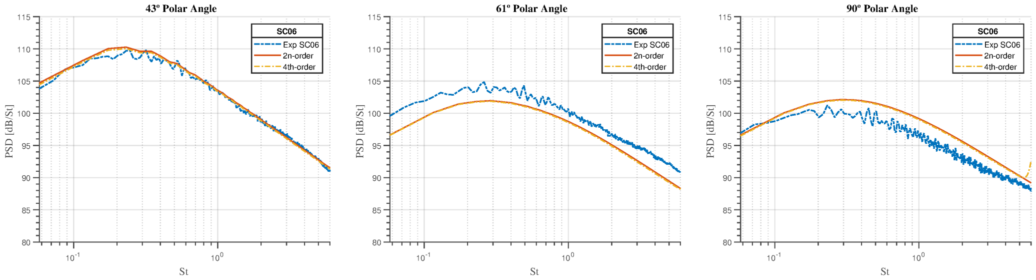

(d) 43°. (e) 61°. (f) 90°.

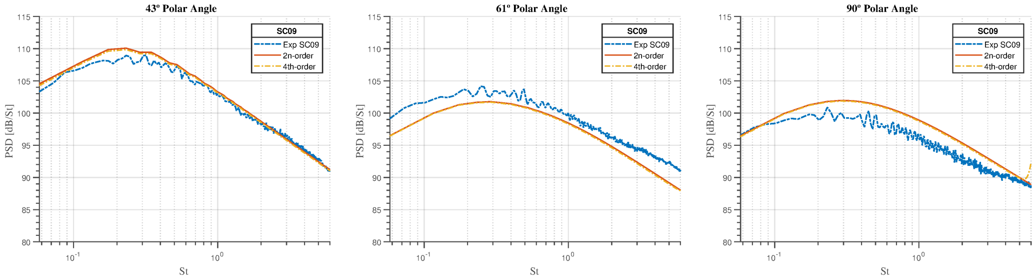

(g) 43°. (h) 61°. (i) 90°.

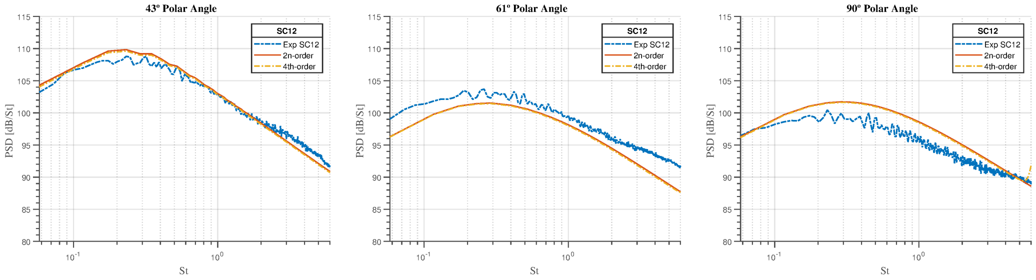

(j) 43°. (k) 61°. (l) 90°.

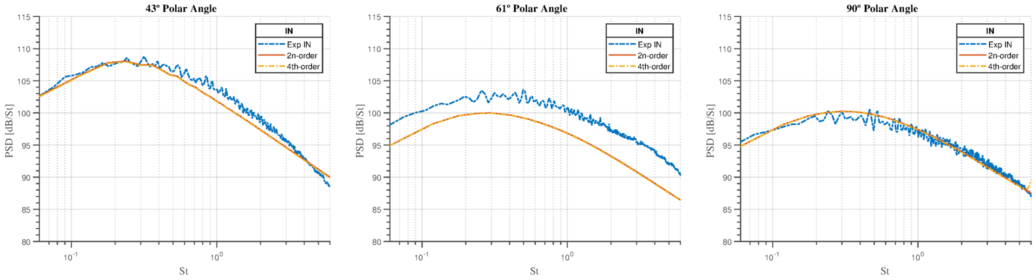

(m) 43°. (n) 61°. (o) 90°.

Figure 4.9: Far-field spectra for non-axisymmetric nozzles - simulations (2nd and 4th order methods) vs experimental data at $M_a = 0.8$.

As shown in Figure 4.9 (a)-(c), there is a comparison between SC03 nozzle at $43°$, $61°$, and $90°$ observer angles. Numerical results exhibit a generally good agreement with the experimental data reported by Doak Lab., particularly in the low- and mid-frequency ranges. This behavior indicates that the underlying flow field and its associated turbulent structures are adequately captured by the computational model, ensuring a realistic representation of the large-scale energy-containing eddies responsible for the dominant acoustic radiation, even though using an averaged flow field by means RANS simulations.

At the shallow angle of $43°$, which corresponds to the downstream direction of the maximum jet noise emission, the PSD curve follows the experimental trend closely, both in amplitude and spectral shape. This agreement suggests that the CFD simulation reproduces the convection and decay of large-scale turbulent structures effectively, and, by an acoustic reference, the GAA implemented technique is adequate to predict jet noise for this observer point.

However, at the intermediate angle of $61°$, a slight sub-prediction of the spectral levels is observed across a wide frequency range. This discrepancy, also noticed in the CFD and CAA mesh refinement studies, highlights the sensitivity of the far-field prediction to the accuracy of the turbulence representation within the shear layer. As stated by Lawrence (2014) the region near this observer angle ($61°$) is strongly dominated by high frequency components (high Strouhal numbers). Finally, at the sideline angle of $90°$, corresponding to the lateral acoustic radiation, the simulated spectrum again aligns well with the measurements, although with a small underestimation at high frequencies likely due to numerical diffusion and CAA mesh resolution limits.

Once the IN geometry is a notched-type nozzle and, as well-known, presents a simple and effectivity topology, it can be employed in real projects. A series of experimental studies performed by Oishi (2010); Ishii et al. (2019) reveal that this simple PNRD presents a less invasive geometry with a low interference in thrust reference of turbofan and turbojet engines. This type of geometry works as chevron-based PNRDs, reducing the low frequency components and slightly increasing the high frequency components (Bridges and Brown, 2004; Leib and Bridges, 2022).

In line with the mentioned experimental works and Doak Lab data (see Chapt. 3), the CAA simulations reproduce the overall spectral shape observed in the IN nozzle – Figure 4.9 (m)-(o). A pronounced broadband peak at low–mid Strouhal numbers and a monotonic roll-off toward higher frequencies is observed in $43°$ polar angle. Both numerical schemes predict the spectral peak location reasonably well, but the 4th-order discretization yields slightly higher amplitudes at mid-frequencies and a closer high-frequency slope to the experiment.

The 2nd-order solution shows somewhat smoother spectra (reduced high-frequency content), consistent with increased numerical diffusion. This indicates that in the downstream direction the principal large-scale turbulent structures (which dominate low-frequency radiation) are captured by the current modeling, while higher-order CAA methods improve the representation of smaller, higher-frequency noise components.

At 61° – Fig. 4.9 (n) – intermediate angle (sensitive direction) angle remains the most challenging noise prediction PSD. The simulations display a systematic sub-prediction of PSD across a wide frequency band relative to the experimental data, and the discrepancy is slightly apparent for the 4th-order result than for the 2nd-order result. The stronger response of the 4th-order scheme suggests that part of the sub-prediction is not numerical dissipation (which would reduce levels), but rather an over-energetic near-field source in the CFD input used by the FastJetNoise code. Potential causes include the turbulence model ($k - \varepsilon$ RANS treatment producing excessive TKE in the mixing layer), inaccuracies in the inflow/turbulence specification, or limitations of the CAA/acoustic model in filtering fluidynamic properties. Because 61° is known to be sensitive, this deviation points to a modeling issue in the near field rather than a pure discretization artifact.

For a IN sideline location, at 90° – Fig. 4.9 (o) – the numerical predictions align much better with the experimental spectrum: both 2nd- and 4th-order results follow the measured PSD shape and amplitude reasonably closely, with the 4th-order again preserving slightly more high-frequency content, with a better fitting than 2n-order. The good agreement at 90° indicates that the simulation captures the radiated acoustic energy in directions predominantly influenced by small structures and less contaminated by fluidynamic contamination or near-field modeling errors. The better match here supports the conclusion that, for lateral observers, the present CFD joined with CAA approach is reliable once a sufficiently accurate results of the flow field are supplied.

Although the use of higher-order numerical schemes, such as the fourth-order finite-difference discretization, yields improved spectral resolution and a more slight accurate predictions of the far-field pressure spectra, these benefits come at a considerable computational expense. The principal drawback of employing fourth-order formulations lies in the substantial increase in memory (RAM) requirements during the solution of the linearized acoustic propagation equations.

This high memory demand is mainly due to the LAPACK library used for solving the eigenvalue problems associated with wave propagation. LAPACK stores each complex variable as a 16-byte number (8 bytes for the real part and 8 bytes for the imaginary part). Consequently, the total memory requirement for the simulation grows proportionally with the total number of grid points in the CAA domain.

For instance, considering a representative simulation with a mesh resolution of $N_\phi = 200$ azimuthal points, the required RAM for a single case already reaches approximately $23\,GB$. When a finer mesh is used – such as $N_\phi = 300$, with the same number of radial and axial points $(N_\phi = N_r)$ -— the estimated RAM usage rises dramatically. The total required memory can be estimated by the following expression:

$$RAM = N_\phi \times N_r \times N_{plans} \times 16 \approx 50.8 \quad [Gb] \tag{4.2}$$

where, $N_\phi = N_r = 300$, $N_{plans} = 37$ from the extraction planes.

This limitation of the LAPAC does not allies with the objectives of this work. On the other hand, with a considerable memory availability, the 4th-order cases can be easily performed in a appropriate workstation.

4.3 Chapter Conclusions

In summary to the chapter conclusions, the association of CFD and CAA simulations for JMN scenarios is generally a feasible tool for noise prediction. As seen, the use of total axisymmetric geometries, for instance R40 nozzle, produces a reliable batch of results. This approach can be used as an industrial tool or even in an academic purpose.

With a critical overview around the CFD responses and methodology, their results can be fed into CAA codes based in the presented GAA, for instance the FastJetNoise. As observed, a well-resolved flow field is more important than the acoustical mesh discretization for 2n-order schemes, and for the considered Strouhal range, the CAA mesh with $N_r = N_\phi \approx 250$ produces reliable results. Other GAA-based solvers, as seen in Leib (2020), depicts some recommendation in CAA mesh discretization, being $N_\phi = 360$ and $N_r = 300$.

The deviations observed at 61° observer angle reinforce the importance of accurate turbulence modeling in the intermediate acoustic field, where both fluidynamic and acoustic components interact strongly. Despite these localized differences, the model reproduces the experimental trends with satisfactory precision, validating its applicability for further parametric and predictive studies.

Overall, the results demonstrate that the current CAA framework is capable of capturing the main acoustic characteristics in cases that involve $0.7 \leq M_a \leq 0.8$ for single stream, isolated, cold jets, both in directivity and spectral distribution. However to deal with JMN problems using the methodology presented here, is recommended pay attention in the following points:

- **Discretization effect**: The 4th-order method consistently preserves more high-frequency energy (less numerical dissipation) and therefore tends to produce spectra that are closer to experiment at high frequencies, especially for downstream (43°) and sideline (90°) observers;
- **Modeling vs numerical results**: The persistent sub-prediction at $\theta = 61^\circ$ indicates a physical/modeling issue in the near-field source (turbulence intensity, shear-layer development, or a residual hydrodynamic component being projected into the acoustic field), rather than a simple lack of numerical accuracy. This must be regarded for studies of other geometries.

5 Thesis Conclusions

As mentioned it the Section 1, the main objectives proposed for this work were achieved and documented. This thesis investigated the feasibility of using a combined CFD and CAA approach to predict jet noise under static conditions. The study evaluated several nozzle geometries and confirmed that this methodology is a robust and reliable way to estimate the Power Spectral Density (PSD) of jet noise.

Although Reynolds-Averaged Navier-Stokes (RANS) models with second-order precision schemes are common in engineering, they are not suitable for characterizing aeroacoustics, particularly in the far-field. The complex physics of sound propagation in transonic flows requires high-order methods to achieve accurate PSD results. Despite the high computational demand of these methods, this work successfully developed a solid methodology for preliminary Passive Noise Reduction Device (PNRD) investigations, even when using low-cost, reduced-order methods with limited CPU availability.

The use of a generalized acoustic analogy (GAA), as implemented in the FastJetNoise code, provided a computationally efficient solution. For example, simulations performed on a common workstation (with an Intel™i7 processor) produced reliable PSD results in just a few hours.

However, to ensure the accuracy of these results, specific precautions must be taken during mesh construction. These include using symmetry, correctly defining boundary conditions, and ensuring the proper y^+ value and boundary layer definition. These parameters are crucial, once they directly affect the CFD solution, which is responsible for the flow field calculation and, consequently, the accurate prediction of the noise signature in the far-field.

6 Future Research

The present study has contributed to the understanding of jet flow and noise generation mechanisms through numerical and experimental comparisons. However, several aspects remain open for further investigation. Future research should focus on improving numerical efficiency, refining modeling accuracy, and exploring alternative computational approaches. The following recommendations outline potential directions that could enhance the predictive capability, computational performance, and physical fidelity of future simulations.

The use of automatic meshing tools represents an important step toward more efficient and reliable CFD workflows. Automated grid generation minimizes manual intervention, reduces user bias, and ensures greater consistency across different geometries. This approach is particularly beneficial when conducting parametric or optimization studies, where multiple configurations must be analyzed under similar numerical conditions.

The use of CFD solvers with Adaptive Mesh Refinement (AMR), as demonstrated by Lima et al. (2020), could further optimize the computational process. AMR dynamically adjusts the grid resolution based on local flow gradients, refining regions with high turbulence intensity other flow properties while keeping coarser grids elsewhere. This method enables accurate resolution of critical flow structures without excessively increasing computational costs.

Another promising direction involves reducing the simulation domain and extending the acoustic collection region downstream beyond $x/D_j > 20$. Expanding this range allows for capturing the complete jet development and radiated noise field, leading to improved far-field predictions. Additionally, optimizing the computational domain can help mitigate boundary effects and reduce artificial diffusion that may distort acoustic results.

Further studies should test other PNRD geometries to verify the robustness of the present methodology. Several geometries and their variations are constantly tested in experimental campaigns, as presented by Bridges and Brown (2004); Brown and Bridges (2006); Câmara et al. (2026); Meyer et al. (2013), among others.

The use of open-source CFD solvers presents another valuable avenue for future research. Tools such as OpenFOAM enable customized model development, greater flexibility in numerical schemes, and full transparency of solver configurations, as performed by Dutra da Silva et al. (2022). Open-source frameworks also promote collaboration, reproducibility, and broader accessibility within the research community.

Finally, future studies should evaluate the balance between performance degradation and noise reduction. Understanding this trade-off is fundamental for practical nozzle design, where aerodynamic efficiency often conflicts with acoustic mitigation goals. Establishing this balance can guide the development of optimized nozzles that maintain acceptable performance while achieving significant noise suppression.

Bibliography and References

Airbus (2007). Aircraft noise - technologies and operations. Available online at `https://www.aerosociety.com/media/4659/2-design-to-lower-noise.pdf` (accessed: 01.09.2024).

Airbus (2019). Aircraft noise - technologies and operations. Available online at `https://www.airbus.com/sites/g/files/jlcbta136/files/2021-09/GMF-2019-2038-Airbus-Commercial-Aircraft-book.pdf` (accessed: 01.09.2024).

Allen, R., Mendonca, F., and Kirkham, D. (2005). Rans and des turbulence model predictions of noise on the m219 cavity at m=0.85. *International Journal of Aeroacoustics*, 4:135–151. `https://doi.org/10.1260/1475472053730039`.

Almeida, O. d. (2009). Aeroacoustics of dual-stream jets with application to turbofan engines.

Almeida, O. d., Barbosa, J. R., Moro, J. B., and Self, R. H. (2014). Noise source distribution of coaxial subsonic jet-short-cowl nozzle. *Journal of Aerospace Technology and Management*, 6:43–52 `https://doi.org/10.5028/jatm.v6i1.258`.

ANSYS (2021a). Ansys fluent theory guide. *Ansys Inc., USA*, 15317:1069.

ANSYS (2021b). Ansys fluent workbench tutorial guide. *Ansys Inc., USA*, 15317:78.

Berg, R. E. (2025). Acoustics. Available online at `https://www.britannica.com/science/acoustics/Measuring-the-speed-of-sound` (accessed: 2025-09-02).

Bodony, D. J. and Lele, S. K. (2008). Current status of jet noise predictions using large-eddy simulation. *AIAA journal*, 46(2):364–380 `https://doi.org/10.2514/1.24475`.

Boussinesq, J. (1877). *Essai sur la théorie des eaux courantes*. Impr. nationale.

Bridges, J. and Brown, C. (2004). Parametric testing of chevrons on single flow hot jets. In *10th AIAA/CEAS aeroacoustics conference*, pages 2824 `https://doi.org/10.2514/6.2004--2824`.

Brown, C. and Bridges, J. (2006). Small hot jet acoustic rig validation. Technical report.

Câmara, F. A., Rosa, V. H., Deschamps, C. J., and da Silva, F. D. (2026). Experimental analysis of jet noise and thrust in nozzles with zigzag-shaped vortex generators. *Applied Acoustics*, 241:111036 `https://doi.org/10.1016/j.apacoust.2025.111036`.

Cambonie, T., Mbailassem, F., and Gourdon, E. (2018). Bending a quarter wavelength resonator: Curvature effects on sound absorption properties. *Applied Acoustics*, 131:87–102 `https://doi.org/10.1016/j.apacoust.2017.10.004`.

Cengel, Y. and Cimbala, J. (2013). *Ebook: Fluid mechanics fundamentals and applications (si units)*. McGraw Hill.

da Vinci, L. (XVI). Studies of water passing obstacles - by Leonardo da Vinci.

Dean, P. D. (1974). An in situ method of wall acoustic impedance measurement in flow ducts. *Journal of Sound and Vibration*, 34(1):97–IN6 `https://doi.org/10.1016/S0022--460X(74)80357--3`.

Duarte, M. A. V. (1985). *Redução de ruídos em motores elétricos*. Florianópolis, SC.

Dutra da Silva, F., Pereira, V., and Cardoso, W. (2022). Prediction of axisymmetric turbulent jet flows using openfoam. pages `https://doi.org/10.26678/ABCM.EPTT2022.EPT22--0010`.

European Civil Aviation Conference (2005a). Report on standard method of computing noise contours around civil airports. Technical guide, European Civil Aviation Conference.

European Civil Aviation Conference (2005b). Report on standard method of computing noise contours around civil airports. Technical guide, European Civil Aviation Conference.

Ferziger, J. H. and Peric, M. (2012). *Computational Methods for Fluid Dynamics*. Springer Berlin Heidelberg. `https://doi.org/10.1007/978-3-319-99693-6`.

Ffowcs Williams, J. E. and Hawkings, D. L. (1969). Sound generation by turbulence and surfaces in arbitrary motion. *Philosophical Transactions of the Royal Society of London. Series A, Mathematical and Physical Sciences*, 264:321–342. `https://doi.org/10.1098/rsta.1969.0031`.

Field, C. and Fricke, F. (1998). Theory and applications of quarter-wave resonators: A prelude to their use for attenuating noise entering buildings through ventilation openings. *Applied Acoustics*, 53(1):117–132. `https://doi.org/10.1016/S0003-682X(97)00035-2`.

Flabes Neto, P. B. (2018). *Investigação matemática e numérica dos mecanismos de geração de ruído em escoamentos cisalhantes livres*. PhD thesis, Universidade Federal de Uberlândia, Uberlândia, Brasil. `http://dx.doi.org/10.14393/ufu.te.2019.314`.

Fontes, D. H., Vilela, V., Meira, L. d. S., and Souza, F. J. d. (2019). Improved hybrid model applied to liquid jet in crossflow. *International Journal of Multiphase Flow*, 114:98–114. `https://doi.org/10.1016/j.ijmultiphaseflow.2019.02.009`.

Gerges, S. N. Y. (2000). *Ruído: Fundamentos e Controle*. S. N. Y. Gerges, Florianópolis, Brasil, 2nd edition edition.

Giraldo, D. A. (2019). *Experimental aeroacoustic and aerodynamic analysis of a large-scale flap side-edge model*. PhD thesis, Universidade de São Paulo. `https://doi.org/10.11606/D.18.2019.tde-09092019-183442`.

Goldstein, M. and Leib, S. (2008). The aeroacoustics of slowly diverging supersonic jets. *Journal of Fluid Mechanics*, 600:291–337 `https://doi.org/10.1017/S0022112008000311`.

Goldstein, M. E. (1976). *Aeroacoustics*. McGraw-Hill International Book Co.

Goldstein, M. E. (2003). A generalized acoustic analogy. *Journal of Fluid Mechanics*, 488:315–333 `https://doi.org/10.1017/S0022112003004890`.

Hansell, A. L., Blangiardo, M., Fortunato, L., Floud, S., De Hoogh, K., Fecht, D., Ghosh, R. E., Laszlo, H. E., Pearson, C., Beale, L., et al. (2013). Aircraft noise and cardiovascular disease near heathrow airport in london: small area study. *BMJ*, 347 `https://doi.org/10.1136/bmj.f5432`.

Hardin, J. C. and Hussaini, M. Y. (2012). *Computational aeroacoustics*. Springer Science & Business Media.

Helmholtz, H. v. (1877). *Die Lehre von den Tonempfindungen als physiologische Grundlage für die Theorie der Musik*. F. Vieweg & Sohn. `https://doi.org/10.1007/978-3-663-18653-3`.

Henshaw, M. J. d. C. (2000). M219 cavity case in verification and validation data for computational unsteady aerodynamics. *RTO-TR-26, AC/323(AVT)TP/19*, pages 473–480.

Heywood, J. (2018). Internal combustion engine fundamentals. `https://doi.org/10.1016/S1350-4789(18)30331-3`.

Howe, M. S. (1998). *Acoustics on Fluid-Structure Interactions.* Cambridge University Press, Cambridge, United Kingdom, 1st edition edition. `https://doi.org/10.1017/CBO9780511662898`.

Howe, M. S. (2003). *Theory of Vortex Sound.* Cambridge University Press, Cambridge, United Kingdom, 1st edition edition.

Hubbard, H. H. (1991). *Aeroacoustics of flight vehicles: theory and practice*, volume 1. National Aeronautics and Space Administration, Office of Management ....

Incropera, F. P., Dewitt, D. P., and Lavine, T. L. B. A. S. (2008). *Fundamentos de Transferência de Calor e Massa.* LTR - Livros Técnicos e Científicos Editora S.A., Rio de Janeiro - RJ, 6ª edição edition.

International Civil Aviation Organization (ICAO) (2016). *ICAO Environmental Report - On Board a Sustainable Future.* International Civil Aviation Organization, Montreal, Canada. Available online at `https://www.icao.int/environmental-protection/Pages/EnvReport.aspx`.

International Civil Aviation Organization (ICAO) (2022). *ICAO Environmental Report - Innovation For a Green Transition.* International Civil Aviation Organization, Montreal, Canada. Available online at `https://www.icao.int/environmental-protection/Pages/EnvReport.aspx`.

International Commission for Acoustics (ICA) (2021). International Year of Sound 2020-2021. Available online at `https://www.sound2020.org/` (accessed: 2025-09-02).

Ishii, T., Nagai, K., Oinuma, H., Oishi, T., and Ishii, Y. (2019). Jet noise reduction of turbofan engine by notched nozzle. In *INTER-NOISE and NOISE-CON Congress and Conference Proceedings*, volume 259, pages 5838–5847. Institute of Noise Control Engineering.

Islam, M., Decker, F., Hartmann, M., Jäger, A., Lemke, T., Ocker, J., Schwarz, V., Ullrich, F., Shröder, A., and Heider, A. (2008). Investigations of sunroof buffeting in an idealised generic vehicle model - part i: Experimental results. *AIAA/CEAS Aeroacoustics Conference (29th AIAA*

Aeroacoustics Conference), 14. P: 1–21. `https://doi.org/10.2514/6.2008-2900`.

Jordan, P. and Colonius, T. (2013). Wave packets and turbulent jet noise. *Annual review of fluid mechanics*, 45(1):173–195. `https://doi.org/10.1146/annurev-fluid-011212-140756`.

Jordan, P., Gervais, Y., Valiere, J., and Foulon, H. (2002). Final results from single point measurements. project deliverable d3. 4, jean—eu 5th framework programme. Technical report, G4RD-CT2000-00313. `https://doi.org/10.1260/147547208784079917`.

Katopodes, N. D. (2019). Chapter 5 - viscous fluid flow. In Katopodes, N. D., editor, *Free-Surface Flow*, pages 324–426. Butterworth-Heinemann. `https://doi.org/10.1016/B978-0-12-815489-2.00005-8`.

Launder, B. E. and Spalding, D. B. (1972). Lectures in mathematical models of turbulence.

Laurendeau, E., Bonnet, J.-P., Jordan, P., and Delville, J. (2006). Impact of fluidic chevrons on the turbulence structure of a subsonic jet. In *3rd AIAA Flow Control Conference*, page 3510. `https://doi.org/10.2514/6.2006-3510`.

Lawrence, J. (2014). *Aeroacoustic interactions of installed subsonic round jets*. PhD thesis, University of Southampton.

Leib, S. and Goldstein, M. (2011). Hybrid source model for predicting high-speed jet noise. *AIAA journal*, 49(7):1324–1335. `https://doi.org/10.2514/1.J050707`.

Leib, S. J. (2020). User's guide for gaa_jet_fv (v1): A jet noise prediction code based on the generalized acoustic analogy. Technical report, NASA/CR-20205003972.

Leib, S. J. and Bridges, J. E. (2022). Predictions of the azimuthal variation of the noise from chevron jets using an acoustic analogy. `https://doi.org/10.2514/6.2022-2912`.

Leib, S. J. and Bridges, J. E. (2023). Effect of flight on the noise from turbulent jets in the generalized acoustic analogy. In *AIAA SCITECH 2023 Forum*, page 0616. `https://doi.org/10.2514/6.2023-0616`.

Lesieur, M. (2008). *Turbulence in Fluids*. Fluid Mechanics and Its Applications. Springer Netherlands. `https://doi.org/10.1007/978-1-4020-6435-7`.

Lighthill, M. J. (1952). On sound generated aerodynamically i. general theory. *Proceedings of the Royal Society of London. Series A. Mathematical and Physical Sciences*, 211(1107):564–587. `https://doi.org/10.1098/rspa.1952.0060`.

Lighthill, M. J. (1954). On sound generated aerodynamically ii. turbulence as a source of sound. *Proceedings of the Royal Society of London. Series A. Mathematical and Physical Sciences*, 222(1148):1–32. `https://doi.org/10.1098/rspa.1954.0049`.

Lighthill, M. J. (1956). *Viscosity effects in sound waves of finite amplitude*. In Surveys in Mechanics (G. K. Batchelor R. M. Davies, eds.), Cambridge University Press.

Lilley, G. M. (1974). On the noise from jets. *AGARD CP-131 - Advisory Group for Aerospace Research and Development, Conference Proceedings*, pages 131–132.

Lima, B. S. d., de Souza Meira, L., and de Souza, F. J. (2020). Numerical simulation of a water droplet splash: Comparison between plic and hric schemes for the vof transport equation. *European Journal of Mechanics-B/Fluids*, 84:63–70 `https://doi.org/10.1016/j.euromechflu.2020.05.016`.

Lyu, B. and Dowling, A. P. (2019). An experimental study of the effects of lobed nozzles on installed jet noise. *Experiments in Fluids*, 60:1–12. `https://doi.org/10.1007/s00348-019-2819-x`.

Maliska, C. R. (2010). *Transferência de Calor e Mecânica dos Fluidos Computacional*. LTC Editora, Rio de Janeiro, 2 edition.

Marangon, C. (2020). Acústica. `http://www.areaseg.com/acustica/`.

McGuirk, J. and Feng, T. (2021). The near-field aerodynamic characteristics of hot high-speed jets. *Journal of Fluid Mechanics*, 915:A120. `https://doi.org/10.1017/jfm.2021.162`.

Meier, H. F., de Oliveira Junior, A. A. M., and Utzig, J. (2023). *Advances in Turbulence*. Springer. `https://doi.org/10.1007/978-3-031-25990-6`.

Meira, L. d. S. (2018). Análise da formação de aerossóis de jato líquido em escoamento cruzado.

Meira, L. d. S. and Souza, F. J. d. (2020). Numerical investigation of the flow-induced noise in a turbulent flow inside an hvac duct. In *Spring School of Transition and Turbulence*, pages 57–69. Springer. `https://doi.org/10.26678/ABCM.EPTT2020.EPT20-0063`.

Meira, L. d. S. and Souza, F. J. d. (2024). *FastJetNoise: Memorial do Software*. Laboratório de Mecânica de Fluidos.

Menter, F. R. (1994). Two-equation eddy-viscosity turbulence models for engineering applications. *AIAA Journal*, 32:1598–1605. `https://doi.org/10.2514/3.12149`.

Meyer, R., Kuo, C.-W., and McLaughlin, D. K. (2013). Reduction of subsonic jet noise by passive flow control devices. In *19th AIAA/CEAS Aeroacoustics Conference*, page 2147. `https://doi.org/10.2514/6.2013-2147`.

Min, K. B. and Min, J. W. (2017). Exposure to environmental noise and risk for male infertility: A 2 population-based cohort study*. *Environmental Pollution*, 226:118–124. `https://doi.org/10.1016/j.envpol.2017.03.069`.

Morris, P. J. and Zaman, K. B. (2010). Velocity measurements in jets with application to noise source modeling. *Journal of sound and vibration*, 329(4):394–414. `https://doi.org/10.1016/j.jsv.2009.09.024`.

Nallasamy, N. (1999). Survey of turbulence models for the computation of turbulent jet flow and noise. Technical report, NASA/CR-1999-206592.

Oishi, T. (2010). Jet noise reduction by notched nozzle on japanese eco engine project. In *16th AIAA/CEAS Aeroacoustics Conference*, page 4026. `https://doi.org/10.2514/6.2010-4026`.

Pletcher, R., Tannehill, J., and Anderson, D. (2012). *Computational Fluid Mechanics and Heat Transfer, Third Edition*. Series in Computational and Physical Processes in Mechanics and Thermal Sciences. Taylor & Francis.

Pope, S. (1978). An explanation of the turbulent round-jet/plane-jet anomaly. *AIAA journal*, 16(3):279–281. `https://doi.org/10.2514/3.7521`.

Pope, S. B. (2000). *Turbulent Flows*. Cambridge University Press. `https://doi.org/10.1017/CBO9780511840531`.

Proença, A. (2013). *Experimental characterization of velocity and acoustic fields of single-stream subsonic jet*. PhD thesis, MSc dissertation, Federal University of Uberlândia, Uberlândia, Brazil.

Proença, A. (2018). *Aeroacoustics of isolated and installed jets under static and in-flight conditions*. PhD thesis, University of Southampton.

Proenca, A. and Lawrence, J. (2022). Installed jet noise reduction using a zigzag vortex generator. In *28th AIAA/CEAS Aeroacoustics 2022 Conference*, page 2873. `https://doi.org/10.2514/6.2022-2873`.

Randall, D. A. (2003). Reynolds averaging. *Selected notes, Department of Atmospheric Science, Colorado State University*.

Rayleigh, J. W. S. B. (1894). *The theory of sound*, volume 2. Macmillan and Co.

Reynolds, O. (1883). Xxix. an experimental investigation of the circumstances which determine whether the motion of water shall be direct or sinuous, and of the law of resistance in parallel channels. *Philosophical Transactions of the Royal society of London*, (174):935–982. `https://doi.org/10.1098/rstl.1883.0029`.

Reynolds, O. (1895). Iv. on the dynamical theory of incompressible viscous fluids and the determination of the criterion. *Philosophical Transactions of the Royal society of London*, (186):123–164. `https://doi.org/10.1098/rsta.1895.0004`.

Ricciardi, T. R., Arias-Ramirez, W., and Wolf, W. R. (2020). On secondary tones arising in trailing-edge noise at moderate reynolds numbers. *European Journal of Mechanics-B/Fluids*, 79:54–66. `https://doi.org/10.1016/j.euromechflu.2019.08.015`.

Ricciardi, T. R., Wolf, W., Speth, R. L., and Bent, P. (2019). Analysis of noise sources in realistic landing gear configurations through high fidelity simulations. In *AIAA Scitech 2019 Forum*, volume 1. `https://doi.org/10.2514/6.2019-0003`.

Rienstra, S. W. and Hirschberg, A. (2006). *An Introduction to Acoustics*. Eindhoven University of Technology, Eindhoven, Netherlands, 2st edition edition.

Rosa, V. H., Self, R., Ilário, C., Naqavi, I., and Tucker, P. (2016). Modelling velocity correlations with les and rans for prediction of noise from isothermal or hot jets. In *22nd AIAA/CEAS Aeroacoustics Conference*, page 2810. `https://doi.org/10.2514/6.2016-2810`.

Saiyed, N., Bridges, J., and Mikkelsen, K. (2000). Acoustics and thrust of separate-flow exhaust nozzles with mixing devices for high-bypass-ratio engines. In *6th Aeroacoustics Conference and Exhibit*, page 1961. `https://doi.org/10.2514/6.2000-1961`.

Silva, C. R. I. d. (2011). *Development of a novel RANS-based method for the computational aeroacoustics of high speed jets*. PhD thesis, PhD Thesis. University of São Paulo. Brazil.

Silveira Neto, A. (2020). *Escoamentos Turbulentos: Análise Física e Modelagem Teórica*. Universidade Federal de Uberlândia, 1ª edição edition.

Smagorinsky, J. (1963). General circulation experiments with the primitive equations. `https://doi.org/10.1175/1520-0493(1963)091<0099:GCEWTP>2.3.CO;2`.

Smith, M. J. T. (1989). *Aircraft Noise*. Cambridge University Press, Cambridge, United Kingdom, 1st edition edition. `https://doi.org/10.1017/CBO9780511584527`.

Souza, F. J. (2012). *UNSCYFL3D Versão 2.0 - Manual Teórico*. Federal University of Uberlândia, MFLab - Fluid Mechanics Laboratory.

T Munzel, T Gori, W. B. and Basner, M. (2014). Cardiovascular effects of environmental noise exposure. *European Heart Journal*, 35:829–836. `https://doi.org/10.1093/eurheartj/ehu030`.

Tam, C. K. (1995). Supersonic jet noise. *Annual review of fluid mechanics*, 27(1):17–43. `https://doi.org/10.1146/annurev.fluid.27.1.17`.

Tam, C. K. (1998). Jet noise: since 1952. *Theoretical and computational fluid dynamics*, 10(1):393–405. `https://doi.org/10.1007/s001620050072`.

Tanna, H. (1977). An experimental study of jet noise part i: Turbulent mixing noise. *Journal of sound and Vibration*, 50(3):405–428. `https://doi.org/10.1016/0022-460X(77)90493-X`.

Teodoro, E. B. (1985). *Redução de ruído em condicionadores de ar*. Florianópolis, SC.

Van Dyke, M. (1982). *An album of fluid motion*. Parabolic Press Stanford, California. `https://doi.org/10.1115/1.3241909`.

Versteeg, H. and Malalasekera, W. (2007). *An Introduction to Computational Fluid Dynamics: The Finite Volume Method*. Pearson Education Limited.

Viswanathan, K. (2009). Mechanisms of jet noise generation: classical theories and recent developments. *International journal of aeroacoustics*, 8(4):355–407. `https://doi.org/10.1260/147547209787548949`.

White, F. M. (2011). *Mecânica dos Fluidos*. AMGH Editora Ltda, Porto Alegre - RS, 6ª edição edition.

White, F. M. and Corfield, I. (2006). *Viscous fluid flow*, volume 3. McGraw-Hill New York.

Wilcox, D. C. (1993). *Turbulence modelling for CFD*. DCW Industries, La Canada.

Witze, P. O. (1974). Centerline velocity decay of compressible free jets. *AIAA journal*, 12(4):417–418. `https://doi.org/10.2514/3.49262`.

Zhang, X. (2010). Airframe noise–high lift device noise. *Encyclopedia of Aerospace Engineering*, page `https://doi.org/10.1002/9780470686652.eae338`.

Apêndice A – Survey About PNRDs and Trends

A.1 Table of Patents of PNRDs for Aircraft and Discharge Nozzles

Table A.1: List of patents

Index	Year	Code	Assignee	Type	Principle and Characteristics
1	1953	US2650752A	RTX Corp.	PNRD	Vortex generators are disposed in regions of BL detachment to improve aerodynamics in rotors, spinners and confining surfaces (diffuser and nozzles).
2	1955	US2944623A	Individual (Bodine Jr, A. G.)	ANRD	A circular set of vanes creates a swirling flow to promote mixture in convergent nozzles.
3	1958	US2990905A	Individual (Lilley, G. M.)	ANRD	A system of high pressure micro-jets disposed circularly on the nozzle leading edge to promote mixture.
4	1960	US3161257A	Individual (Young, A. D.)	PNRD and ANRD	Vanes disposed inside and ouside of the nozzle with capacity of angle adjustment.
5	1964	US3153319A	Individual (Young, A. D.; Lane, W.; Lilley, G. M.; End, W.; Westley, R.)	PNRD	Squared corrugated nozzles.
6	1969	US3612209A	General Electric Co.	ANRD	Thrust reverser and sound suppressor. Based on internal pivoted flaps at the engine fairing.

Continued on next page

Table A.1 – continued from previous page

Index	Year	Code	Assignee	Type	Principle and Characteristics
7	1969	US3587973A	General Electric Co.	ANRD	An active system of flaps mounted internally in the engine cowl. The flaps consist in perforated plates and tubes for noise suppression.
8	1973	US3830431A	NASA	ANRD	A rotary component in the exhaust portion of the engine which swirls the axial jet.
9	1973	US3893640A	General Electric Co.	PNRD	A sound suppressing nacelle arrangement. It is disposed at the outer engine fairing.
10	1974	US3889882A	General Electric Co.	ANRD	A retractable sound suppressor composed by a plurality of variable nozzle flaps.
11	1974	US3934675A	Lear Avia Corp.	PNRD	Metal sheets in radial lobe disposition in nozzle for business jets (Learjet versions).
12	1975	US3982696A	Grumman American Aviation Corp	PNRD	A plurality of chute flow dividers through which air passes to mix with the jet gases at downstream end of the engine. The Coanda effect enhance the mixture.
13	1975	US3987621A	RTX Corp	PNRD	Device for mixing bypass jetstream and atmospheric air.
14	1979	US4280587	Boeing Co.	PNRD and ANRD	Series of devices and approaches for non-coaxial turbofan engines. Some of them uses the nozzle geometry or eccentricity of core and bypass flow.

Continued on next page

Table A.1 – continued from previous page

Index	Year	Code	Assignee	Type	Principle and Characteristics
15	1979	US4291782A	Boeing Co.	ANRD	A portion of the jet engine exhaust flow is selectively directed to a nozzle which at least partially surrounds the circumference of the jet engine exhaust.
16	1980	US4335801A	Boeing Co.	PNRD	Wall deflections of a multi-lobe type noise suppressing nozzle are minimized without the use of external struts and by the use of only a single internal strut per lobe.
17	1987	US4934481A	Individual (Thomas E. Friedrich)	ANRD	A plurality of vanes that extend substantially around the engine cowl in the end of the nozzle. These vanes promote mixture between hot and surrounding cold air.
18	1987	US4958700A	Rheinhold and Mahla GmbH. & Cantrell Machine Co. Inc.	Test facility	A protective facility for suppressing jet aircraft noise which has a primarily horseshoe shape for surrounding a jet aircraft. The exhaust gases are deflected upward during ground tests.
19	1990	EP0405796A1	Nordam Group LLC	ANRD	A series of doors and scoops opens around the engine cowl and a plug coated with absorbers slides in the turbine axis to reduce noise.
20	1997	US5947412A	Engility LLC	ANRD	Conduit assemblies proximate the trailing edges of the internal walls capture a portion of external flow to mixture with the hot core gaseous.

Continued on next page

Table A.1 – continued from previous page

Index	Year	Code	Assignee	Type	Principle and Characteristics
21	1998	US6487848B2	RTX Corp	PNRD	An arrangement of tabs disposed circularly on the end of the nozzle. The tapered tabs have a specific entrance angle and spacing.
22	2000	US6233920B1	Stage III Technologies, L.C.	PNRD and ANRD	A contoured thrust reverser and multi-lobe nozzle that reduce engine noise.
23	2000	US6318070B1	United Technologies Corp.	ANRD	The flaps are actuated by a plurality of actuating mechanisms driven by shape memory alloy (SMA) actuators to vary fan exist nozzle area.
24	2001	US6314721B1	United Technologies Corp.	PNRD	The nozzle has an arrangement of triangular tabs in alternate entrance angles, acting as vortex generators.
25	2001	US6532729B2	General Electric Co.	PNRD	Circumferential adjoining chevrons extend from the duct aft end around only an arcuate portion thereof leaving a plain arcuate shelf between terminal ones of the chevrons.
26	2001	US20020189896A1	Pratt and Whitney Canada Corp	PNRD	An exhaust flow guide attached to the engine exhaust end, wich diverges the flow and reflets part of the noise upwards.
27	2002	US20030231777A1	Boeing Co.	ANRD	A set of piezoelectric tabs disposed circumferential at the engine exhaust that alters its shape by an AC signal.

Continued on next page

Table A.1 – continued from previous page

Index	**Year**	**Code**	**Assignee**	**Type**	**Principle and Characteristics**
28	2003	US20040031258A1	University of California	ANRD	An internal deflector moved by an actuator disturbs the flow symmetry to enhance mixture.
29	2004	EP1493912A1	General Electric Co.	ANRD	Fluidic chevrons and configurable thermal shield for jet noise reduction.
30	2004	US20050115245A1	Safran Aircraft Engines SAS	PNRD	Notches are asymmetrical relative to the vertical axis aiming to produce counter-rotating effect between the gas flows.
31	2004	US20050166575A1	Rolls Royce PLC	ANRD	A plurality of tabs likewise chevrons with tapered shape and controlled.
32	2004	US20050193716A1	RTX Corp	PNRD	A plurality of mixer lobes and a common flow nozzle having an equal number of tabs located along a circumferential edge of an aft end of the nozzle.
33	2004	WO2005068796A1	Poly Systems Pty Limited	PNRD	Exhausting pipe for internal combustion engines and gas turbines (turboprops).
34	2005	EP1561939A2	General Electric Co.	ANRD	Sinuous chevron exhaust nozzles.
35	2005	EP1731747A1	United Technologies Corp.	PNRD	A system for reducing jet noise emission of mixer lobes and twisted metal sheets.
36	2005	GB2431720A	Rolls Royce PLC	ANRD	A series of vortex generators based on shape memory properties.

Continued on next page

Table A.1 – continued from previous page

Index	Year	Code	Assignee	Type	Principle and Characteristics
37	2006	RU2313680C2	Federal State Unitary Enterprise & Central Aerohydrodynamic Institute	PNRD and ANRD	A series of devices that promote mixture in square nozzles and circular nozzles.
38	2006	US20080202847A1	Airbus Operations SAS	ANRD	An arrangement of hollow notches that blows high pressure air.
39	2007	US7966826B2	Boeing Co.	ANRD	A series of chevrons with auxiliary micro-jets driven by a pressurized gas source based on engine parameters and flight conditions.
40	2007	US20080264718A1	Boeing Co.	PNRD	Semi-circumferential shield in the shape of a visor that is adapted to be secured to an external surface of a nozzle housing of a jet nozzle to attenuate jet noise generated by the jet nozzle.
41	2010	DE102010025014A1	EADS Deutschland GmbH	ANRD	A device which includes oscillatable ring segments arranged on the inner wall (14) of the nozzle and distributed around the circumference.
42	2011	CN103133180B	AECC Commercial Aircraft Engine Co. LTD	ANRD	Small coaxial spray jets disposed circumferentially to promote high pressure flows from compressor to promote mixture and reduce noise.

Continued on next page

Table A.1 – continued from previous page

Index	Year	Code	Assignee	Type	Principle and Characteristics
43	2011	US8628040B2	Boeing Co.	Aircraft configuration	An aircraft configuration that may reduce the level of roaring jet exhaust noise, infrared radiation, sonic boom, or combination thereof directed towards the ground from an aircraft in flight.
44	2012	US8959889B2	Boeing Co.	ANRD	A method of varying a fan duct nozzle throat area of a gas turbine engine includes pivoting a fan nozzle outwardly relative to a longitudinal axis of the gas turbine engine.
45	2012	US8967326B2	Parafluidics LLC.	PNRD for discharge	A channel composed by an array of modified torus to reduce noise in high velocity discharges of hot gases. This device must be used in industrial plants or firearms.
46	2012	US9261047B2	Lockheed Martin Corp.	ANRD	A device that weakes Mach cones in a jet exhaust gas streamtube. The Mach cones are weakened by modifying exhaust gas flow in a longitudinal axial core of the exhaust gas streamtube.
47	2013	JP6438025B2	Hexcel Corp.	Coating	A sound wave guide within the acoustic cells of an acoustical coating. The two chambers inside the cell provide an effective increase in resonator length of the cell.

Continued on next page

Table A.1 – continued from previous page

Index	Year	Code	Assignee	Type	Principle and Characteristics
48	2013	US20150048177A1	Japan Aerospace Exploration Agency JAXA	PNRD and ANRD	The noise can be reduced by using a simple and light-weight mechanism without increasing the complexity and size of the structure of the exhaust nozzle, and furthermore, the efficiency during cruising at supersonic speeds can be improved.
49	2016	CN106481455B	General Electric Co.	PNRD	System for suppressing noise within a gas turbine combustor. A cavity is created upstream to the combustor and mimic a Helmholtz resonator.
50	2016	US20180080408A1	Safran Aircraft Engines SAS	ANRD	A device for reducing the jet noise by means of blowing micro-jets circularly distributed in the exhaust nozzle.
51	2019	CN110457804A	Nanjing Tech University	Code	Farfield noise extimation for rocket engines by means the FW-H equation based on acoustic analogy method. The present invention reduces number of grid while guaranteeing computational accuracy, and improves computational efficiency.
52	2019	CN210487225U	Low Speed Aerodynamics Institute of China Aerodynamics Research and Development Center	Test device	Subsonic/transonic jet noise research test device. Anechoic chamber, etc.

Continued on next page

Table A.1 – continued from previous page

Index	**Year**	**Code**	**Assignee**	**Type**	**Principle and Characteristics**
53	2020	WO2021138538A1	University of Kansas	ANRD	A device which induces a rotation of a swirl layer to promote mixing of the high-speed or supersonic jet with surrounding air.
54	2021	CN113435135A	Beijing Institute of Technology BIT	Code	Method for estimating jet flow field and noise of bundled rocket engine.
55	2022	JP2022129373A	Japan Aerospace Exploration Agency (JAXA)	ANRD and Aircraft configuration	Supersonic aircraft and method for reducing sonic boom and jet noise. Elevator acts like a barrier to the noise and an engine with a variable nozzle geometry.
56	2022	US12162618B2	Boom Technology Inc.	PNRD	Dissimilarly shaped aircraft nozzles with tandem mixing devices, and associated systems and methods are disclosed.

Apêndice B – Achievements

B.1 Software Registration – FastJetNoise

REPÚBLICA FEDERATIVA DO BRASIL
MINISTÉRIO DO DESENVOLVIMENTO, INDÚSTRIA, COMÉRCIO E SERVIÇOS
INSTITUTO NACIONAL DA PROPRIEDADE INDUSTRIAL
DIRETORIA DE PATENTES, PROGRAMAS DE COMPUTADOR E TOPOGRAFIAS DE CIRCUITOS

Assinado Digitalmente

Certificado de Registro de Programa de Computador

Processo Nº: **BR512024002425-5**

O Instituto Nacional da Propriedade Industrial expede o presente certificado de registro de programa de computador, válido por 50 anos a partir de 1° de janeiro subsequente à data de 12/07/2024, em conformidade com o §2°, art. 2° da Lei 9.609, de 19 de Fevereiro de 1998.

Título: FastJetNoise

Data de publicação: 12/07/2024

Data de criação: 20/12/2023

Titular(es): UNIVERSIDADE FEDERAL DE UBERLÂNDIA

Autor(es): FRANCISCO JOSÉ DE SOUZA; LUCAS DE SOUZA MEIRA

Linguagem: OUTROS

Campo de aplicação: CO-02; FQ-02; IN-02; IN-03; MA-03

Tipo de programa: SM-01; SM-04

Algoritmo hash: SHA-512

Resumo digital hash:
30b76a5a50375d23714951d69eaa4744a7e20572721b920986295ce330c735518e3e71ebc36f8613136e379318371b14579e3abfd02a9dd94eac7eed233b9a7a

Derivação autorizada: Sim, Na qualidade de titular dos direitos patrimoniais de autor que recaem sobre o Programa de Computador acima citado, em observância á Instrução Normativa n. 47, de 22 de janeiro de 2016, autorizo o INPI a reproduzi-lo para mídia diferenciada da original, mediante cópia digital ou por qualquer outro meio ou suporte que se faça necessário, incluindo a aplicação de métodos de compressão e criptografia, para fins de preservação de seu conteúdo.

Expedido em: 23/07/2024

Aprovado por:
Carlos Alexandre Fernandes Silva

Annex A – CFD Result File

Here, we have an example of the exported variables from the CFD results in the measurement lines (or planes in 3D cases). The 3D cases differ by an extra row for Z coordinate. These data are used as input to cylindrical mesh generator, disposed in A.

Listing A.1: `CFD_result.dat` - Excerpt from the CFD file result with variables of interest.

```
cellnumber,    x-coordinate,    y-coordinate,         density,
    axial-velocity,turb-kinetic-energy,  turb-diss-rate,     sound-speed
        1, 8.249999881E-01, 2.177471179E-04, 1.177513634E+00, 2.426225144E+02,
    3.900452351E-01, 4.213992330E+01, 3.471810319E+02
        2, 8.249999881E-01, 6.532413536E-04, 1.177513635E+00, 2.426224911E+02,
    3.905121099E-01, 4.230984894E+01, 3.471810321E+02
        3, 8.249999881E-01, 1.088735531E-03, 1.177513639E+00, 2.426224648E+02,
    3.901302853E-01, 4.220135014E+01, 3.471810317E+02
        4, 8.249999881E-01, 1.524229767E-03, 1.177513632E+00, 2.426224678E+02,
    3.900006870E-01, 4.218260898E+01, 3.471810336E+02
        5, 8.249999881E-01, 1.959724119E-03, 1.177513642E+00, 2.426224527E+02,
    3.899659566E-01, 4.216654041E+01, 3.471810328E+02
        6, 8.249999881E-01, 2.395218238E-03, 1.177513646E+00, 2.426224651E+02,
    3.901596773E-01, 4.220160073E+01, 3.471810337E+02
        7, 8.249999881E-01, 2.830712590E-03, 1.177513662E+00, 2.426224527E+02,
    3.904178054E-01, 4.223692111E+01, 3.471810323E+02
        8, 8.249999881E-01, 3.266206710E-03, 1.177513673E+00, 2.426224682E+02,
    3.907809718E-01, 4.229313787E+01, 3.471810328E+02
        9, 8.249999881E-01, 3.701701062E-03, 1.177513697E+00, 2.426224537E+02,
    3.911886008E-01, 4.235140113E+01, 3.471810312E+02
       10, 8.249999881E-01, 4.137195647E-03, 1.177513715E+00, 2.426224730E+02,
    3.916724421E-01, 4.242394596E+01, 3.471810315E+02
       11, 8.249999881E-01, 4.572689533E-03, 1.177513752E+00, 2.426224560E+02,
    3.922017758E-01, 4.250081384E+01, 3.471810298E+02
 ...
 ...
 ...
      195, 8.249999881E-01, 2.022799104E-01, 1.166434803E+00, 6.494292891E-01,
    1.640087854E-01, 1.553884835E-01, 3.486079206E+02
      196, 8.249999881E-01, 2.149087340E-01, 1.167331134E+00, 6.107975588E-01,
    1.347285181E-01, 1.115848455E-01, 3.484741599E+02
      197, 8.249999881E-01, 2.283930480E-01, 1.168273703E+00, 5.732949308E-01,
    1.098754600E-01, 7.956564780E-02, 3.483336490E+02
      198, 8.249999881E-01, 2.376779765E-01, 1.169258883E+00, 5.367390487E-01,
    8.882820735E-02, 5.630928709E-02, 3.481869546E+02
```

Annex B – Cylindrical Mesh Generator

Here, we have an example of the cylindrical mesh generator. All variables disposed by the measurement lines (or planes in 3D cases) are revolved in a structured mesh by means `revolve_CFDresult.f90`, whose code is described below.

Listing B.1: `revolve_CFDresult.f90` - Excerpt from the code used to generate the structured mesh in cylindrical coordinates.

```
!  revolve_CFDresult.f90
!
!*********************************************************************************
!
!  PURPOSE: this routine will revolve the CFD input data into several revolution
!          planes based on the CFD results from a circular sector or a 2D axial
!   symmetric geometry
!
!*********************************************************************************
!
    subroutine revolve_CFDresult

    use var

    implicit none
    !
    !
    real*8,allocatable :: rho_aux(:),U_aux(:),tke_aux(:),epsilon_aux(:),sound_speed_aux(:)
    real*8 radius_aux,phi_aux
    !
 !
    !
    open(unit=1,FILE=’CFDresult.dat’)   !  CFD File name (cellnumber,    x-coordinate, y-coordinate,         density,  axial-velocity,turb-kinetic-energy,  turb-diss-rate, sound-speed )
    read(1,*)                              !  the first line
    !
 !
    number_of_cells=number_of_sectors*partial_number_of_cells
    !
    allocate(rho_aux(number_of_cells))
    allocate(U_aux(number_of_cells))
    allocate(tke_aux(number_of_cells))
    allocate(epsilon_aux(number_of_cells))
    allocate(sound_speed_aux(number_of_cells))
    allocate(xc(number_of_cells))
    allocate(yc(number_of_cells))
    allocate(zc(number_of_cells))
    !
    open(2,file=’CFDinput.dat’)
    write(2,*)
    !
    ! create new cells and assign values


    if(three)then
      print *,’3D geometry SELECTED’
```

```
    else
      print *,'2D geometry SELECTED'
    endif
    print *

    !
    do slice=1,number_of_slices
      !
      do i=1,partial_number_of_cells
          if(three)then
            read(1,*)
    dummy,xc(i),yc(i),zc(i),rho_aux(i),U_aux(i),tke_aux(i),epsilon_aux(i),sound_speed_aux(i)
          else
            read(1,*)
    dummy,xc(i),yc(i),rho_aux(i),U_aux(i),tke_aux(i),epsilon_aux(i),sound_speed_aux(i)
            zc(i) = 0.d0
          endif

          radius_aux=dsqrt(yc(i)**2.d0+zc(i)**2.d0)
          phi_original=datan(zc(i)/yc(i))

          do sector=1,number_of_sectors-1
            phi_aux=phi_original+dble(sector)*2.d0*pi/dble(number_of_sectors)
            index=i+sector*partial_number_of_cells

            yc(index)=radius_aux*dcos(phi_aux)
            zc(index)=radius_aux*dsin(phi_aux)
            xc(index)=xc(i)
            rho_aux(index)=rho_aux(i)
            U_aux(index)=U_aux(i)
            tke_aux(index)=tke_aux(i)
            epsilon_aux(index)=epsilon_aux(i)
            sound_speed_aux(index)=sound_speed_aux(i)
          enddo
      enddo
   !
      do i=1,number_of_cells
           write(2,'(g19.10,g19.10,g19.10,g19.10,g19.10,g19.10,g19.10)') &
           yc(i),zc(i),rho_aux(i),U_aux(i),tke_aux(i),epsilon_aux(i),sound_speed_aux(i)
      enddo
    enddo

!
    close(1)
    close(2)
    deallocate(xc)
    deallocate(yc)
    deallocate(zc)
!
!    end program revolve_CFDresult
    return
    end subroutine revolve_CFDresult
```

Annex C – FastJetNoise Setup

Here, we have an example of a setup of FastJetNoise. All variables and inputs disposed here are commented for easy understanding by users in file `setup.dat`, which is described in the following.

Listing C.1: `setup.dat` - Example of setup used for a CAA simulation of SC12 at $Ma = 0.8$ at an observer angle $\phi = 90°$ with 4th order scheme.

```
t 1    3D? interpolation method (2nd order = 0↵ 4th order = 1)
340.0    sound_speed_infinity↵ U_infinity
0.0    U_infinity
1.4    gamma

200    n_radial
200    n_phi
37    number_of_slices

0.04    D_jet
276.12    U_jet
90.0    observer_theta
0.0    observer_phi
1.0    observer_radius
6    max_radius
105    number_of_frequencies

400.0    frequency
400.0    bandwidth

0.5    delta_x
---------------------used in revolve
6232    partial_number_of_cells
16    number_of_sectors
```